

Surface Plasmon Fluorescence Spectroscopy and Surface Plasmon Diffraction in Biomolecular Interaction Studies

Dissertation zur Erlangung des Grades

‘Doktor der Naturwissenschaft’

am Fachbereich Biologie

der Johannes Gutenberg-Universität

in Mainz

vorgelegt von

Fang Yu

aus Zhejiang, V. R. China

Mainz, April, 2004

Dekan: Prof. Dr. H. Paulsen

1. Berichterstatter: Prof. W. Knoll

2. Berichterstatter: Prof. H. Decker

3. Berichterstatter: Prof. J. Markl

Tag der mündlichen Prüfung: 11, Mai 2004

Die vorliegende Arbeit wurde unter Betreuung von Herrn Prof. Dr. W. Knoll im Zeitraum zwischen August 2000 bis Mai 2004 am Max-Planck-Institute für Polymerforschung, Mainz, Deutschland angefertigt.

Contents

1	INTRODUCTION.....	1
1.1	BIOSENSORS IN THE POST-GENOMIC ERA	1
1.2	SURFACE PLASMON BASED (SENSING) TECHNIQUES.....	2
1.3	AIM OF THE STUDY	3
2	THEORY	5
2.1	SURFACE PLASMON OPTICS.....	5
2.1.1	<i>Maxwell equations – a starting point:</i>	5
2.1.2	<i>Wave equations and dispersion relation of surface plasmons:</i>	6
2.1.3	<i>Spatial extensions of SP fields and propagation of SPs</i>	8
2.1.4	<i>Excitation of SPs by light</i>	9
2.1.4.1	Prism coupling	10
2.1.4.2	Grating coupling	13
2.1.5	<i>SPR response to a thin film deposition</i>	14
2.1.6	<i>Field enhancement</i>	15
2.2	SURFACE DIFFRACTION	17
2.2.1	<i>Diffraction from a smooth, sinusoidal surface</i>	17
2.2.2	<i>Fourier diffraction optics</i>	19
2.3	FLUORESCENCE	20
2.3.1	<i>Fluorescence process</i>	20
2.3.2	<i>Fluorescence quenching and self-quenching</i>	21
2.3.3	<i>Fluorescence resonance energy transfer</i>	22
2.3.4	<i>Photobleaching</i>	23
2.3.5	<i>Fluorescence at the metal/dielectric interface</i>	23
2.4	INTERFACIAL BIOMOLECULAR INTERACTION ANALYSIS	25
2.4.1	<i>Interface kinetics based on Langmuir adsorption model</i>	25
2.4.2	<i>Mass-transport controlled kinetics</i>	27
2.4.3	<i>Interaction controlled kinetics</i>	27
2.4.4	<i>Equilibrium analysis</i>	29
2.4.5	<i>Applicability of the kinetic model</i>	29
3	EXPERIMENTAL	31
3.1	INSTRUMENTAL	31
3.2	FLOW CELL AND LIQUID HANDLING	34
3.3	PROTEIN LABELING.....	36
3.4	SURFACE FUNCTIONALIZATION TECHNIQUES.....	38
3.4.1	<i>Self-assembled monolayers</i>	38
3.4.2	<i>Micro-contact printing (μCP)</i>	40
3.4.3	<i>UV-photo-patterning</i>	42
4	SPR/SPFS STUDIES ON PLANAR SURFACES	44
4.1	MOTIVATIONS	44
4.2	MATERIALS	45
4.3	PROTEIN RESISTANCE OF THE SAM SURFACES	46
4.4	SURFACE REGENERATION	48
4.5	MASS-TRANSPORT LIMITED BINDING RATES	50
4.6	AVIDITY INFLUENCE ON THE IGG BINDING KINETICS	51
4.7	SELF-QUENCHING OF CY5 AND AF 647	53
4.8	DETUNING OF FLUORESCENCE	55
4.9	THREE DIMENSIONAL IGG ARRANGEMENT	56
4.10	SPFS DETECTION OF EXTREMELY DILUTED ANTIGEN DENSITIES	59
4.11	A LAYER-BY-LAYER MODEL	61

4.12	AFFINITY DETERMINATION BETWEEN HIL8 AND ITS ANTIBODY FRAGMENTS	63
4.13	CONCLUSION	65
5	SPFS IMMUNOASSAY ON 3D MATRIX	67
5.1	MOTIVATIONS.....	67
5.2	LOD ASSESSMENT OF SPFS.....	69
5.2.1	<i>Materials</i>	69
5.2.2	<i>Use of CM5 chip in the SPFS set-up</i>	70
5.2.3	<i>Calibrate the SPR signal to surface protein concentrations</i>	71
5.2.4	<i>Protein immobilization to a dextran matrix</i>	73
5.2.5	<i>LOD of SPFS</i>	74
5.2.5.1	Baseline deviation	76
5.2.5.2	Dose-response curve.....	76
5.2.5.3	LOD at atto-molar level.....	78
5.2.6	<i>Parallel comparison to Biacore 3000</i>	81
5.2.7	<i>SPFS in other modes</i>	82
5.2.7.1	SPFS+FOS	82
5.2.7.2	SPFM.....	83
5.3	SPFS PSA ASSAY	84
5.3.1	<i>Experimental</i>	85
5.3.2	<i>Affinity determination</i>	86
5.3.3	<i>Sandwich PSA assays</i>	88
5.3.4	<i>Binding in buffer and human plasma</i>	90
5.3.5	<i>Removal of plasma NSB and LOD evaluation</i>	91
5.4	CONCLUSION	92
6	SURFACE PLASMON DIFFRACTION	93
6.1	BACKGROUND	93
6.2	DIFFRACTION ENHANCEMENT BY SURFACE PLASMON FIELDS	95
6.3	THEORETICAL DESCRIPTION.....	97
6.4	ANTIBODY BINDING TO PATTERNED SAM	99
6.4.1	<i>Microscopic characterization on patterned surfaces</i>	99
6.4.2	<i>Antibody monolayer induced light diffraction</i>	100
6.4.3	<i>Quadratic effect of diffraction intensity</i>	101
6.4.4	<i>Estimation of the biotin density</i>	102
6.5	SELF-REFERENCING PROPERTY	104
6.6	PICO-MOLAR SENSITIVITY FOR HCG DETECTION.....	107
6.7	OLIGONUCLEOTIDE HYBRIDIZATION STUDIES	109
6.7.1	<i>Kinetic studies</i>	111
6.7.2	<i>Equilibrium titration</i>	115
6.7.3	<i>Probe density engineering</i>	117
6.8	CONCLUSIONS.....	118
7	SUMMARY.....	120
8	SUPPLEMENT.....	122
8.1	ABBREVIATIONS	122
8.2	LIST OF FIGURES.....	124
8.3	LIST OF TABLES	127
8.4	BIBLIOGRAPHY	128
	ACKNOWLEDGEMENTS.....	137
	CURRICULUM VITAE.....	138

1 Introduction

1.1 Biosensors in the post-genomic era

The biological functions of most macromolecules depend on their ability to interact with other molecules. While in biology labs, haptens, tracers, immunoconjugates and antibodies are routinely characterized to determine their identities and purities, their kinetic and thermodynamic properties are seldomly acquired. In the post-genomic era, one of the greatest challenges facing the chemical biology community is a complete understanding and description of the interaction of the proteome. This information will provide insights into the mechanism of biological processes, and opportunities for controlling these processes by, e.g., interrupting key molecular interactions. Therefore, the interaction parameters are of great importance at all stages of proteomics development. However, laborious endeavor may be demanded for the determination of these parameters if applying conventional techniques. In this context, various biosensors¹ were developed and have been an increasingly impactful technology for biomolecular interaction analysis (BIA). These technologies have greatly simplified the task of BIA with their easy access to high-quality kinetic and thermodynamic data. More exciting progresses are being made to allow large-scale interaction studies² for helping the development of a complete set of proteomic interaction maps in an age where the full genomes have been sequenced!!³

Biosensors are devices that combine the specificity of biological molecules with physical detection strategy, e.g., using electronic or optical systems.⁴ Biosensors use specific bio-recognition elements immobilized on the surface to transduce the biological signal. The transducer detects the specific molecular interaction and converts the signal for electrochemical, optical, mass, thermal or other measurements. The majority of the biosensor techniques can be grouped into two categories, based on labeling and label-free⁵ interrogation, respectively. The earliest types of sensors require radio active, enzymatic, fluorescent or electrochemical labels to report the binding event. However, there is an increasing awareness of novel techniques that do not require labeling of the ligand or the receptor, such as optical sensors, electrochemical sensors, acoustic sensors, mass spectrometry, calorimetry, etc. The label-free sensors are obviously advantageous in avoiding the additional cost/time. In particular, the concept eliminates undue

detrimental effects from the labels that may interfere with the fundamental interaction. There are an increasing number of commercially available instruments⁶ that enable label-free screening for virtually any receptor–analyte complex. Calorimetry sensors are even providing the “gold standard” in the measurement of interaction thermodynamics.⁷ However, although the sensitivity of label-free biosensors has been greatly boosted by enormous engineering efforts, it can never compete with that of the labeling biosensors. For example, single-molecule spectroscopy has been widely realized at room temperature by laser-induced fluorescence.⁸ Also, the labeling by gold nano-particles has also gained great reputation in ultra-trace detection of biomolecules.⁹ Since both labeling and label-free technique have their advantage and limitation (cf. Figure 1.1), both techniques are driven forward in parallel in order to accelerate the acceptance of biosensors in a larger abundance of areas.

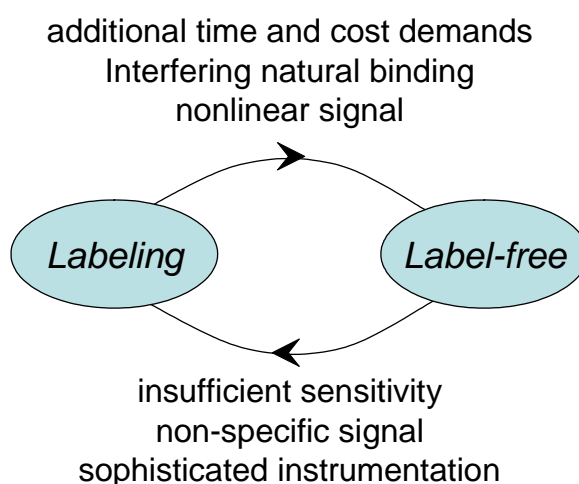


Figure 1.1: The advantages and disadvantages of labeling and label-free biosensing techniques.

1.2 Surface plasmon based (sensing) techniques

A surface plasmon resonance (SPR) is a collective electron resonance, pinned at the interface between two optically dissimilar materials, one of which is a metal (e.g. Au, Ag, Cu).¹⁰ SPR is being explored for its potential in optics, magneto-optic data storage, microscopy and solar cells, as well as being used to construct sensors for detecting biologically interesting molecules. Theoretically and experimentally, the following distinctive features of SPR have been discovered and proven to be valuable:

- a) It is a short range phenomenon, with the electric field decaying with $1/e$ distance of hundreds of Angstroms \sim nanometers in the adjacent media.
- b) It provides an enhanced electromagnetic field at the interface;
- c) It propagates with high attenuation owing to the high loss in the metal.
- d) It is mostly p-polarized, giving spatial orientation information about the dipoles with which the SP interacts.

Based on feature (a), SPR becomes an optical technique that uses evanescent waves to measure changes in refractive index very close to the sensor surface. A great deal of work has been done in the exploitation of SPR for optical biosensing, since its first thin-film sensing was conducted in the late seventies.¹¹ In 1990, the first commercial SPR biosensing instrument was introduced by Biacore.¹² Subsequently, a number of commercial SPR biosensor instruments are available.⁶ It is becoming a mature biophysical method and a leading technology for characterizing biomolecular interactions.

Feature (b), the enhancement in the localized field has long been recognized and used for different spectroscopies of adsorbing species, including Raman scattering, fluorescence, nonlinear optical response (e.g. second order nonlinear polarizability), infrared-absorption and diffraction (scattering), etc. Correspondingly, the techniques are named to be surface plasmon enhanced Raman scattering (SE-SERS),¹³ surface plasmon enhanced fluorescence spectroscopy (SPFS),¹⁴ surface-enhanced second harmonic generation (SHG),¹⁵ surface-enhanced infrared absorption (SEIRA)¹⁶ and surface plasmon enhanced diffraction (SPD).¹⁷

Feature (c) offers a lateral resolution of SPR at the micrometer scale for thin-film imaging purposes. Following the early work by Knoll et al,¹⁸ surface plasmon microscopy (SPM) has been well-engineered¹⁹ and even commercialized.²⁰ SPM is also showing its compatibility to the biochip technology.

Feature (d) has not gained as much attention as that of (a), (b) and (c). However, there are still a few efforts²¹ reported, using SPFS or SEIRA to take full advantage of the p-polarized excitation source.

1.3 Aim of the study

The aim of this study is divided into two parts of different scope. In the first part, an in-depth understanding of surface plasmon fluorescence spectroscopy (SPFS) in immuno-interaction studies is provided (chapter 4) and an SPFS immunoassay established (chapter 5). In the second

part, a completely new label-free biosensing strategy, i.e. a surface plasmon diffraction sensor (SPDS), is developed (chapter 6) and used for biomolecular characterizations.

The SPFS technique was firstly introduced by our group in 2000.¹⁴ Although extensive DNA hybridization studies have been carried out since then,²² applications for protein systems still remained unexplored. Normally possessing a larger size than oligonucleotides, the protein binding can be visible in both the SPR and the fluorescence channel of SPFS. This dual-channel sensing ability of SPFS can be fully used for uncovering more interfacial information. On the other hand, besides sharing the same features known from the DNA work, the SPFS protein study introduces new features and difficulties, such as non-specific protein binding (NSB), multiple labels in protein, an SPR field ‘detuning’ effect, etc. Therefore, the study starts with a thorough investigation of protein-interaction monitored by SPFS based on functional self-assembled monolayer systems, depicted in chapter 4.

Based on the understanding that fluorescence suffers severe quenching if the fluorophores are too close to the metal, a three-dimensional (3D) functional matrix is introduced to SPFS, in order to extend the interaction platform out of the ‘quenching’ region. This strategy significantly enhanced the limit of detection (LOD) of SPFS, which is carefully estimated by applying a simple ‘two-component’ immuno-interaction. As an attempt aiming towards clinical applications of SPFS, the SPFS-based PSA sandwich assay is demonstrated, even in the presence of human plasma. All this sensing work based on a 3D matrix will be demonstrated in chapter 5.

Finally, the development of a new label-free biosensing strategy will be shown in chapter 6. This biosensor is based on the biological extension of the surface plasmon enhanced diffraction (SPD) phenomenon, introduced in the late eighties by our group¹⁷. At first, the physical features of SPD, such as the enhancement in diffraction intensity, quadratic signal-relation, the self-referencing property, etc., are described one-by-one mostly using biological systems. Subsequently, two sensing examples respectively for immuno-substances (hCG, human chorionic gonadotropin) and oligonucleotides are provided, showing excellent performance of the diffraction-based sensor.

2 Theory

2.1 Surface plasmon optics

Surface plasmon resonance spectroscopy (SPR, SPS or SPRS) is a century-old technique dating back to the finding of Wood's anomaly seen in for the reflected light from diffraction gratings.²³ It was later investigated in 1957 by the pioneering work of Ritchie.²⁴ Since then, there has been a considerable amount of work done on the fundamental properties of plasmons and the SPR theory has been well established.¹⁰ There are also numerous examples of their applications, which mainly focus on developing a wide variety of optical sensors.

Surface plasmons (SPs) are electromagnetic waves that propagate along the surface of a conductor, usually a noble metal (such as Au, Ag, Pt, etc.). They are essentially light waves that are bound to the surface by the interaction with the free electrons of the conductor. As a result, the free electrons respond collectively by oscillating in resonance with the light wave. The resonant interaction between the surface charge oscillation and the electromagnetic field of the light constitutes the SPs and gives rise to its unique properties.

2.1.1 Maxwell equations – a starting point:

The Maxwell equations are given by

$$\begin{aligned}\nabla \cdot \vec{D} &= 0 & \nabla \times \vec{E} &= -\frac{\partial \vec{B}}{\partial t} \\ \nabla \cdot \vec{B} &= 0 & \nabla \times \vec{H} &= \frac{\partial \vec{D}}{\partial t}\end{aligned}\quad \text{--- 2.1}$$

Here, \vec{E} is the electric field (Vm^{-1}) and \vec{H} is the magnetic field (Am^{-1}). They are related to the electric displacement (or the dielectric flux density or electric flux density) \vec{D} (Cm^{-2}) and magnetic flux density (or magnetic induction) \vec{B} (T: tesla = $\text{NA}^{-1}\text{m}^{-1}$)

$$\begin{aligned}\vec{D} &= \epsilon\epsilon_0\vec{E} \\ \vec{B} &= \mu\mu_0\vec{H}\end{aligned}\quad \text{--- 2.2}$$

where ϵ and ϵ_0 are the dielectric constant (without dimension) and the electric permittivity of free space, respectively. μ and μ_0 are the magnetic permeability (without dimension) and the magnetic permeability of free space, respectively.

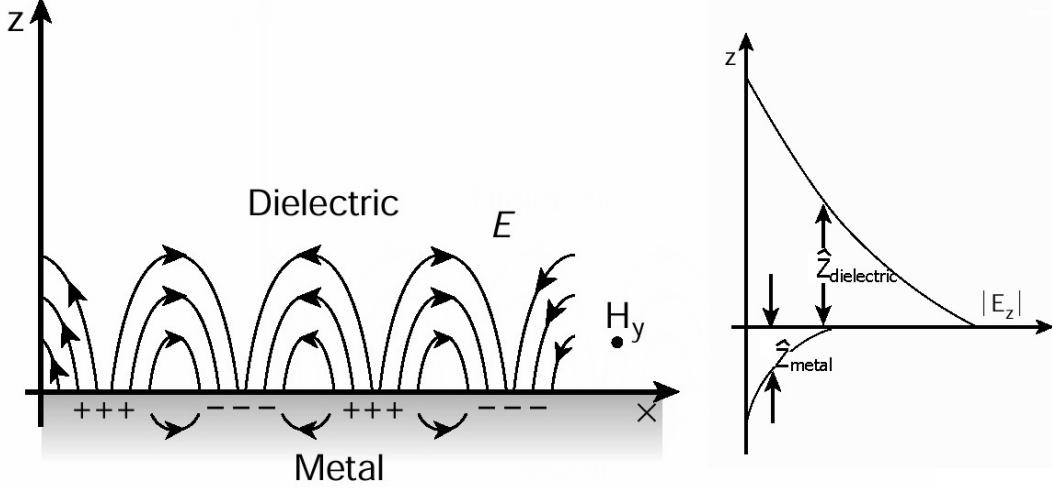


Figure 2.1: The charges and the electromagnetic field of SPs propagating on a surface in the x-direction are shown schematically in the left panel. The exponential dependence of the field E_z on both $+z$ and $-z$ sides is seen on the right panel.

2.1.2 Wave equations and dispersion relation of surface plasmons:

The solution of Maxwell equations for the electric field \vec{E} , in the case of plane waves, is presented by the equation:

$$\vec{E} = \vec{E}_0 e^{i(\vec{k} \cdot \vec{r} - \omega t)} \quad \text{--- 2.3}$$

Where \vec{E}_0 is the electric field amplitude, \vec{r} is the position vector, ω is the angular frequency ($\omega = 2\pi f$, f : frequency), t is the time, and \vec{k} is the wavevector which is in the direction of the propagation. The magnitude of \vec{k} is given by:

$$|k| = \sqrt{\mu\mu_0\epsilon\epsilon_0\omega^2} \quad \text{--- 2.4}$$

in vacuum (or air as a first approximation), $\epsilon=1$, $\mu=1$ and $\lambda = 2\pi c/\omega$, $k=2\pi/\lambda=\omega/c$, then:

$$c = 1/\sqrt{\mu_0\epsilon_0} \quad \text{--- 2.5}$$

The electron charges on a metal boundary can perform coherent oscillations, which are called surface plasmon polaritons (SPPs or SPs). These charge oscillations can be localized in the z -

direction, and accompanied by a mixed transversal and longitudinal electromagnetic field that propagates along the x-axis and vanishes at $|z| \rightarrow \infty$ on both sides of the metal/dielectric interface, and has its maximum at $z = 0$ (cf. Figure 2.1). The plasmon waves have p-character because the surface charges induce the discontinuity of the electromagnetic field in the z-direction, which does not apply for s-waves (no \vec{E}_z component). In other words, only transverse magnetic plane waves (i.e. TM waves) can be applied to excite SPPs. Considering the dielectric ($\epsilon_1 > 0$, medium 1)/metal ($\epsilon_2 = \epsilon_2' + i\epsilon_2''$, medium 2) interface, the electromagnetic fields on both sides are expressed as:

$$\begin{aligned}
 z > 0 \quad & H_1 = (0, H_{y1}, 0)e^{i(k_{x1}x + k_{z1}z - \omega t)} \\
 & E_1 = (E_{x1}, 0, E_{z1})e^{i(k_{x1}x + k_{z1}z - \omega t)} \\
 z < 0 \quad & H_2 = (0, H_{y2}, 0)e^{i(k_{x2}x - k_{z2}z - \omega t)} \\
 & E_2 = (E_{x2}, 0, E_{z2})e^{i(k_{x2}x - k_{z2}z - \omega t)} \quad \text{--- 2.6}
 \end{aligned}$$

k_{x1} and k_{x2} are the wavevectors in x-directions and k_{z1} and k_{z2} the ones along the z-axis. Considering the continuity relations of the in-plane components:

$$E_{x1} = E_{x2}, \quad H_{y1} = H_{y2} \quad \text{--- 2.7}$$

and inserting (2.7) into (2.6) yields:

$$k_{x1} = k_{x2} = k_x, \quad \text{--- 2.8}$$

inserting (2.6) into (2.1), together with (2.5) one obtains:

$$\begin{aligned}
 +k_{z1}H_{y1} &= -\frac{\omega}{c}\epsilon_1 E_{x1} \\
 +k_{z2}H_{y2} &= +\frac{\omega}{c}\epsilon_2 E_{x2} \quad \text{--- 2.9}
 \end{aligned}$$

Together with the continuity relations (2.7), one obtains the dispersion relation of SPPs:

$$\frac{k_{z1}}{\epsilon_1} + \frac{k_{z2}}{\epsilon_2} = 0 \quad \text{--- 2.10}$$

This reveals that SPPs can only exist at the interface between two materials that have dielectric constants of opposite sign, e.g., a metal/dielectric interface.

The wavevector k_i can be decomposed into k_{xi} and k_{zi} , together with (2.8), one obtains:

$$k_x^2 + k_{zi}^2 = \epsilon_i \left(\frac{\omega}{c}\right)^2 \quad \text{--- 2.11}$$

From (2.10) together with (2.11), one yields the dispersion relation of SPPs in another format:

$$k_x = \frac{\omega}{c} \left(\frac{\varepsilon_1 \varepsilon_2}{\varepsilon_1 + \varepsilon_2} \right)^{1/2} \quad \text{--- 2.12}$$

In the case of the dielectric ($\varepsilon_1 > 0$, medium 1)/metal ($\varepsilon_2 = \varepsilon_2' + i\varepsilon_2''$, medium 2) interface, and assuming $\varepsilon_2'' < |\varepsilon_2'|$, the complex k_x is expressed by:

$$k_x = k_x' + ik_x'' \quad \text{--- 2.13}$$

with

$$k_x' = \frac{\omega}{c} \left(\frac{\varepsilon_1 \varepsilon_2'}{\varepsilon_1 + \varepsilon_2'} \right)^{1/2} \quad \text{--- 2.14}$$

$$k_x'' = \frac{\omega}{c} \left(\frac{\varepsilon_1 \varepsilon_2'}{\varepsilon_1 + \varepsilon_2'} \right)^{3/2} \frac{\varepsilon_2''}{2\varepsilon_2'^2} \quad \text{--- 2.15}$$

2.1.3 Spatial extensions of SP fields and propagation of SPs

From (2.11) and (2.12) and assuming $|\varepsilon_2'| > \varepsilon_1$, one obtains:

$$k_{z1}^2 \approx \left(\frac{\omega}{c} \right)^2 \left(\frac{\varepsilon_1^2}{\varepsilon_1 + \varepsilon_2'} \right) \quad \text{--- 2.16}$$

$$k_{z2}^2 \approx \left(\frac{\omega}{c} \right)^2 \left(\frac{\varepsilon_2'^2}{\varepsilon_1 + \varepsilon_2'} \right) \quad \text{--- 2.17}$$

Since $\varepsilon_2' + \varepsilon_1 < 0$, the wavevectors k_{zi} is purely imaginary. The optical fields decay exponentially as $E_z \propto e^{-|k_{zi}||z|}$ into their respect medium.

The distance (depth) where the field falls to $1/e$, becomes

$$\hat{z} = \frac{1}{|k_{zi}|} \quad \text{--- 2.18}$$

The intensity of SPs propagating along the metal/dielectric interface (x -axis) decreases as $E_x \propto e^{-2|k_x''||x|}$. Therefore, the propagation length L_x

$$L_x = \frac{1}{2|k_x''|} \quad \text{--- 2.19}$$

can be defined, which influences the lateral resolution for surface plasmon microscopy applications. Also for 633 nm light on the gold/air interface, $L_x = 10 \mu\text{m}$. For the same light on the

gold/water interface, $L_x = 4 \mu\text{m}$. The damping of the electromagnetic field causes heat and dissipated into the metal and the dielectric.

2.1.4 Excitation of SPs by light

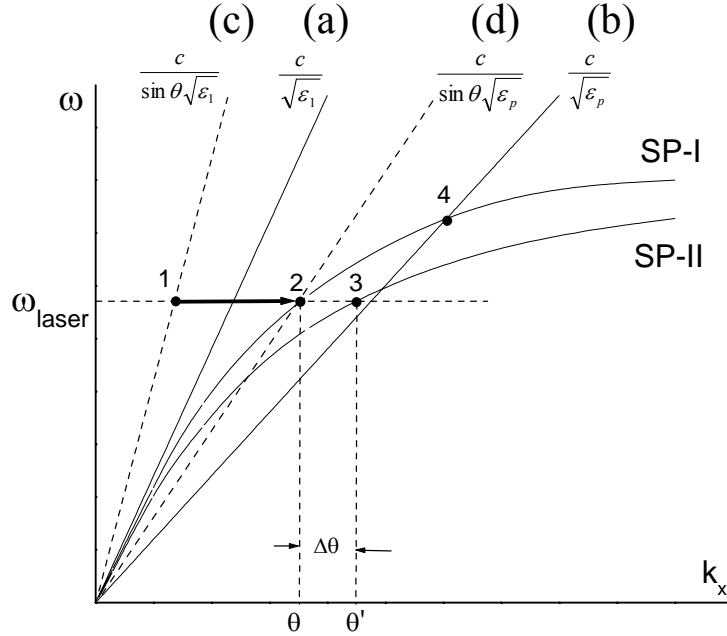


Figure 2.2: The dispersion relation of free photons in a dielectric (a), and in a coupling prism (b) with $\epsilon_p > \epsilon_1$, compared to the dispersion relation non-radiative surface plasmons at the metal/dielectric interface before (SP-I) and after (SP-II) the adsorption of an additional dielectric layer.

The dispersion relation of a free photon in a homogenous dielectric (ϵ_1) is

$$k_{ph} = \frac{\omega}{c} \sqrt{\epsilon_1} \quad \text{--- 2.20}$$

which is always smaller than the wavevector of SPs at the dielectric/metal interface, k_{spp} (cf. k_x in (2.12)). This is shown graphically as $\omega(k_x)$ plots in Figure 2.2 (cf. curve (a) and curve SP-I). The $\omega(k_x)$ curve of SPs approaches asymptotically the dispersion curve of the free photon ($|\epsilon_2'| \gg \epsilon_1$ for $\omega \rightarrow 0$) with no intersection of the curves. Thus, SP cannot directly transform into light on a smooth surface, i.e., it is a non-radiative wave. Another consequence is that, the p-polarized light cannot be used to excite SPs directly, due to its insufficient k_{ph} . Experimentally, there are two coupling techniques to enhance k_{ph} , namely, the prism coupling and the grating coupling, in order to match the optical momentum at the interface.

2.1.4.1 Prism coupling

The light travels through a half-cylindrical prism (ϵ_p), with its k_{ph} being enhanced to $\frac{\omega}{c}\sqrt{\epsilon_p}$ by a factor of $\sqrt{\epsilon_p/\epsilon_1}$. The dispersion curves before and after the enhancement by the prism are shown as curve (a) and (b) in Figure 2.2, with a slope of $\frac{c}{\sqrt{\epsilon_1}}$ and $\frac{c}{\sqrt{\epsilon_p}}$, respectively. At a certain wavelength of the laser (ω_{laser}), the dispersion curve of SP-I determines a laser incident angle θ for the excitation of SPs (cf. curve (d)). This occurs if the projection of the wavevector $\frac{\omega}{c}\sqrt{\epsilon_p}$ on the x-axis matches the x-component of k_{spp} .

$$\frac{\omega_{laser} \sin \theta}{c} \sqrt{\epsilon_p} = k_{SPP,x} \quad \text{--- 2.21}$$

As is shown in Figure 2.2, the enhanced wavevector Δk_x from point 1 to 2 is the contribution from the prism. The excitation of SPs is recognized as a minimum in the totally reflected intensity, which can be quantitatively described by Fresnel's equations for multi-layer system,²⁵ with the aid of the transfer matrix algorithm.²⁶

Two prism coupling geometries are possible, which are called Otto configuration²⁷, and Kretschmann-Raether configuration²⁸, respectively. Various shapes of prisms can be used for exciting SPs, such as triangular, half cylinder prisms, hemisphere prisms. For simplicity, in the following discussions we will use half cylinder, since the light incident angle will not be changed by the refraction at the air/prism interface. For the triangle prism, the corresponding angle conversion should be considered.

For the Otto configuration (panel (A) in Figure 2.3), the metal surface is separated by an air or dielectric gap at a distance of sub-micrometer from the prism. The resonant excitation of SPPs is achieved on the metal surface through the gap where the evanescent fields from both sides of the gap overlap. With the experimental parameters listed below the schematic, a Fresnel simulation yields a deep and sharp minimum in the angular-dependent reflectivity curve due to the occurring of the surface plasmon resonance.

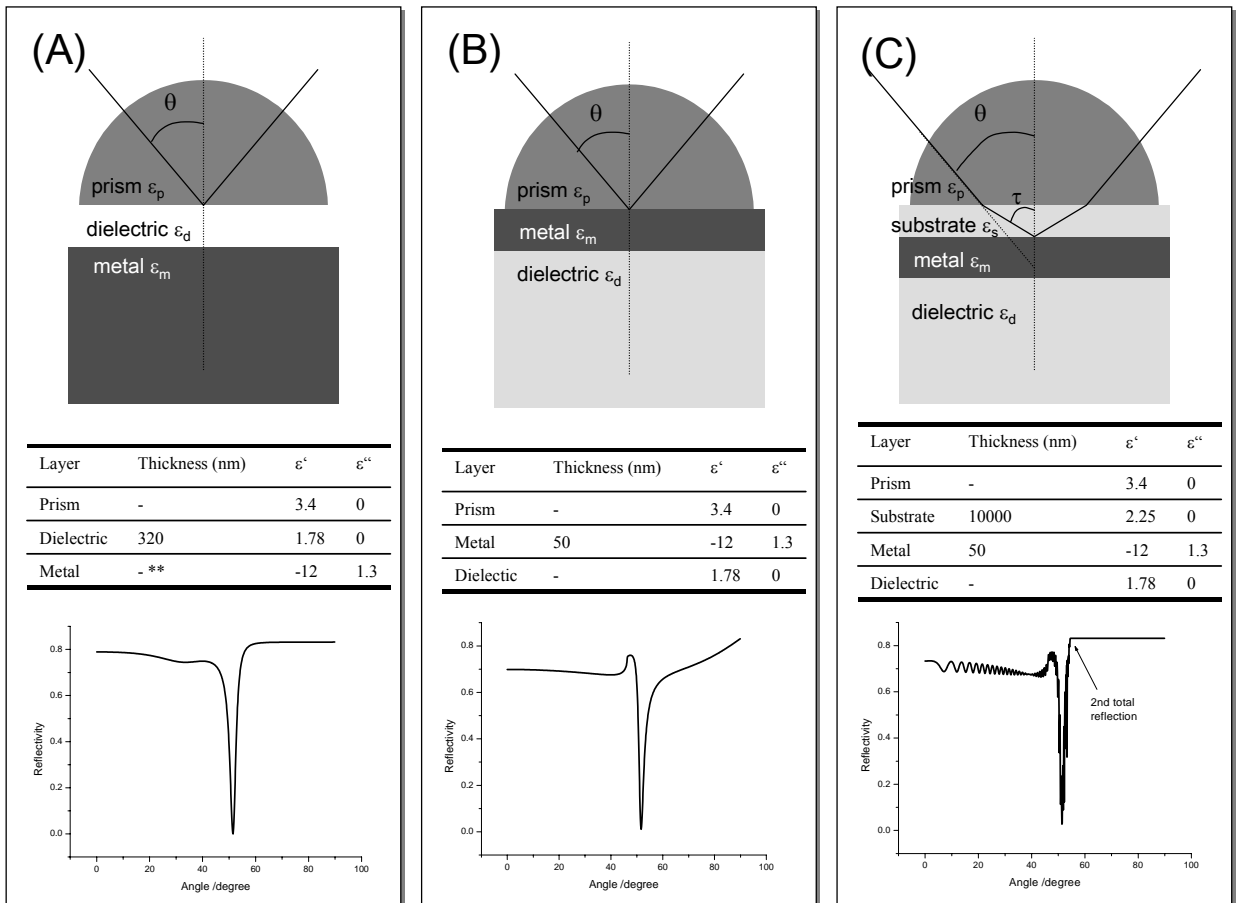


Figure 2.3: Prism coupling geometries and their corresponding angular-dependent reflectivity simulations for (A) Otto configuration, (B) Kretschmann-Raether configuration, (C) alternative Kretschmann-Raether configuration with a refractive-index-mismatch between the prism and the substrate.

The Kretschmann-Raether configuration is more versatile because it is experimentally less difficult to realize. As shown in panel (B) of Figure 2.3, it requires a finite thickness d_m of the metal layer, which is directly attached to the base of the prism. The thickness d_m influences the coupling angle θ , as well as the coupling efficiency, e.g., the minimum reflectivity. This dependence can be simulated by Fresnel's equations using the transfer matrix methods. As a general understanding, it is a result of the destructive interference between the partially reflected light wave from the prism/metal interface and the re-radiated light wave from the metal/dielectric interface. A Fresnel simulation of the usual experimental conditions is also shown.

For a more convenient experimental handling, the metal layer is usually deposited on a glass substrate with the same refractive index as that of the prism. Then an index-matching fluid couples the prism and the substrate optically. For practical reasons (cf. chapter 5), substrates with lower refractive indices are sometimes coupled to the high index prism for surface plasmon

excitation. The refractive index mismatch between the prism and the substrate brings extra features in the angular reflectivity curve, as shown in panel (C) of Figure 2.3. For example, the reflectivity curve is superimposed by an angular-dependent interference pattern, which is caused by the extra reflection beam at the prism/substrate interface interfering with the beam from the substrate/metal interface. Another point is that, at an angle slightly higher than the SPR minimum angle, a second total reflection occurs at the prism/substrate interface and the SPR phenomenon vanishes abruptly. However, the surface plasmon dip still appears at the same angle as if the extra layer of the substrate does not exist (cf. the reflectivity curve in panel (B)). In order to elucidate these phenomena, we refer to the reflection/transmission law at dielectric interfaces.

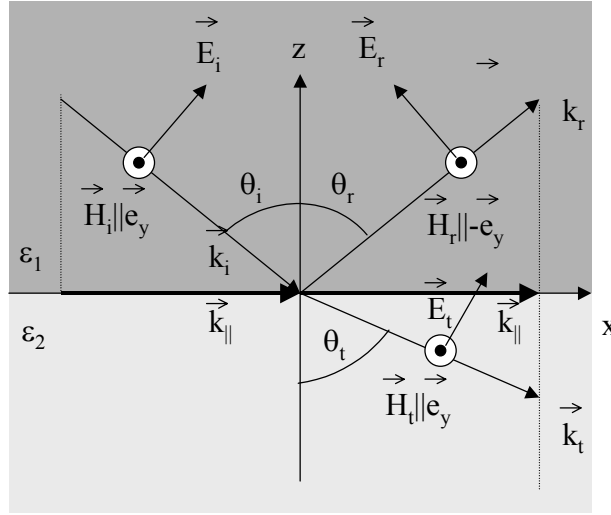


Figure 2.4: Schematic picture of an incident, a reflected and a transmitted transverse magnetic polarized plane wave at an interface between two different dielectric media. The subscripts stand for ‘incident’ (i), ‘reflected’ (r), ‘transmitted’ (t). The plane of incidence is determined by the wavevector of the incident beam and the surface normal. Note that the in-plane components of the wavevectors are equal.

As shown in Figure 2.4, at the interface of two dielectric media with no adsorption ($n_1 = \epsilon_1^{1/2}$, $n_2 = \epsilon_2^{1/2}$), the incident wave (e.g. a TM mode) is subjected to reflection and transmission. An important characteristic is the conservation of the in-plane wavevector k_{\parallel} , i.e., the wavevector parallel to the interface.

$$k_i \sin \theta_i = k_r \sin \theta_r = k_t \sin \theta_t \quad \text{--- 2.22}$$

This is schematically presented in the Figure 2.4. Although the modulus of \vec{k}_t for $n_1 > n_2$ is smaller, it still yields for the transmission beam the same projection k_{\parallel} on the x-axis due to the increased θ_t . Therefore, SPR resonance is possible at the same angle (cf. Equation 2.21).

Moreover, with Snell's law

$$n_1 \sin \theta_i = n_2 \sin \theta_t \quad \text{--- 2.23}$$

for $n_1 > n_2$, $\theta_t = 90^\circ$, total reflection (i.e. no transmission light) will occur at a critical angle θ_c , with

$$\theta_c = \sin^{-1} \frac{n_2}{n_1} \quad \text{--- 2.24}$$

Thus, with the same n_1 , θ_c increases with increasing n_2 . Using this equation, those two total reflection angles can be precisely positioned.

2.1.4.2 Grating coupling

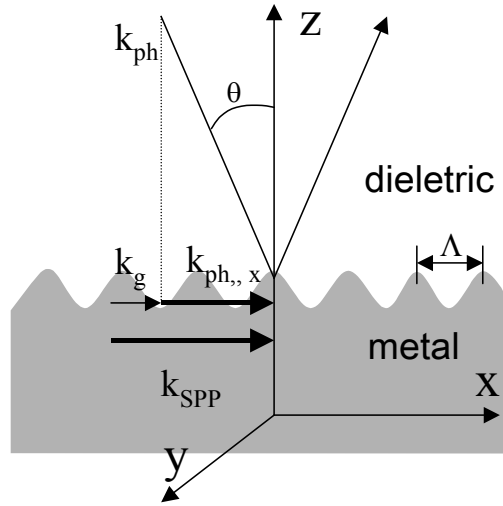


Figure 2.5: Schematic representation of SPR coupling via a sinusoidal diffraction grating.

As is indicated mathematically by a Rayleigh expansion (approximation for shallow grating)²⁹, the surface periodic structure can also enhance the wavevector of the incident light for resonance coupling.¹⁰ As shown in Figure 2.5, light ($k_{ph} = \omega/c$) from the dielectric (ϵ_d) hits a metallic grating (ϵ_m) with a grating constant Λ at an incident angle θ . Assuming the dispersion property of the SP wave is not disturbed by the corrugated surface, the momentum matching condition can be written as:

$$k_x = k_{ph,x} \pm mg = \frac{\omega}{c} \sqrt{\epsilon_d} \sin \theta \pm mg = \frac{\omega}{c} \sqrt{\frac{\epsilon_d \epsilon_m}{\epsilon_d + \epsilon_m}} = k_{sp,x} \quad \text{--- 2.25}$$

with m the order of diffraction and $g = 2\pi/\Lambda = k_g$, the grating wavevector. The resonance can be also observed as a minimum of the reflected light as a function of incident angle or wavelength. Note that the grating constant Λ should be within the same order-of-magnitude as the wavelength

of the incoming light, given the fact that SPR coupling via the first diffraction order is significantly more efficient than via higher orders. A shallow grating with amplitude of several tens of nanometers is proven to be sufficient for efficient SPR coupling.

2.1.5 SPR response to a thin film deposition

The evanescent field of a surface plasmon wave reaches the maximum at the metal-dielectric interface, and decays exponentially into the dielectric medium at a distance of several hundreds of nanometers. Therefore the surface plasmon resonance technique is extremely sensitive to the changes of the optical properties of the adjacent dielectric medium. This means that a variation of the ε_l in equation (2.12) changes $k_{spp,x}$, and consequently, changes the surface plasmon resonance angle elucidated by equation (2.21). On the other hand, the addition of a thin (i.e. thickness d much smaller than the SP decay length along the z axis) and non-adsorbing layer with different dielectric constant ($\varepsilon_f \neq \varepsilon_l$) also induces a change in the overall dielectric constant integrated over the evanescent field, therefore shifts the SPR angle. The mean refractive index within the evanescent field increases assuming $\varepsilon_f > \varepsilon_l$. Therefore, the dispersion relation of equation (2.12) shifts to larger wavevector, depicted as curve SP-II in Figure 2.2. Consequently, a higher light incident angle $\theta' > \theta$ is required to fulfill the resonance criterion. For a thin, non-adsorbing layer defined by a thickness d and a refractive index n , the resonant angle displacement $\Delta\theta$ is linear to the optical thickness nd of the layer:

$$\Delta\theta \propto n \cdot d \quad \text{--- 2.26}$$

There are various methods proposed, to separate the two distinct parameters (n and d) within the optical thickness value, e.g., by measuring the SPR in a series of bulk media with different refractive indices³⁰ or under multiple light wavelengths.³¹ If the studied material forms a thick film, a number of waveguide modes can be excited which provide adequate information for resolving n and d .³² However, for biomolecules, this optical picture is usually irrelevant. SPR angle displacement $\Delta\theta$ are directly correlated with the molecular surface concentration. For example, using radioisotope labeled protein, it has been found that $\Delta\theta$ depends linearly on the protein concentration (mass per area) and the dependence is irrelevant to the type of proteins studied.³³ Usually, a layer of biomolecules can be treated as non-adsorbing layer. However, if the biomolecules carries external labels (e.g. gold nanoparticles, fluorescent dye, etc.) the resulting thin layer becomes adsorbing, which more or less distorts the property of SPR.³⁴

2.1.6 Field enhancement

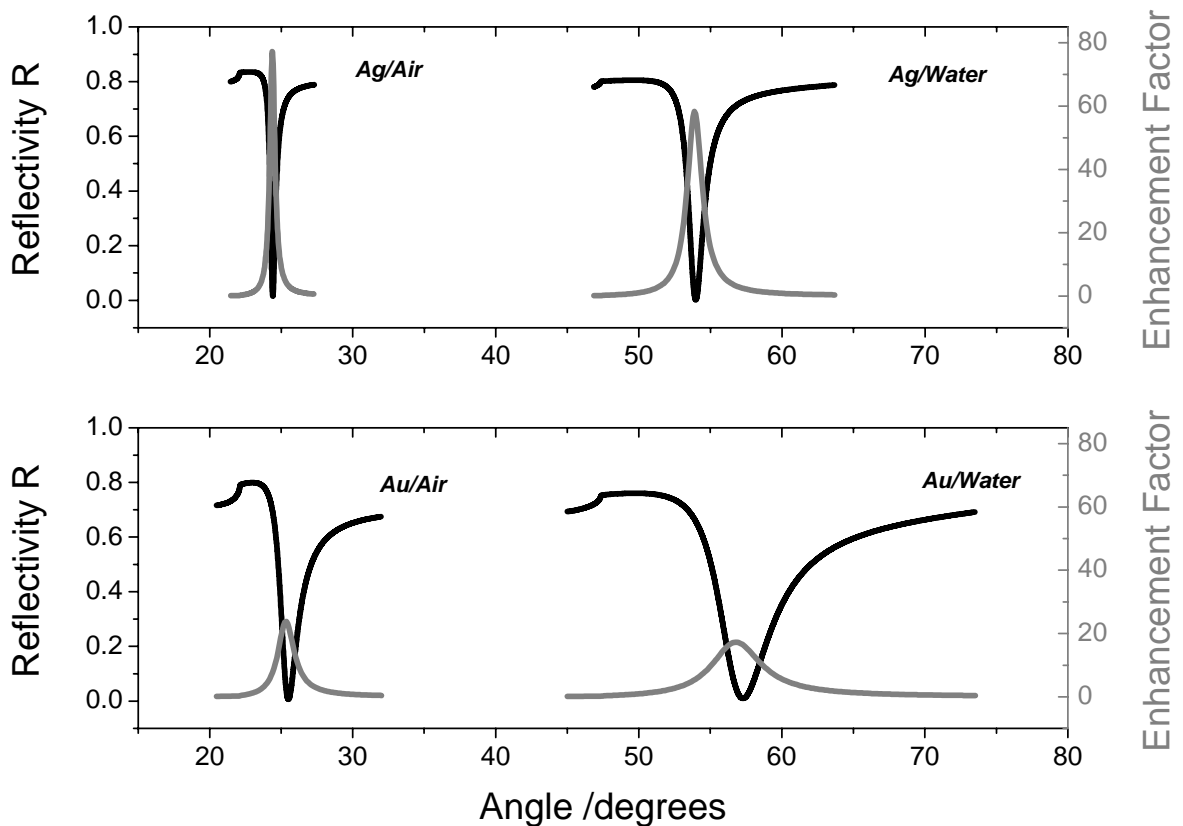


Figure 2.6: Simulation curves of the reflectivity and the relative field intensity as a function of the light incident angle on three-phase systems (prism/Ag/air, prism/Ag/water, prism/Au/air, prism/Au/water). Calculation parameters: right-angled prism ($\epsilon=3.4$), Ag ($\epsilon=-17+0.7i$), Au ($\epsilon=-12+1.3i$), air ($\epsilon=1$), water ($\epsilon=1.78$), HeNe laser (633 nm).

Angle-scan SPR curves of three-phase systems (prism/Ag/air, prism/Ag/water, prism/Au/air, prism/Au/water) in the Kretschmann-Rather ATR configuration calculated by Fresnel equation are shown in Figure 2.6. All the curves show a critical angles θ_c and a resonance angle θ_{SPR} . The critical angle θ_c , whose value is determined only by the refractive indices of the prism and the dielectric medium, indicates the onset of the attenuated total reflection (ATR) phenomenon. The resonance angle, on the other hand, indicates the condition at which the wavevector of the incident light matches that of the surface plasmon wave supported by the metal. At the resonance angle, almost all of the energy of the incident radiation is converted into surface plasmon excitation and, thus, the electromagnetic field at the interface is greatly enhanced. As a result, a substantial attenuation of the reflectance is observed. The enhancement can be also depicted in a more obvious manner by applying energy conservation.¹⁰

For p-polarized radiation, the electric field has two components (in x -direction and in z -direction) while the magnetic field has only one component (in y -direction). Since both fields are tightly correlated, for simplicity the field-enhancement estimation is calculated for the magnetic field. The angular dependent magnetic field intensities are normalized to the incident intensity and are plotted against their corresponding reflectivity curves in Figure 2.6. As shown, every field intensity reach a maximum near the reflectivity minimum. The enhancement factors are found to be 77, 58, 24, 17 for the interfaces of *Ag/air*, *Ag/water*, *Au/air*, *Au/water*, respectively. The significantly higher enhancement factor on silver is attributed to its smaller imaginary dielectric constant ϵ'' , which results in lower dissipation of optical field. The SP field is pushed more into the metal by the optically denser dielectric (e.g. water) than the air, therefore is more dissipated. Consequently, the field enhancement is lower in metal/water than in metal/air.

A closer look reveals that the angle of the maximum field-intensity slightly shifts toward a smaller angle of the reflectivity minimum angle. This phenomenon can be explained by considering the system as a resonator driven by the incoming light.^{14,35} The imaginary dielectric constant ϵ'' of the metal is the lossy component of the resonator which separates the coincidence of the resonance. The larger is the ϵ'' , the greater is the separation, which coincides with the factor that the angular separation is smaller on Ag than on Au.

2.2 Surface Diffraction

2.2.1 Diffraction from a smooth, sinusoidal surface

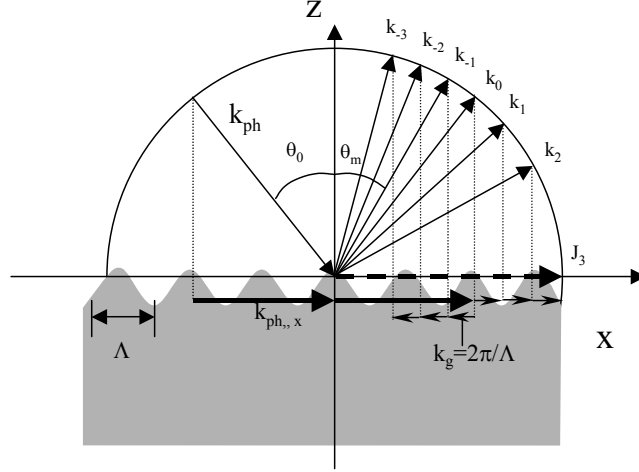


Figure 2.7: Schematic sketch of a reflective diffraction of an incident light by a surface grating structure

Ordered scattering from surface with a periodic structure is called diffraction. Figure 2.7 gives a schematic sketch of the diffraction of p -polarized light on a sinusoidal grating. The p -polarized light is incident in the x - z plane at angle θ_0 with a wavelength λ . The grating/air interface plane is oriented perpendicular to the x - z plane. The Rayleigh expansion²⁹ gives the description of the diffracted electric field in the air region:

$$E(x, z) = \sum_{m=-\infty}^{\infty} E_m \cdot e^{i(\alpha_m \cdot x \pm \beta_m \cdot z)} \quad \text{--- 2.27}$$

with

$$\alpha_m = k_{ph} \sin \theta_m + m k_g$$

$$\beta_m = \sqrt{k_{ph}^2 - \alpha_m^2}$$

$$k_g = 2\pi / \Lambda$$

where θ_m is the angle of the m th order of the diffraction peak relative to the z -axis, k_{ph} is the wavevector of the incident light with $k_{ph} = 2\pi/\lambda$, and Λ is the wavelength of the grating.

If m is large enough, α_m becomes larger than k_{ph} . Consequently, k_z becomes purely imaginary, representing an evanescent wave $E_m e^{-\beta_m z} e^{i\alpha_m x}$, propagating along the x -axis but damped along the z -axis. Otherwise, each term of the expansion represents a propagating plane wave, monitored as diffraction maximum. From Figure 2.7 one can see this by the superimposing of wavevectors. The x component of the k_{ph} gains discrete momentum mk_g from the periodic grating structure, which gives rise to the discrete deviation the angle θ_m of the m th diffraction order from the zeroth diffraction order, i.e., the spectrally reflected beam. If $k_{ph} \sin \theta_m + mk_g \geq k_{ph}$, no real z -component of the photon can exist. Consequently, the light couples into the grating.

Clearly, for those radiative diffraction orders, the positions of the diffracted orders are given by:

$$\sin \theta_m = \sin \theta_0 + m\lambda / \Lambda \quad \text{--- 2.28}$$

This is well known as the grating equation. Note that the spacing of the diffracted orders is dependent on the light wavelength and the grating periodicity, but is not on the grating amplitude and light power. For a grating with periodicity of $\Lambda \gg \lambda$ (note: this is different to the grating-coupled SPR case, where Λ and λ should be close for an efficient coupling), the spacing of the diffracted orders near the zeroth order is pseudo-periodic, i.e., $\theta_l - \theta_0 = (\theta_m - \theta_0) / m$.

The intensities (powers) of each diffraction order I_m depend on the grating amplitude A and the light power I_0 and are also found via the diffraction theory. Solutions may be divided into the classes of scalar and vector calculations that ignore and include the effects of light polarization, respectively. Most scalar diffractions yield diffracted orders I_m that are proportional to a summation of squared Bessel functions.³⁶ Most of the calculations can be reduced to a simplified equation for the low-angle diffraction on ‘smooth’ gratings ($A \ll \lambda$).

$$\frac{I_m}{I_i} \propto \left[J_n \left(\frac{2\pi A}{\lambda} \right) \right]^2 \quad \text{--- 2.29}$$

We can see that the diffraction intensity has a quadratic relationship with the grating amplitude A . A more accurate vector perturbation result, developed in the radar literature³⁷ and based on earlier diffraction calculations in 1907,³⁸ has been introduced by Church³⁹. This relationship is commonly referred as the Rayleigh-Rice vector perturbation theory. The theory considers different situation of two orthogonal polarizations, i.e., TM and TE polarization, respectively. In either case, the quadratic relationship between I_m and A is preserved. In a more general picture, for periodic modulations with index-of-refractive amplitude $(\Delta n(\lambda)d)$ and adsorption coefficient amplitude $(\Delta k(\lambda)d)$, but with the material being only weakly adsorbing, the Equation 2.29 can be expanded for the first several diffraction orders⁴⁰:

$$\eta = \frac{I_m}{I_i} \propto \left(\frac{\pi \Delta n d}{\lambda} \right)^2 + \left(\frac{\Delta k d}{4} \right)^2 \quad \text{--- 2.30}$$

where, η is called the diffraction efficiency of the m th diffraction order.

2.2.2 Fourier diffraction optics

In the Fraunhofer approximation, a plane electromagnetic wave passing a transmission function $\bar{\tau}(\bar{v})$, the field distribution becomes:

$$\bar{T}(\bar{u}) = C \int \bar{\tau}(\bar{v}) e^{i2\pi(\bar{u} \cdot \bar{v})} d\bar{v} \quad \text{--- 2.31}$$

which is the Fourier transform of the transmission function with respect to position \bar{u} . For gratings, they can be considered as finite one-dimensional periodic optical modulations. The transmission function may be expressed as the convolution of a single gate function $g(x)$ and a finite array of delta functions with periodicity of Λ .⁴¹

$$\tau(x) = \sum_{n=-(N-1)/2}^{(N-1)/2} \delta(x - n\Lambda) * g(x) \quad \text{--- 2.32}$$

with

$$\delta(x) = (x - \chi) = \begin{cases} 0 & x \neq \chi \\ \infty & x = \chi \end{cases},$$

$$\int_{-\infty}^{+\infty} \delta(x - \chi) dx = 1,$$

$$g(x) = \begin{cases} 0 & \text{if } |x| > a/2 \\ d & \text{if } |x| \leq a/2 \end{cases},$$

and $a < \Lambda$.

Its Fourier transform is:

$$T(u) = d \frac{\sin(\pi a u)}{\pi u} \left[\sum_h \delta(u - \frac{h}{\Lambda}) * N\Lambda \frac{\sin(\pi N \Lambda u)}{\pi N \Lambda u} \right]. \quad \text{--- 2.33}$$

The diffraction intensity is

$$I(u) = T(u)^2 \propto d^2 \quad \text{--- 2.34}$$

Thus the height of each of the diffraction intensity maxima is proportional to the square of the gate height d , equivalent to the grating amplitude. This also confirms the quadratic relation shown in Equation 2.30.

2.3 Fluorescence

2.3.1 Fluorescence process

Fluorescence is a result of a three-stage spontaneous process that occurs in certain molecules (generally polyaromatics hydrocarbons or heterocycles) called fluorophores or fluorescent dyes. The process responsible for the fluorescence of fluorophores is illustrated by the simple electronic-state diagram (Jablonski diagram⁴²), as shown in Figure 2.8.

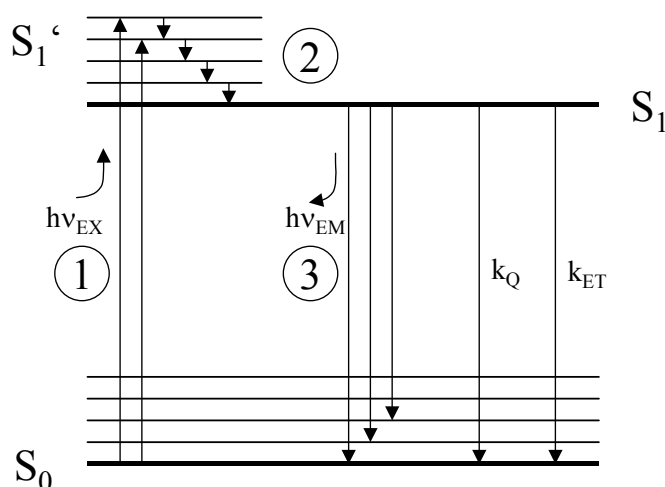


Figure 2.8: Simplified Jablonski diagram. The energies of some electronic (S_0 and S_1) and vibrational states of a molecule are sketched.

Upon the adsorption of a photon of energy $h\nu_{EX}$, the fluorophore is excited from the ground state (S_0) to one of the vibrational levels of a higher singlet state (S_1') (stage ①, cf. Figure 2.8). The excited state only exists for a finite time (usually 1-10 nanoseconds (ns)). During this time, it undergoes changes such as conformational change and interacts with its environment in many different ways (stage ②, cf. Figure 2.8). Consequently, the energy from the excited state (S_1') is partially dissipated, yielding a relaxed singlet excited state (S_1) from which the fluorescent emission occurs. Finally, the reversion to S_0 from S_1 emits a photon of energy $h\nu_{EM}$ (stage ③, cf. Figure 2.8). It is important to note that not all of the excited species return to the ground state via fluorescent emission. Many other processes can occur with their respective rate constants, such as fluorescence resonance energy transfer (FRET, k_{ET}), intersystem crossing (ISC, k_{ISC}), internal conversion (IC, k_{IC}) or collisional quenching (CQ, k_{CQ}), which can depopulate molecules

from S_1 . They all influence the fluorescence quantum yield Φ , which is the ratio of the number of fluorescence photon emitted to the number of photon adsorbed. Since the overall fluorescence probability is governed by the rate constants of the fluorescence process (k_F) and the depopulation processes (k_D), another expression of the quantum yield is:

$$\Phi = \frac{k_F}{k_F + k_D} \quad \text{--- 2.35}$$

where $k_D = k_{ET} + k_{ISC} + k_{IC} + k_{CQ}$. Due to energy loss during the excited state lifetime, $h\nu_{EM}$ is smaller than $h\nu_{EX}$. Therefore, the emitted fluorescence photons have longer wavelength (lower frequency) than the photons responsible for the excitation. This wavelength difference is termed the Stokes shift, which allows the emitted fluorescent photons to be easily distinguished from the excitation photons, leading to the possibility of a very low background in fluorescent studies.

2.3.2 Fluorescence quenching and self-quenching

Quenching refers to any process that causes a reduction in the quantum yield of a given fluorescence process. Quenching can be either collisional or static. The collisional quenching occurs if the quencher comes into contact with the excited fluorophore during the fluorescence lifetime and causes the dye to return to the ground state without emitting a photon, described by the Stern-Volmer Equation:

$$I_o/I = 1 + k_q[Q]\tau \quad \text{--- 2.36}$$

Where I_o is the fluorescence intensity in the absence of quencher, I is the intensity in the presence of the quencher at concentration $[Q]$, k_q is the rate of collisional quenching, and τ is the observed lifetime.

Static quenching is due to the formation of a ground state complex between the fluorescent molecule and the quencher with formation constant K_c , described by:

$$I_o/I = 1 + K_c[Q] \quad \text{--- 2.37}$$

One of the interesting phenomena about fluorescence is that multiple labelling of a molecule with a fluorophore does not always leads to an increase in fluorescent intensity. The brightness of a fluorophore is defined as the product of the extinction coefficient (ϵ) and the quantum yield (Φ):

$$\text{Brightness} = \epsilon \times \Phi \quad \text{--- 2.38}$$

If we conjugate N fluorophores to a molecule, the overall brightness can be described as:

$$\text{Brightness} = \epsilon \times \Phi \times N \quad \text{--- 2.39}$$

In many cases, as N increases, the overall brightness does not increase linearly and sometimes even decreases. This is known as a phenomenon of inter-conjugate “self-quenching” of the conjugated fluorophores.⁴³ Different fluorophores differ in their ability to self-quench. It has been confirmed that the more hydrophobic the fluorophore, the lower the ratio of fluorophores/conjugate to which quenching will occur. Intra-conjugate “self-quenching” is also observed if conjugates are densely packed. Generally, self-quenching is considered as a result of excited-state interactions (collisional quenching), or, of the formation of non-fluorescent complexes (e.g. dimers).

2.3.3 Fluorescence resonance energy transfer

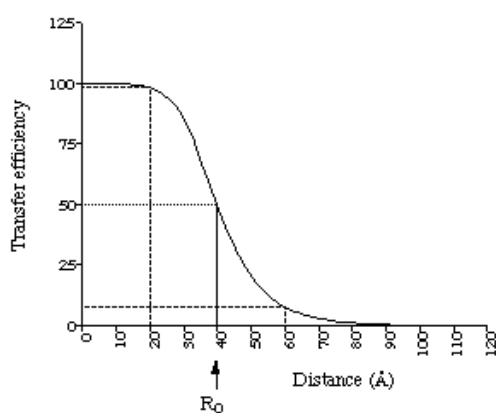


Figure 2.9: Schematic example of energy transfer efficiency dependent on the distance of donor-acceptor. The Förster radius (R_0) is shown.

Resonance energy transfer, often known as fluorescence resonance energy transfer (FRET) or Förster energy transfer, is the transfer of excitation energy from a donor to an acceptor. An important consequence of this transfer is that the emission of light by the donor is greatly reduced. The acceptor may or may not be fluorescent. FRET is a distance-dependent interaction where the energy transfer occurs typically over a distance of 1-10 nm, making it useful over distances comparable with the dimensions of biological macromolecules (e.g. the molecular beacon technology⁴⁴). The efficiency of FRET is a key factor, which is dependent on the inverse sixth power of the intermolecular separation (R) of dipole-to-dipole interaction given by the following equation:

$$\Phi_{ET(R)} = \frac{R^6}{R^6 + R_0^6} \quad \text{--- 2.40}$$

The distance at which energy transfer is 50% efficient (i.e., 50% of excited donors are deactivated by FRET) is defined by the Förster radius (R_0).

2.3.4 Photobleaching

A typical fluorophore can undergo a finite number of excitation-relaxation cycles prior to photochemical destruction. This process is often referred to as photobleaching, photofading or photodestruction. For a photostable fluorophore, e.g. tetramethylrhodamin, photobleaching occurs after about 10⁵ cycles. In contrast, fluorescein photobleaches very easily. Generally speaking, the photobleaching involves the generation of reactive oxygen molecules, thus it is sometimes useful to introduce antioxidants or to use anoxic conditions. On the other hand, the rate of the photobleaching is often proportional to the intensity of illumination. Therefore, a simple practical way to overcome this is to reduce the time or the intensity of the excitation radiation.

2.3.5 Fluorescence at the metal/dielectric interface

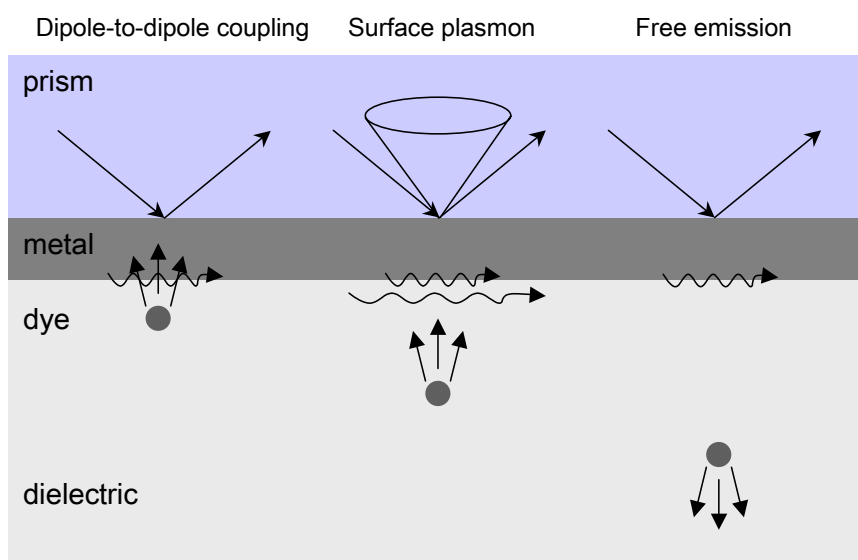


Figure 2.10: Schematic drawing of a fluorophore positioned close to a metal/dielectric interface. Different fluorescence decay channels take place at different fluorophore/metal separation distances.

A fluorophore close to a surface can be excited by the evanescent wave. For that, the fluorophore should be placed within the decay length of the evanescent field for excitation, which is typically several tens to hundreds of nanometers for applicable wavelengths. This makes the detection to be surface sensitive and compatible to modern biosensor geometries. Surface plasmon fluorescence spectroscopy (SPFS)¹⁴ and total internal reflection fluorescence spectroscopy (TIRF)⁴⁵ belong to

this category. TIRF uses a dielectric sensor surface that is illuminated by an evanescent field created by totally internally reflecting a laser beam and has been well developed to be a mature fluorosensor. Femtomolar sensitivity was reported with a channel-etched thin film waveguide fluoroimmunosensor.⁴⁶ TIRF microscope has been even commercialized allowing for the observation of spatially resolved fluorescence images.⁴⁷

Compared with TIRF, there are at least two advantages of using surface plasmon evanescent waves to excite the fluorophores locating at the interface. Firstly, the enhanced evanescent field excited by SPR exhibits greatly enhanced intensity more than the TIR case¹⁴. Secondly, the semi-transparent metal film acts as an efficient blocker to reduce the background contribution from the excitation light source. However, introducing the metal layer alters the way an excited fluorophore loses its energy. As reviewed^{14,48}, there are additional decay channels which are contributing to the decrease of the radiative quantum yield of the emitters (fluorophores) and they take place in different dye-metal separations (summarized in Figure 2.10).

If a dye is positioned at a distance within 10 nm to the metal surface, the non-radiative decay of fluorescence is the dominating process. The excitation is assumed to be dipole-to-dipole, if it is due to the excitation of an electron-hole pair (exciton) in the metal. The standard Förster model gives a R^{-6} dependence of the transfer rate to the separation distance (cf. Figure 2.9), due to the co-effect from both near fields of the donor molecule and the acceptor molecule. However, the distance dependence of energy transfers involving a dye and a surface (could be rough) can be greatly compromised to be $R^{-3} \sim R^{-4}$ dependent due to the integration over the enlarged number of effective acceptor sites. The transferred energy dissipated by the metal is converted into heat.

At an intermediate-distance regime (a few nm up to ~ 20 nm), a significant fraction of excited fluorescence couples back to surface plasmon polaritons, by fulfilling momentum-matching conditions. Unless SPP modes can be converted again into photons by a coupling-prism or a grating, which allows for the monitoring of SPP decay channel⁴⁹, it represents a significant loss of fluorescence yield.

At sufficient separation distances (>20 nm), free emission of the dyes dominates. However, the fluorescence yield cannot be directly obtained unless two effects are considered. Firstly, the fluorescence emission oscillates as the distance increases, since the metal reflects the fluorescence field and introduces light interference. Secondly, the excitation source, i.e., the evanescent field weakens as the distance increases.

2.4 Interfacial biomolecular interaction analysis

2.4.1 Interface kinetics based on Langmuir adsorption model

The development of evanescent wave biosensors offers an easy access to the kinetics of a biomolecule in the solution reversibly interacting with another biomolecule immobilized on the solid surface. The conventional treatment starts with a simple 1:1 interaction model,⁵⁰ equivalent to the Langmuir adsorption isotherm,⁵¹ which is the simplest physically plausible isotherm based on three assumptions:

1. Adsorption cannot proceed beyond monolayer coverage.
2. All sites are equivalent and the surface is uniform.
3. The ability of a molecule to adsorb at a given site is independent of the occupation of neighboring sites.

If these conditions are met the dynamic equilibrium is,



assuming A is the molecule binding from the solution and B is specie immobilized on the surface. The forward and reverse interaction rates are described by adsorption (association) rate constant k_{on} and desorption (dissociation) rate constant k_{off} , respectively. Therefore, the association rate of the complex $[AB]$ is

$$\frac{d[AB]}{dt} = k_{on}[A][B] \quad \text{--- 2.42}$$

and the dissociation rate of complex $[AB]$ is

$$-\frac{d[AB]}{dt} = k_{off}[AB] \quad \text{--- 2.43}$$

Upon the dynamic equilibrium of both processes, the association and dissociation rates are equal

$$k_{on}[A][B] = k_{off}[AB] \quad \text{--- 2.44}$$

Therefore the equilibrium constants can be expressed by the rate constants

$$K_D = \frac{[A][B]}{[AB]} = \frac{k_{off}}{k_{on}} \quad \text{--- 2.45}$$

$$K_A = \frac{[AB]}{[A][B]} = \frac{k_{on}}{k_{off}} \quad \text{--- 2.46}$$

where K_D and K_A are called dissociation constant and affinity constant, respectively. This treatment is mathematically identical as if the interaction occurs in the homogenous phase. However, at the solid-water interface, the transported (diffusion and convection) of A from the bulk solution to the interface must be taken into account.

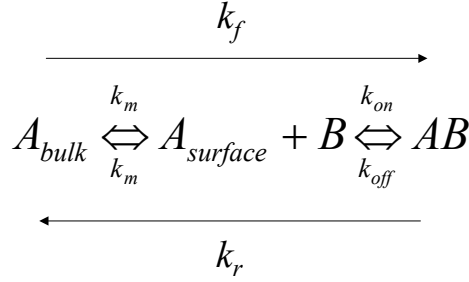


Figure 2.11: A simple model for a biomolecular interaction at the solid/water interface and definition of the parameters that are used to describe kinetic analysis of the interaction.

The formation of the complex AB can be influenced by the mass-transport rate constant k_m from the bulk to the interface and from the interface to the bulk, schematically described in Figure 2.11. The forward and reverse rate constant k_f and k_r are introduced to build the direct link between $[A_{bulk}]$ and $[AB]$. Therefore, the formation of the complex AB is defined as:

$$\frac{d[AB]}{dt} = k_f [A_{bulk}] [B] - k_r [AB] \quad \text{--- 2.47}$$

However, at the surface, the relation is expressed as:

$$\frac{d[AB]}{dt} = k_{on} [A_{surface}] [B] - k_{off} [AB] \quad \text{--- 2.48}$$

Since the $[A_{surface}]$ is balanced by the mass-transport flux and the formation of AB , we get

$$k_m [A_{bulk}] - k_m [A_{surface}] = \frac{d[AB]}{dt} = k_{on} [A_{surface}] [B] - k_{off} [AB] \quad \text{--- 2.49}$$

Therefore,

$$[A_{surface}] = \frac{k_m [A_{bulk}] + k_{off} [AB]}{k_{on} [B] + k_m} \quad \text{--- 2.50}$$

Combining 2.48 to 2.50, and referring to 2.47 yields

$$k_f = \frac{k_{on}k_m}{k_m + k_{on}[B]} = \frac{k_{on}}{1 + \frac{k_{on}[B]}{k_m}} \quad \text{--- 2.51}$$

$$k_r = \frac{k_{off}k_m}{k_m + k_{on}[B]} = \frac{k_{off}}{1 + \frac{k_{on}[B]}{k_m}} \quad \text{--- 2.52}$$

Note that the mass-transport rate k_m equally influences the k_{on} and the k_{off} by a factor of $k_{on}[B]$. This indicates that mass-transport effect dominates at the early stage of association or the later stage of the dissociation, where the concentration of free surface site $[B]$ is high.

2.4.2 Mass-transport controlled kinetics

If k_m is very small, or the surface concentration of B is very large, i.e. $k_m \ll k_{on}[B]$, the interaction is controlled by the mass-transport rate:

$$\frac{d[AB]}{dt} = k_m[A_{bulk}] - \frac{k_m k_{off}}{k_{on}[B]}[AB] \quad \text{--- 2.53}$$

At the initial association stage $[AB]$ is very small, therefore the complex forming rate is solely dependent on the bulk concentration of A , and the binding signal increases linearly with time.

$$\frac{d[AB]}{dt} = k_m[A_{bulk}] \quad \text{--- 2.54}$$

This can be used for the concentration analysis of analyte A , since the slope of the initial stage of the binding curve is proportional to the analyte concentration. Theoretically the linear range of the dose-response curve has no limitation at the lower concentration side. If the reaction rate is fully mass-transport limited, the sensor surface acts like an infinite sink and $[A_{surface}] = 0$. In this case, k_m can for all practical situations be described by: ⁵²

$$k_m = 0.98(D/h)^{2/3}(v/bx)^{1/3} \quad \text{--- 2.55}$$

where D is the diffusion coefficient, h and b are the height and the width of the flow cell, v is the volumetric flow rate, and x is the distance from the flow cell entrance.

2.4.3 Interaction controlled kinetics

If the mass-transport rate is much larger than the association rate constant, or the surface concentration of the immobilized specie is low, i.e., $k_m \gg k_{on}[B]$, then $[A_{surface}] = [A_{bulk}]$. k_f and k_r are approximately equal to the intrinsic rate constants k_{on} and k_{off} . Under such a condition, the binding rate can be expressed as:

$$\frac{d[AB]}{dt} = k_{on}[A][B] - k_{off}[AB] \quad \text{--- 2.56}$$

Since the surface concentration of the free binding site $[B]$ is the difference between the concentration of complex at saturation and the current complex concentration:

$$[B] = [AB_{max}] - [AB] \quad \text{--- 2.57}$$

Combining 2.56 and 2.57, and considering that the response R scales linearly with the complex concentration $[AB]$, one gets:

$$\frac{dR}{dt} = k_{on}C(R_{max} - R) - k_{off}R \quad \text{--- 2.58}$$

where C is the concentration of the analyte, R_{max} is the saturation signal at sufficiently high analyte concentration. The solution of 2.58 yields:

$$R = \frac{k_{on}CR_{max}}{k_{on}C + k_{off}}(1 - e^{-(k_{on}C + k_{off})t}) = R_o(1 - e^{-(k_{on}C + k_{off})t}) \quad \text{--- 2.59}$$

At dissociation phase, $C = 0$, thus:

$$\frac{dR}{dt} = -k_{off}R \quad \text{--- 2.60}$$

The solution becomes

$$R = R_o e^{-k_{off}t} \quad \text{--- 2.61}$$

Equation 2.59 and 2.61 can be used to yield k_{on} and k_{off} from a single set of association/dissociation data using non-linear curve fit. The k_{off} is obtained first by analyzing the dissociation phase.

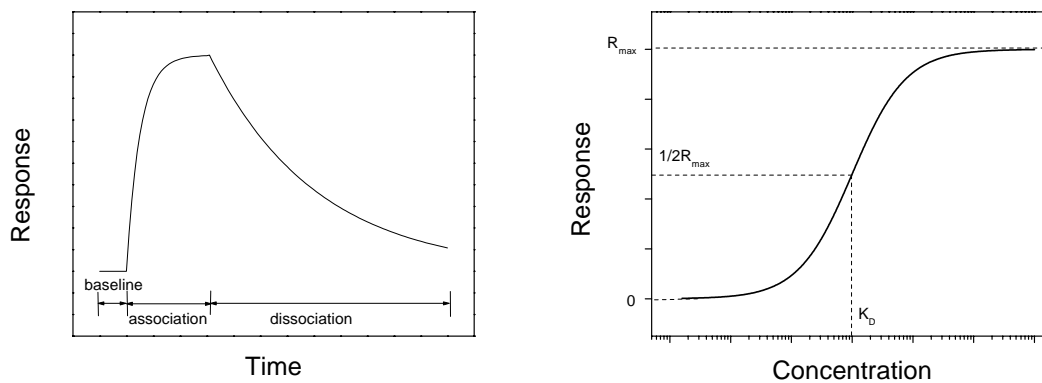


Figure 2.12: Schematic examples of: (left panel) a typical interaction analysis involving an association and a dissociation process, (right panel) an equilibrium analysis based on a 1:1 Langmuir model. Both methods help to determine the intrinsic affinity constant of the interaction couple.

2.4.4 Equilibrium analysis

Upon dynamic equilibrium, the net effect of the association and dissociation process is zero, i.e.,

$$\frac{dR}{dt} = k_{on}C(R_{max} - R_{eq}) - k_{off}R_{eq} = 0 \quad \text{--- 2.62}$$

where R_{eq} is the equilibrium response at a given analyte concentration C . Therefore, the equilibrium signal reflects the affinity constant K_A and dissociation constant K_D of the interaction couple.

$$\frac{k_{on}}{k_{off}} = K_A = \frac{1}{K_D} = \frac{R_{eq}}{C(R_{max} - R_{eq})} \quad \text{--- 2.63}$$

This can be converted to a format which resembles the 1:1 Langmuir isotherm:⁵¹

$$R_{eq} = \frac{CK_A R_{max}}{CK_A + 1} = \frac{CR_{max}}{C + K_D} \quad \text{--- 2.64}$$

The isotherm is an S shaped curve if using logarithmic axis for the concentration, as shown in Figure 2.12. Upon application of an analyte concentration of $C = K_D$, R_{eq} is half of the saturation response R_{max} . The time to reach equilibrium can be calculated by the following equation deduced from 2.59:

$$t = \frac{-\ln(1 - R/R_{eq})}{k_{on}C + k_{off}} \quad \text{--- 2.65}$$

For instance, at $C=K_D$, it takes $\sim 1/k_{off}$ period of time to reach 90% association equilibrium.

2.4.5 Applicability of the kinetic model

While this pseudo-first order kinetic model has been used very successfully in studies with more qualitative questions (such as demonstration of interactions between biomolecules), the determination of the kinetic rate constants of binding is often complicated by the fact that most binding curves deviate from the single exponential time-course expected for a simple pseudo-first order reaction. Apart from the experimental causes (e.g. the sample depletion, noise, drift, impurity, etc.), major concerns for the deviation are focused on:

1. mass transport effects/rebinding;
2. multivalent interactions/avidity effects;
3. heterogeneity in the immobilized ligands / matrix effects;
4. complex binding mechanisms.

Fortunately, by improving the experimental design (e.g use high flow rates and low surface capacities) and applying advanced analysis algorithm (e.g the Global Analysis,⁵³ fitting association and dissociation phase data for a series of concentrations simultaneously), the contribution from most of these effects can be minimized or even corrected.⁵⁴

3 Experimental

3.1 Instrumental

A major part of this study was based on a surface plasmon resonance set-up in the Kretschmann-Reather configuration, which is also commercially the most implemented configuration.⁶ Almost all of the components of this set-up are modular, which directly enables the convenient instrumental upgrade, e.g., combining the electrochemical probing/manipulating,⁵⁵ or fluorescence detection¹⁴ abilities.

The schematic of the set-up is depicted in Figure 3.1. The beam of a Helium-Neon (HeNe) laser (Uniphase, 5 mW, $\lambda = 632.8$ nm) passes through a chopper (frequency = 1331 Hz) that is connected to a lock-in amplifier (EG&G). The modulated beam then passes through two polarizers (Glan-Thompson), by which the intensity and the plane of polarization of the laser can be adjusted. A programmable shutter is installed such as to constantly block the laser (unless data points are recorded), thus minimizing the photo-bleaching effect of the fluorescent dyes. Next, the beam is reflected off the base of the coupling prism (Schott, LASFN9, $n=1.85$ @ 633 nm) and is focused by a lens ($f = 50$ mm, Owis) onto a collection lens and a photo-diode detector, connected to the lock-in amplifier. The prism/sample and the photo-detector are mounted on two co-axial goniometers respectively, enabling an independent tuning of respective angular positions.

Surface plasmon microscopy (SPM) can also be realized for monitoring laterally structured surfaces,¹⁸ or for parallel read-out of arrayed samples.^{19(A)} Two modifications in the set-up are necessary:

- 1) Use a beam expander by an 10× objective lens, an 25 μm pinhole and a collimating lens to get clean, parallel and expanded beam for illuminating a larger surface area,
- 2) Replace the photo-diode detector to be a monochromatic CCD camera (Hamamatsu, C5405-01) equipped with an imaging lens (EHD, Zoom70 or Rodenstock $f=50$ mm). The CCD camera is connected to a frame-grabber card for image transmitting.

The fluorescence detection unit is mounted towards the base of the prism, rotating together with the prism (sample) at θ , while the photo-diode detecting the reflected light rotates at 2θ . The fluorescence emission from the sample surface is collected by a lens ($f = 50$ mm, Owis) and passes through an interference filter ($\lambda = 670$ nm, $\Delta\lambda = 10$ nm, LOT, 80% transmittance) into a photomultiplier tube (PMT, Hamamatsu), which is connected to a photon-counter (Agilent) unit via a home-built electronic interface. Note that the interference filter is specifically designed for commercially versatile fluorophores such as Cy5 (Cyanine 5, from Amersham Pharmacia Inc.) and Alexa Fluor 647 (from Molecular Probes Inc.). Occasionally, a neutral filter (attenuator) is used to attenuate the fluorescence in the case of strong fluorescence intensity, in order to keep the PMT working in the linear input-versus-output range ($<1\sim 2$ million counts per second). Custom programs accomplish the data acquisition and the controlling of the system electronics.

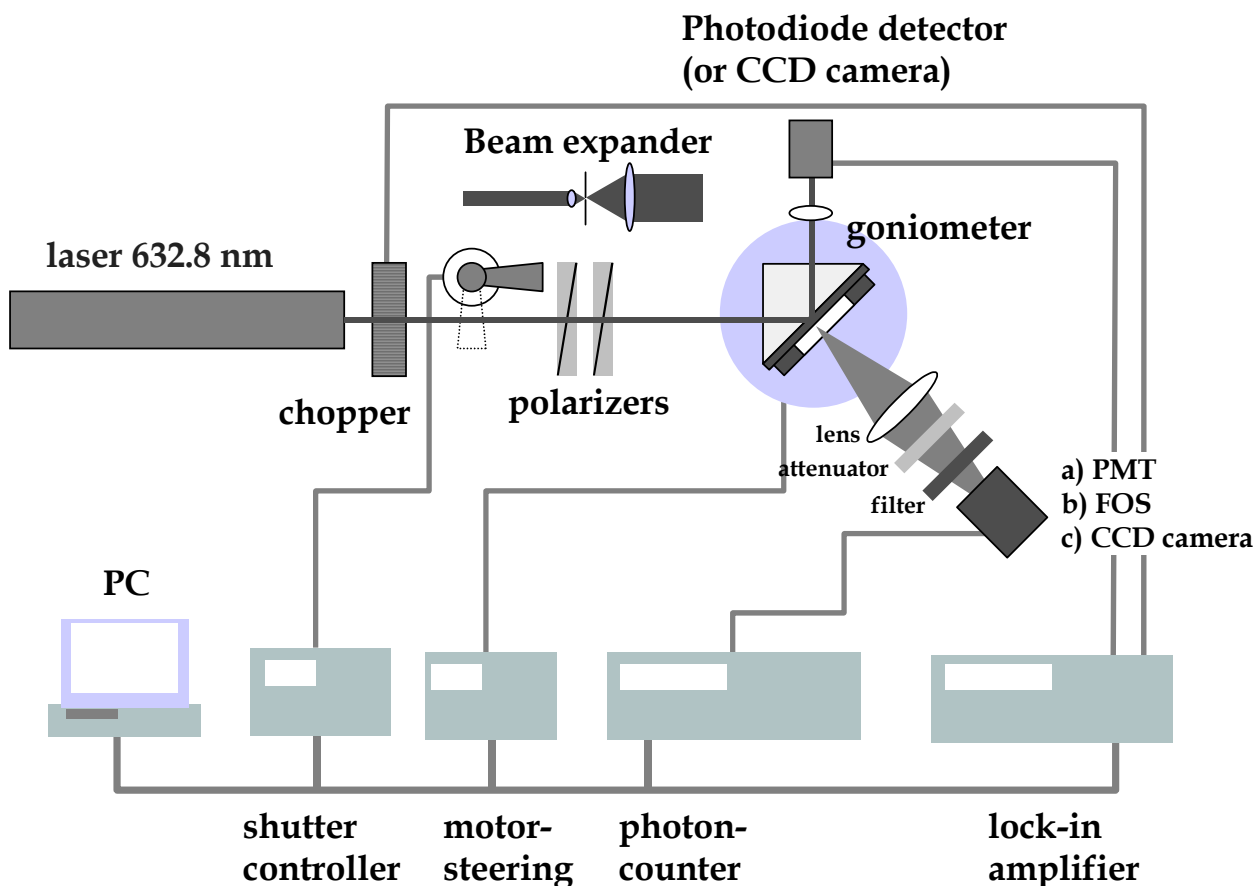


Figure 3.1: Schematic sketch of a surface plasmon spectrometer set-up including various extensions.

In order to get spectroscopic information from the fluorescence emission, a fiber optic spectrometer (from Ocean Optics Inc., model USB-S2000, abbreviated as FOS) equipped with a dedicated collection lens is employed instead of the PMT unit. Surface plasmon fluorescence microscopy (SPFM) is also instrumentally feasible by equipping a cooled CCD camera (Roper scientific) with an imaging lens (Rodenstock $f = 50$ mm). Yet, for these two elements, the controlling and the data acquisition are through the programs provided by the companies. Therefore, their signals are only manually synchronized with the SPR reflectivity signal.

Two measurement modes, i.e., angular scanning mode (reflectivity/fluorescence/image as a function of angular position) and time-resolved kinetic mode (reflectivity/fluorescence/image as a function of time) are both applicable for SPR (M) and SPFS (M) measurements.

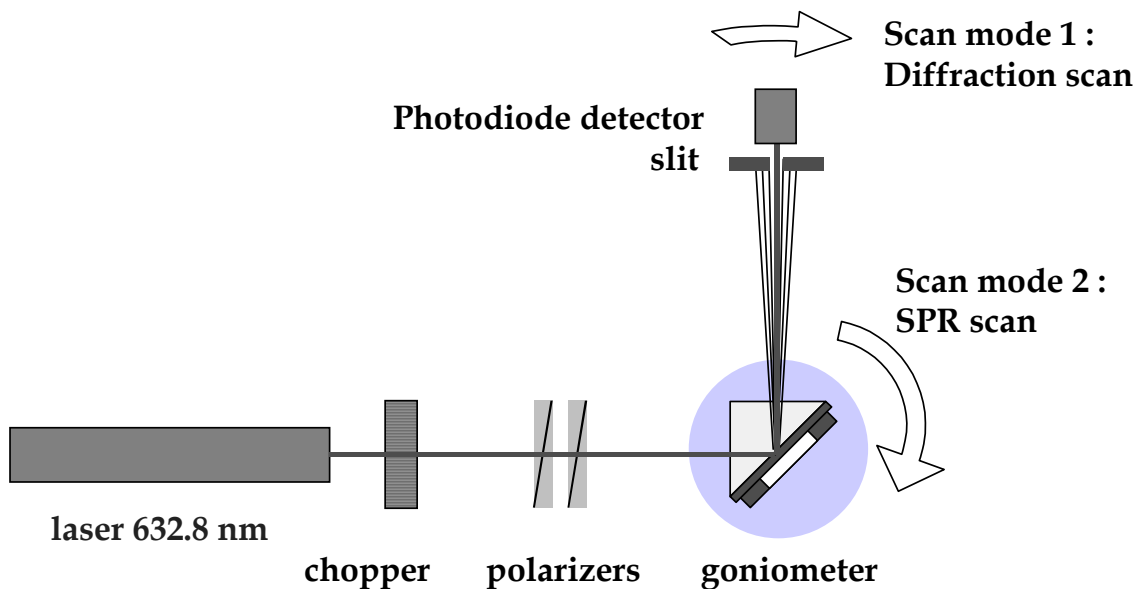


Figure 3.2: Sketch of a surface plasmon diffraction set-up. The diffraction and SPR scan modes are depicted as mode 1 and mode 2, respectively.

The set-up used for the diffraction experiments is based on the same Kretschmann SPR set-up (cf. Figure 3.2). The same linearly polarized HeNe laser ($\lambda=633$ nm, 5 mV) is used for the excitation of PSP. The laser intensity is also modulated by the chopper and the reflected/diffracted intensity is also measured by a photo-diode detector coupled to a lock-in amplifier. The angular acceptance of the photo-diode detector is limited by a 1 mm slit mask to $\Delta\tau\approx 0.08^\circ$ for resolving the diffraction orders. The two co-axial goniometers enable an independent tuning of the incident

angle of the laser and/or the detection angle. Both motors rotate in a $\theta/2\theta$ fashion for the usual SPR angular scans, whereas only the detector motor rotates when performing diffraction scans.

3.2 Flow cell and liquid handling

A few commercial instruments listed in Table 3.1 are equipped with well-designed flow cells and liquid handling systems. These fluidic systems are advantageous in:

- 1) accelerating mass-transport limited interaction kinetics, in the case of low analyte concentration;
- 2) minimizing sample consumption;
- 3) enabling automatic sample mixing, delivery, etc.

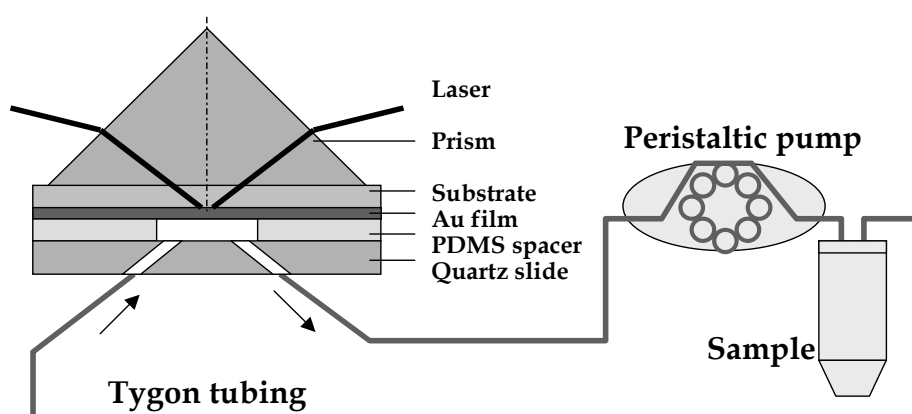


Figure 3.3: Sketch of a homemade flow cell with a thin PDMS spacer (300 μm) and a sealed circulation loop.

The schematic of the flow cell designed for our sensing system is shown in Figure 3.3. It consists of a thin polydimethylsiloxane (PDMS) spacer (300 μm , with a 5mm*7mm ellipse hole) and a quartz cover slide (Herasil glass) through which two holes are machined and two steel needles are glued, serving as inlet and outlet, respectively. The flow cell is attached, via Tygon® tubing with an inner diameter of 0.76 mm, to a peristaltic pump (Ismatec, Switzerland) and the sample tube, forming a closed circulation loop. Buffer and sample solutions can only be manually exchanged, however, with little trouble from air bubbles. Once the exchange is completed, the whole loop is closed and completely sealed allowing for a long interaction time (>48 hours). The loop volume is around 300 μL , with a minimum sample consumption of around 400~600 μL to assure the desired analyte working concentration. The highest linear flow rate of 100 mm/sec (at 9 mL/min) at the

sensing point compares favorably with that of Biacore's microfluidic system,⁵⁶ which is the most sophisticated/advanced fluidic system in the market.

	SPFS	Biacore	IAsys
Transducer principle	SPR+fluorescence	SPR	Resonant mirror
Liquid handling system	Flow cell	Flow cell	Cuvette system
Sample loading	Manual control	Automatic control	Automatic control
Liquid cell dimension	8.7 μ L- 14.7 μ L	25 nL	>100 μ L
Typical flow rate	3 mL/min	20 μ L/min	Vibro stirrer
Typical sample flux	2 mL/mm ² *min	0.8 mL/mm ² *min	Not applicable
Sample consumption	> 350-500 μ L Circulate	20-100 μ L Flow-through	30-100 μ L Incubate
Parallel Channels	One	Two or four	Two

Table 3.1: A list of the flow cell of SPFS and a few commercial instruments equipped with well-engineered flow cells and liquid handling systems.

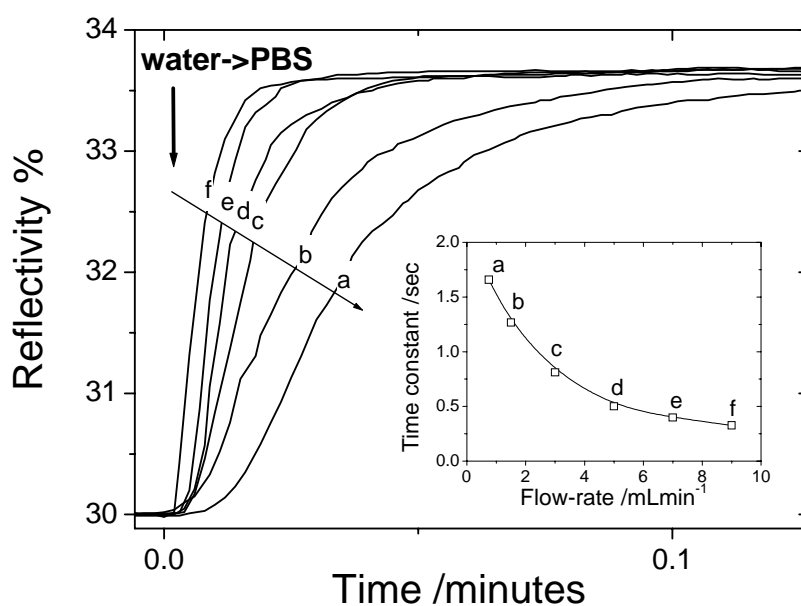


Figure 3.4: The SPR time responses of the homemade flow cell upon sample exchanges (MilliQ water -> PBS). The flow rates are 0.75, 1.5, 3, 5, 7, 9 mL/min for (a), (b), (c), (d), (e), (f), respectively. The inset shows their corresponding time constants, yielded by single exponential fits.

The time response of the flow cell upon the sample exchange was tested (shown in Figure 3.4). Two liquids, MilliQ water and PBS buffer, were used as liquids with different refractive indices. The flow cell was firstly filled with MilliQ water, followed by the exchange by PBS buffer at

flow rates of 0.75, 1.5, 3, 5, 7, 9 mL/min respectively. Positive signal increases were monitored, because the increase of bulk refractive index induced a positive shift of the SPR spectrum. Single-exponential fits to the signal-increasing phases yielded the time-constants of the sample exchange of 1.7, 1.3, 0.8, 0.5, 0.4, and 0.3 seconds, respectively. If the limiting measurable kinetic constant (k_L) is defined as 3 times that of the sample exchange, k_L , for this fluidic system one obtains $\sim 10^0$ s⁻¹ at a flow rate of 9 mL/min, which is about one order-of-magnitude higher than Biacore's fluidic system.⁵⁷ This fast sample exchange ability offers a potential to measure extremely fast biomolecular interactions, e.g., the interaction between human cell-adhesion molecule CD2 and CD58 (LFA-3) with a very low affinity ($K_D = 9\sim 22$ μ M) and dissociated with an extremely fast dissociation rate constant ($k_{off} = 4$ s⁻¹).⁵⁸ Typically, a flow rate of 3 mL/min was used for all the interaction studies unless otherwise mentioned.

3.3 Protein labeling

Only a few fluorescently labeled secondary antibodies and 'normal' proteins are commercially available. However, the available dye-labeling kits enable a convenient mean to label small quantities (e.g. 100 μ g) of proteins of interest with Mw > 30 kDa. Basically, three steps are required in the labeling procedure:

- 1) Reaction with dyes carrying reactive group, usually a succinimidyl ester (amine-reactive) or maleimide (thiol-reactive).
- 2) Purification of the labeled protein, usually by a gel-filtration column or dialysis.
- 3) Determination of the degree of labeling by UV adsorbances of proteins and dyes, respectively.

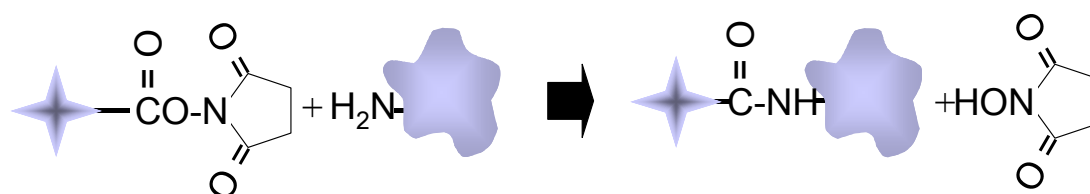


Figure 3.5: Schematic of the labeling of protein with Alexa Fluor 647 dye with a succinimidyl ester moiety.

For our experimental conditions (e.g. using the wavelength @ 633 nm as the excitation source), the commercial Alexa Fluor 647 dye (abbreviated as AF 647, from Molecular Probes, Inc.) was used taking advantage of its high fluorescence yield, less auto-quenching and in-sensitivity to pH

conditions.⁵⁹ The commercial labeling kit contains things needed to perform labeling reactions as well as to purify the resulting conjugates. In the kit, the AF 647 dye contains a succinimidyl ester moiety that reacts efficiently with primary amines of the protein to form stable dye-protein conjugates at pH 7.5-8.5. The experimental protocol for labeling 100 μg monoclonal antibody is as the following:

- 1) Prepare 1 mg/mL antibody solution with sodium bicarbonate buffer (100 mM, pH 8.3)
- 2) Transfer 100 μL of the antibody solution to the vial of reactive dye. Incubate the solution for 1 hour at room temperature. Every 10-15 minutes, gently agitate the vial.
- 3) Prepare the spin column by adding the resin (30 kDa size exclusion) suspension into the column and allow it to settle, until the bed volume reaches 1.5 mL.
- 4) Centrifuge the column for 3 minutes at $1100 \times g$ using a swinging bucket rotor. The Equation 3.1 converts the revolutions per minute (rpm) into the relative centrifugal force (g-force).
- 5) Load the 100 μL reaction volume dropwise onto the center of the column, allowing the solution to adsorb into the gel bed.
- 6) Place the column into a collection tube and centrifuge for 5 minutes at $1100 \times g$. The collection tube then contains labeled protein in ca. 100-150 μL of PBS, pH 7.2, with 2 mM sodium azide.
- 7) Dilute a small amount of the purified conjugate into suitable buffer and measure the absorbance in a cuvette with a 1 cm pathlength at both 280 nm (A_{280}) and 650 nm (A_{650}).

$$\text{Relative centrifugal force} = (1.12 \times 10^{-5}) (\text{rpm})^2 (\text{radius}) \quad \text{--- 3.1}$$

$$\text{The protein concentration (M)} = \frac{(A_{280} - (A_{650} \times 0.03)) \times \text{dilution_factor}}{203,000} \quad \text{--- 3.2}$$

with 203,000 being the molar extinction coefficient (ϵ) in $\text{cm}^{-1}\text{M}^{-1}$ of a typical IgG at 280 nm and 0.03 is a correction factor for the contribution of the fluorophore to the absorbance at 280 nm.

The degree of labeling, i.e., dye-to-protein ratio (abbreviated as D/P ratio) is:

$$\text{Mole dye per mole protein} = \frac{A_{650} \times \text{dilution_factor}}{239,000 \times \text{protein_concentration}(M)} \quad \text{--- 3.3}$$

3.4 Surface functionalization techniques

3.4.1 Self-assembled monolayers

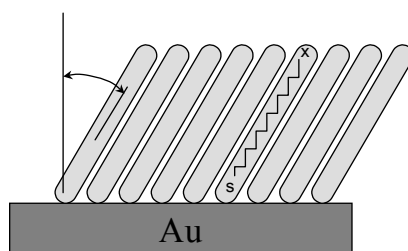
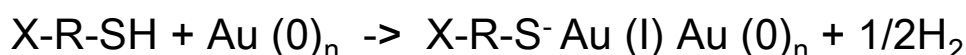


Figure 3.6: Schematic representation of a highly ordered monolayer of alkanethiolate formed on a gold surface.

Molecular self-assembly phenomena are widely seen in surface modification strategies. Self-assembled monolayers (SAMs) are highly ordered molecular assemblies of long chain alkanes that chemisorb on the surface of solid materials. The structure of SAMs, effectively two-dimensional crystals with controllable chemical functionality, makes them ideal model systems for the investigations and applications in wetting, adhesion, corrosion, protein adsorption, surface functionalization, micro-/nano- fabrications, etc. SAMs of alkanethiolates on gold (RSH/Au) are one of the most attractive systems for their: (i) ease of fabrication; (ii) degree of perfection; (iii) chemical stability; (iv) availability of materials; and (v) flexibility in chemistry and thus surface functionality. SAMs of alkanethiolates on Au (111) form quasi-crystalline structures $((\sqrt{3} \times \sqrt{3})R30^\circ)$ for $n > 6$ with the driving forces coming from lateral van der Waals forces and the strength of the sulphur-gold bond (cf. Figure 3.6).⁶⁰

Formation of mixed (binary) SAM is a strategy to build sensor surfaces as it has been reported extensively.⁶¹ This strategy helps to build up structurally well-defined functional monolayers and enables convenient tuning of functional group density. Practically, two kinds of thiols, one with

passive end group and the other one with a functional end group, are mixed together before being chemisorbed onto the gold surfaces. There is a great flexibility in choosing the end groups of thiols. The functional thiol usually carries a small ligand or a reactive group. The end group of the non-functional thiol, however, needs to be chemically inert and should strongly repel the analytes, thus minimizing nonspecific adsorption. The relative proportion of the two thiolates in the assembled SAM depends upon several parameters, like the mixing ratio in solution, the alkane chain lengths, the solubilities of the thiols in the solvent used, and the properties of the chain-terminating groups. In general, the composition will not be the same in the SAM as in the preparation solution.⁶² However, approximations are usually valid and acceptable.^{61(A)}

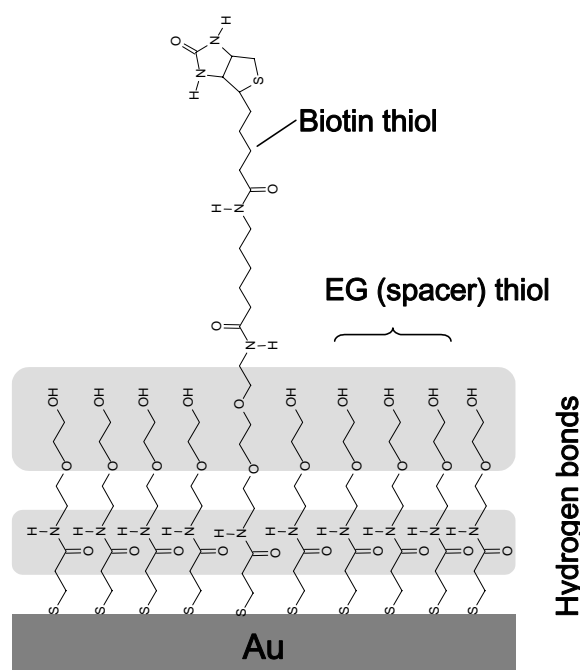


Figure 3.7: Schematic representation drawing of a mixed monolayer of biotin- and EG (spacer)-thiol (with a molar ratio of 1:9 in the preparation solution). The intra-monolayer hydrogen bonds are indicated to stabilize the layer structure.

In this study, a thiol couple, i.e., a biotin-terminated thiol and an ethylene glycol- (EG) terminated thiol (or spacer thiol) is mainly utilized as a functional/non-functional thiol couple for the fabrication of mixed SAMs. Their chemical structures are shown in Figure 3.7. As can be clearly seen, they are alkanethiol-derivatives. The resulting SAM may not be as highly ordered as alkanethiol SAMs. However, the richly available hydrogen bonds can interlink the thiolates and enhance the film stability,⁶³ as is schematically drawn in Figure 3.7.

SAMs were prepared by simply dipping the Au substrates into the thiol solution. In order to minimize the incorporation of water into the SAM structure and thus reduction of the layer

stability, ethanol was normally used as the solvent for thiols in this study. Experimentally, the LASFN9 slides (Schott, $n = 1.85$ @ $\lambda=633\text{nm}$) are carefully cleaned by detergent/water/ethanol and coated with 45-50 nm of gold by thermal evaporation at a deposition rate of 0.1 nm/s under ultra-high vacuum (UHV) conditions ($5\text{E-}6$ mbar) in a commercial evaporator (Edwards). Mixed thiol solutions are prepared at various molar ratios χ , however, at a net thiol concentration of 500 μM in absolute ethanol (99%). Freshly coated Au substrates are immersed in the thiol solutions, then sealed and kept overnight at room temperature. Subsequently, the substrates are removed, rinsed thoroughly with ethanol and blown dry by a stream of nitrogen. The prepared substrates were stored under Argon atmosphere until use. The mole fractions of the biotinylated thiolate, χ , in the SAMs are approximated to its mole fractions in the preparation solutions.

3.4.2 Micro-contact printing (μCP)

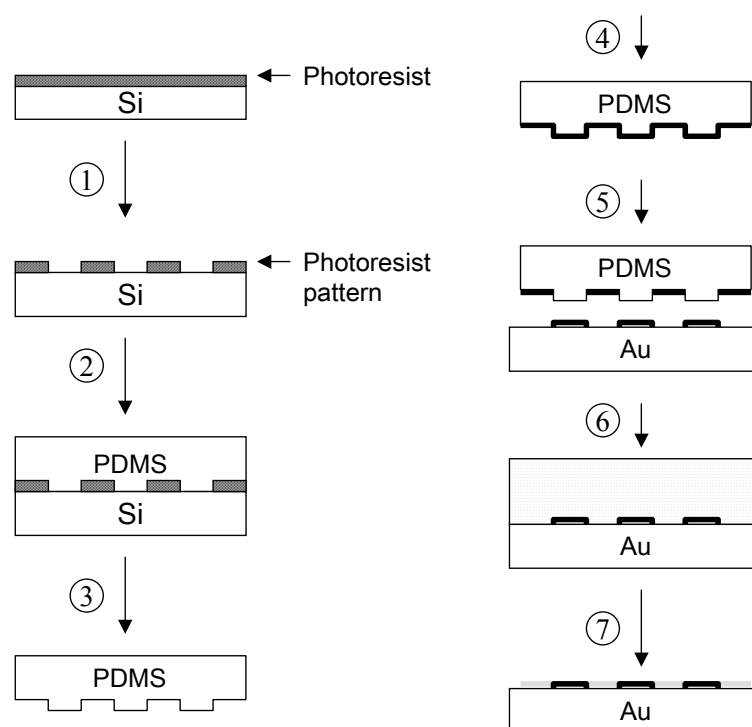


Figure 3.8: ①photolithography is used to create a master, ②PDMS is poured over master and cured, ③ PDMS stamp is peeled away from the master, ④PDMS stamp is exposed to functional thiol solution, ⑤ Stamping onto gold substrate transfers thiol to form functional SAM patches, ⑥Backfilling the substrate with non-functional thiol solution, ⑦uncovered areas are passivated by non-functional SAM.

More and more applications of SAMs in micro- and nanofabrication require the combination with the patterning techniques, includes micro-contact printing (μCP), micromachining, photolithography, photochemical patterning, photo-oxidation, ion-beam writing, electron-beam

writing, surface probe microscopy (SPM) writing, etc. Among all these methods, μ CP is one of the most convenient and versatile methods.⁶⁴ Even enabling patterning nano-features, it is also becoming more compatible with the fashionable nanotechnology.

Figure 3.8 shows a schematic of the μ CP process used in this study. Photolithography through a commercial mask produces the negative pattern profile (as a master) on a spin-casted photoresist layer. An elastometric stamp, i.e., a three-dimensional relief is then formed by casting PDMS (Dow-Corning Corporation, Sylgard 184) on the photoresist master. In this study, two stripe-like PDMS stamps were fabricated, with the width of the embossed strips being $\alpha = 6, 42 \mu\text{m}$ respectively while sharing a common periodicity of $\Lambda=100 \mu\text{m}$ (cf. Figure 3.9).

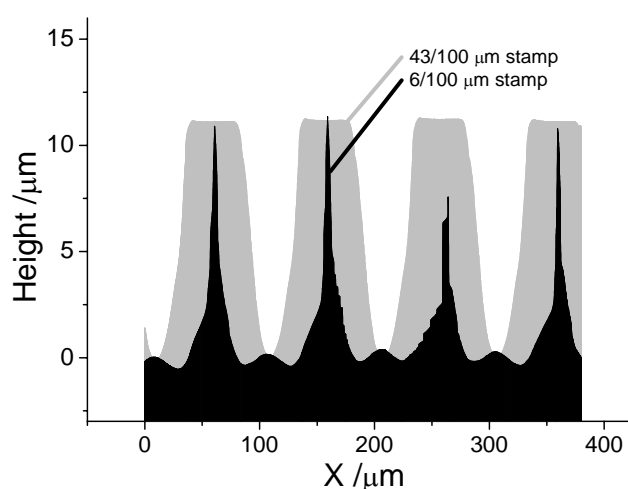


Figure 3.9: Cross-sectional analysis of PDMS stamps by a surface profiler (Tencor, P-10). The scan rate was $20 \mu\text{m}/\text{sec}$ with a force of 2 mg for both scans.

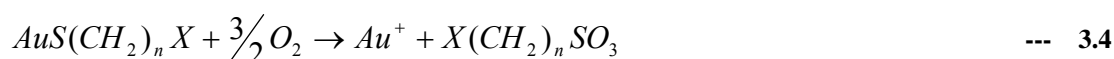
The following μ CP steps are applied to generate functional strips exposing biotin functionality on the Au surfaces.

- 1) Before printing, the stamp was cleaned by O_2/Ar plasma treatment for 15-30 minutes, and sonicated in pure ethanol for 15 minutes.
- 2) The stamp was inked for 5 minutes in an ethanolic solution of a mixture of biotin thiol and spacer thiol (molar ratio 1:9) with a net concentration of $500 \mu\text{M}$. Excess thiol solution was removed and the stamp was dried in a stream of nitrogen.
- 3) The stamp was brought into contact with the freshly evaporated Au (50 nm) on LASFN9 substrate for ~ 1 minute.

- 4) After rinsing with copious amounts of ethanol, the Au substrate was exposed to an ethanolic solution of the pure spacer thiol (2 mM) for ~10 minutes in order to passivate the non-derivatized areas.
- 5) The patterning process was completed by rinsing the slide with ethanol and drying it with nitrogen.

3.4.3 UV-photo-patterning

Thin polymer layer can be patterned through photo-oxidation,⁶⁵ which is ironically a deleterious phenomenon for organic coatings in our daily life. Photo-oxidation technology can also be utilized in patterning SAMs by converting the thiolate headgroup to a sulfonate (cf. Eqn 3.4).⁶⁶



In this study, UV-oxidation was used as another experimentally convenient strategy to generate micro-patterns on surfaces originally covered by homogenous layers, e.g., dextran or polystyrene layers. The dextran covered substrates were commercial CM5 chips from Biacore. The polystyrene covered substrates were prepared by a spin-coating method.

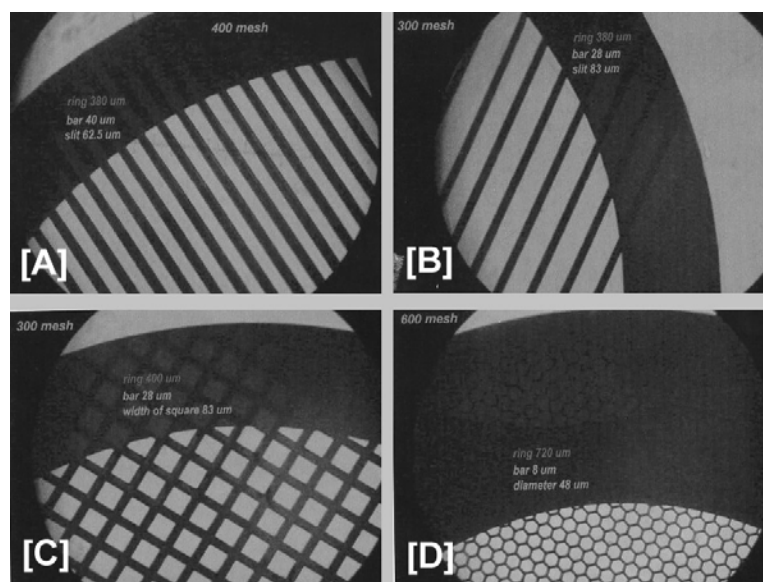


Figure 3.10: Optical microscopic images of the copper grids used in this study. The dimensional parameters are: [A] 400 mesh, outer ring width 380 μm, bar width 40 μm, slit width 62.5 μm, [B] 300 mesh, outer ring width 380 μm, bar width 28 μm, slit width 83 μm, [C] 300 mesh, outer ring width 400 μm, bar width 28 μm, square width 83 μm, [D] 600 mesh, outer ring width 720 μm, bar width 8 μm, hexagonal width 48 μm.

The polystyrene (cut from 96 micro-well board, Nunc Inc.) was dissolved in toluene, with a concentration of 2.5 mg/mL. After the substrate was placed onto the spin coater its surface was completely covered with the solution followed by spinning the sample at a speed of ~2500-3000 rpm. After 1 minute, the substrate was removed from the apparatus and kept in a desiccator at room temperature for >24 hours prior to use.

The UV source used in the study was a low pressure, cold cathode, mercury pen lamp (UVP Inc., model 90-D012-01) that was held 0.5 cm above the sample. The primary output of this lamp occurs at 254 nm with a total power of ~ 5 mW at 1 cm. Copper electron microscopy grids (cf. Figure 3.10) were placed directly on the sample. The sample was then UV-irradiated through the grids for 30-60 minutes. Following the irradiation, the dextran sample was rinsed liberally with MilliQ water, and exposed to an ethanolic solution of the pure spacer thiol (2 mM) for 10 minutes, and rinsed by ethanol, dried by nitrogen stream. The polystyrene surface is ready to be measured without any additional treatment.

4 SPR/SPFS studies on planar surfaces

4.1 Motivations

Surface plasmon field-enhanced fluorescence spectroscopy (SPFS) uses the greatly enhanced electromagnetic field of a surface plasmon mode for the excitation of surface confined fluorophores. At the commonly used gold/water interface, the evanescent field of a surface plasmon is enhanced by a factor of 16 compared to the incident field at the respective resonance angle, and then decays exponentially into the dielectric medium, with a penetration depth of approx. $L_z = 250$ nm. In this thin layer, the accumulation of the analyte molecules alters the optical properties of the interface and can be sensed by an angular shift in the SPR resonance minimum. If the analyte molecule carries a fluorescent dye, fluorescence emission will be excited by the SPR field. In this sense, SPFS can be considered as a combined tool, which simultaneously conveys the information of local refractive index change and the fluorophore concentration. By this, it offers a potential for a more detailed surface investigation than SPR. For example, a recent report elucidated this applications of SPFS in monitoring/distinguish multi-component protein adsorption based on its dual signal sensing ability.⁶⁷ However, lacking the awareness of the non-linear correlation between SPR and fluorescence signal on the metal, the interfacial understanding in that report was limited.

As has been discussed theoretically in chapter 2, the fluorescence yield of fluorophores near a metal exhibits a highly pronounced distance-dependent behavior. Briefly, within a short separation distance range (approx. 20-30 nm), the fluorescence of the fluorophores can be ‘quenched’ by a reduced fluorescent lifetime or, can be ‘back-coupled’ as red-shifted re-radiation. Both effects reduce the effective fluorescence emission. Beyond this range, as the distance increases further, the fluorescence yield weakens with the fading of the evanescent field. On one hand, this strong distance behavior of fluorescence causes problems in the quantification of surface analyte, whose fluorescence yield may depend on its unpredictable position/conformation at the surface. On the other hand, it results in a much more pronounced distance information than

the surface plasmon evanescent field ($L_z = \sim 150$ nm), which may offer a clearer understanding of the three-dimensional distribution of the bound molecules.

Obviously, a planar functional surface (or two-dimensional surface) is experimentally desirable for pronouncing such a distance effect. Combining the 2D surface with the layer-by-layer assembly technique, a distance profile of fluorescence yield on SPFS has been depicted.⁶⁸ In this study, gold surfaces were functionalized by (mixed) SAMs exposing a functional group (e.g. a biotin) with controlled density. Specific recognition interaction, e.g., antibody-antigen interaction occurs if the sample solution passes over the surface driven by the fluidic system. Based on the 2D surface system, important features towards the understanding of SPFS in protein studies will be sequentially addressed in the following.

4.2 Materials

Functional SAM exposing biotin functionalities were prepared following the protocols described in the experimental part. The ratio or density of biotin groups at the surface was controlled by the ratio of biotin thiol, χ , in the preparation solution.

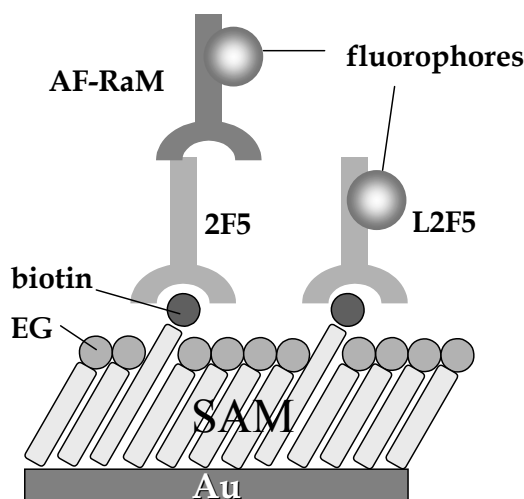


Figure 4.1: Schematic drawing of the interfacial molecular architectures for direct and indirect fluorescence detection schemes for most of the work in this chapter.

The anti-biotin mouse monoclonal antibody 2F5 (isotype IgG *I.k*), the Alexa Fluor 647 labeled (AF 647) rabbit anti-mouse IgG (abbreviated as AF-RaM, reacts with the IgG heavy chains and all classes of Ig light chains from mouse, $D/P=4.8$), the AF 647 labeled streptavidin (abbreviated as AF-SA, $D/P=4.2$), the AF 647 monoclonal antibody labeling kit and the biotinylated goat anti-

mouse IgG (labeling ratio: 5.3) were purchased from Molecular Probes. Cy5 labeled goat anti-mouse IgG (abbreviated as Cy5-GaM, $D/P=4.9$) was obtained from Amersham Pharmacia Biotech. Proteins were stocked at micro-molar concentrations to avoid concentration depletion. Sodium dodecyl sulfate (SDS) and PBS (phosphate buffered saline) tablets were purchased from Sigma-Aldrich. HBS-EP buffer (degassed 10 mM HEPES buffered saline, pH 7.4, 150 mM NaCl, 3 mM EDTA, 0.005% (v/v) surfactant P-20 (equivalent to Tween-20)) was kindly provided by Biacore (Uppsala, Sweden). All protein solutions were prepared in HBS buffer unless otherwise stated.

The 2F5 antibody was labeled with AF 647 dye by following a standard protocol provided by Molecular Probes (cf. chapter 3). The D/P was 4.4, determined spectrophotometrically by measuring the adsorbance at 647 nm (AF 647) and 278 nm (antibody) in PBS buffer. This ratio is within the optimal region for the AF dyes.⁵⁹ The labeled 2F5 is abbreviated as L2F5.

Basically, two interaction modes were applied on the biotin SAM surfaces, namely a direct probing and indirect probing mode, schematically drawn in Figure 4.1. For the direct probing mode, L2F5 captures surface biotin groups. The indirect mode applied firstly 2F5 to decorate the surface biotin, then AF-RaM to yield the fluorescence signal. Both ways are strategies to yield final signal in clinical immunoassays, e.g., the enzyme immunoassay (EIA).

Cy5 labeled human interleukin 8 (Cy5-hIL8, with $D/P \approx 1$) and its biotinylated Fab fragments (named as Fab13A and Fab6x, respectively) were obtained from Zyomyx, USA. Fab13A and Fab6x recognize different epitopes of hIL8, and yield different affinities.

4.3 Protein resistance of the SAM surfaces

As a prerequisite for the application of SAM surfaces in all the following studies, their ability to resist NSB of antibodies needs to be demonstrated. In the following, we will show that (a) designing ethylene glycol groups in the SAM and (b) applying non-ionic detergent in the interaction buffer helped to yield negligible protein NSB on SAM surfaces.

Since the early 1980s, surface grafted poly (ethylene glycol) (PEG) has been used to prevent adsorption of proteins from biological media.⁶⁹ The resistance of these films is well explained by the “steric repulsion” theory, which associates the inertness of the polymer brushes with the high conformational freedom of PEG chains in the near surface region. However, the ability to resist protein adsorption is also exhibited by conformationally restricted oligo (ethylene glycol) (OEG) terminated alkanethiolate SAMs. It thus appears that the protein resistance of these SAMs must be

attributed to effects other than steric repulsion. To explain the protein adsorption characteristics on a molecular level, calculations on the interaction of water with OEG clusters as well as Monte Carlo simulations of the OEG-SAM/water interface have been performed.⁷⁰ It has been generally accepted that a tightly bound layer of interphase water, which prevents direct contact between the proteins and the surface, causes the protein resistance of OEG-SAM.

P-20 is added routinely in the buffer from Biacore for minimizing protein NSB and avoiding sample depletion. It is equivalent to Tween-20, a polyoxyethylene sorbitan ester of fatty acid, known as a model non-ionic detergent to preserve the native protein structure and has a relatively high critical micelle concentration (CMC=0.05% (v/v)). Tween-20 is a vital reagent in clinical immunoassays with extremely primitive sensor surface-engineering,⁷¹ where the detergent is highly effective in preventing proteins adsorption and in displacing the adsorbed proteins. Tween 20 is similarly used in Western blot analysis.⁷² It was also carefully determined that both the minimum albumin adsorption amount and the minimum sessile water contact angle correlated closely with the CMC level of Tween-20, where a monolayer of Tween molecules forms with their hydrophilic heads oriented toward the exterior, i.e., the bulk phase.⁷³

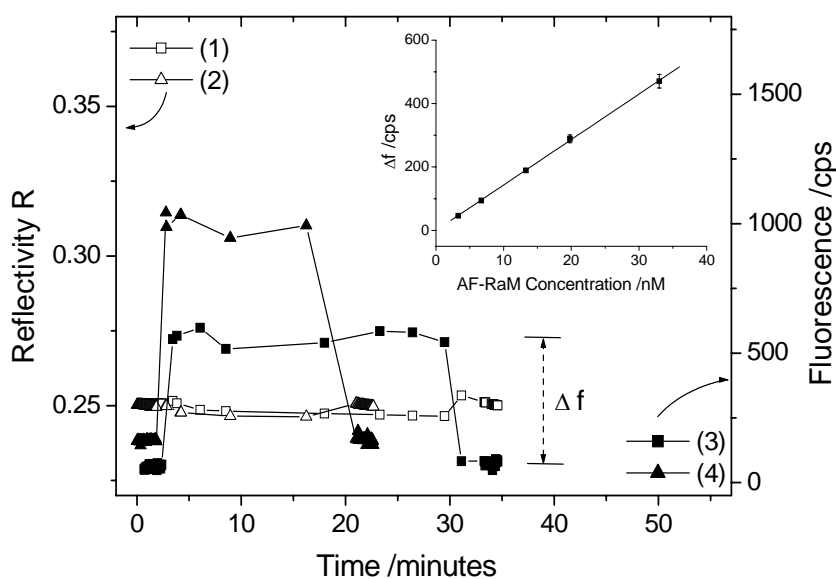


Figure 4.2: Resistance of EG SAMs and mixed SAMs ($\chi = 0.1$) to the nonspecific adsorption of 33 nM AF-RaM in HBS-EP buffer. (1) SPR signal on the EG SAM, (2) SPR signal on the mixed SAM, (3) fluorescence on the EG SAM, (4) fluorescence on the mixed SAM. The inset shows the relation between background fluorescence signal Δf and the bulk concentration of AF-RaM solution.

A pure EG SAM and a mixed SAM containing a relatively high molar fraction of biotin thiol ($\chi = 0.1$) were tested for the NSB level against a labeled IgG, AF-RaM. AF-RaM solution was injected

into the cell at a working concentration of 33 nM, in HBS buffer. As Figure 4.2 shows, an abrupt fluorescence signal increase was observed for both SAM surfaces upon injection of the antibody solution. The increase in the intensity, Δf , was about 470 and 940 counts per second (cps) for the EG SAM and the mixed SAM, respectively. This difference in this background intensity reflects differences in the degree of resonant surface plasmon excitation and the randomly scattered light, as it was found in sample-to-sample variations. When the running buffer replaced the sample solution, the fluorescence signal quickly dropped back to the baseline level in both curves. In the SPR signal, the reflectivity, R , showed only irregular noise caused by the sample solution exchange. No detectable minimum shift was found after comparing the SPR scan curves before and after the incubation. The fact, that no further rise in the fluorescence signal after the initial jump and the quick drop back to the original value was observed, suggests that there was no significant nonspecific binding of labeled antibodies to these SAMs. Although the detergent concentration used was significantly lower than its CMC, the co-effect of EG groups and the detergent completely inhibited the kinetically irreversible NSB from the labeled IgG. As for the origin of this fluorescence signal, contributions from two different sources are inferred. Firstly, there is a (small) fraction of labeled antibodies in the bulk solution, which can be excited by the evanescent tail of the surface-plasmon mode that extends some two hundred nanometers into the liquid phase. Secondly, the laser light, which is randomly scattered by the roughness of sensor surfaces, can also excite the fluorescent dyes in the solution. The sample-to-sample difference in roughness is inferred as a main source to the difference in Δf . On the same chip (e.g. on EG SAM chip), however, both contributions yielded a linear relation between Δf and sample concentration, as is shown in the inset of Figure 4.2, which reasonably follows Lambert-Beer's law.⁷⁴

4.4 Surface regeneration

The robustness of the SAM, enhanced by the internal hydrogen bonds, enables the repetitive removal of the bound antibodies by offensive reagents, including sodium dodecyl sulfate (SDS), guanidine hydrochloride (GdnHCl), etc. Although mild non-ionic detergent (such as beta-octyl glucoside) can also be used to competitively desorb proteins, it is generally demanded that the regeneration reagents denature the proteins for the fast disruption of the relatively stable interfacial immuno-complex. SDS is known as an anionic detergent with a high CMC level (1 mM) and also as a denaturing reagent.⁷⁵ Reports⁷⁶ have shown that SDS solutions below CMC were much less effective at removing proteins from surfaces, which then suggests also the requirement of micelle formation. Therefore, 5 mM SDS solution was applied in the experiments.

GdnHCl is a chaotropic reagent,⁷⁷ which is also an effective protein denaturant. Efficient working concentration is at high concentration, e.g., 4-8 M.

As a demonstration of the regeneration ability of both reagents, $\chi = 0.1$ surfaces were used and decorated firstly by 2F5. As shown in Figure 4.3, a pulse injection of 5 mM SDS solution of ~ 10 minutes totally removes the bound 2F5, which is shown by the return of the baseline to the original level (5). The biotin functionality was completely preserved, since another injection of 2F5 made the SPR signal climb up to almost the same level as the first injection. Another regeneration performed equally well afterwards.

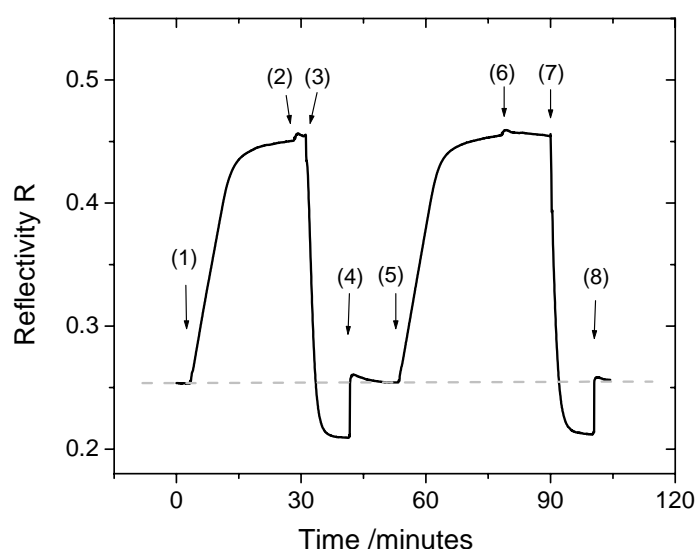


Figure 4.3: Example of repetitive regenerations of bound 2F5 by SDS solution: (1) 20 nM 2F5, (2) buffer rinse, (3) 0.5% SDS, (4) buffer, (5) 20 nM 2F5, (6) buffer rinse, (7) 0.5% SDS, (8) buffer. Dashed line represents the stable baseline level.

The regeneration of 2F5 by a 4M GdnHCl solution was even faster than the SDS solution, i.e., a pulse of ca. 1 minute was enough to completely remove the bound IgG. However, GdnHCl solution was proved to be more aggressive to the Au film than SDS solution probably due to its extraordinarily high Cl^- concentration. Long time exposure of the sensor surface to the GdnHCl is usually not recommended, since it causes significant distortion of the SPR angular curve.

In conclusion, such a regenerable surface makes the model system more interesting, in terms of direct comparison of different experiments performed with the same surface.

4.5 Mass-transport limited binding rates

The effect of the flow rate on the binding kinetics was investigated. A mixed SAM containing a biotin mole fraction $\chi = 0.04$ was selected and a 20 nM L2F5 solution was injected and rinsed over the surface at different rates. In order to put the focus on the binding kinetics and not to be involved to a ‘detuning’ problem for the fluorescence signal, cf. Figure 4.7, only the SPR signal was plotted in Figure 4.4. As one can see, the initial part of each association phase is a straight line, indicating that those are all mass-transport limited interactions. For a flow-through cell with a rectangular cross section, the mass-transport-limited forward rate constant k_M is approximated by Equation 2.55, which suggests that k_M is proportional to the cube root of the flow rate.

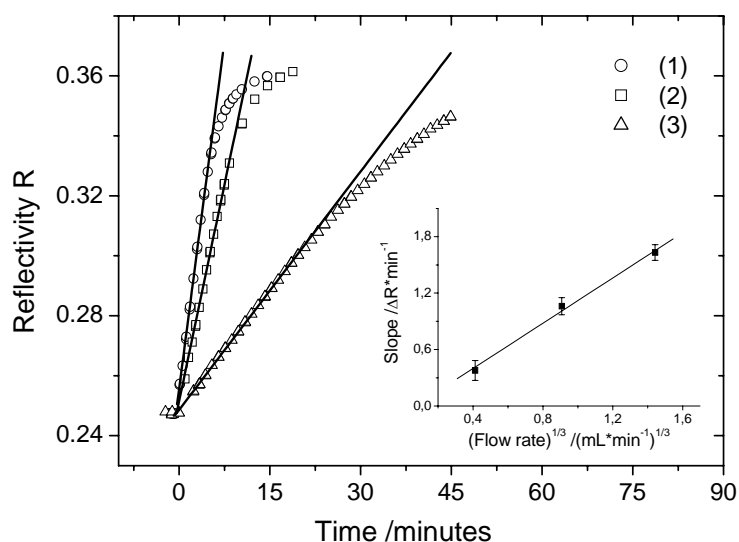


Figure 4.4: The effect of the flow rate on the binding profiles of L2F5. (1) 3 mL/min, (2) 0.75 mL/min, (3) 0.07 mL/min. The inset shows the relation between the cube root of the flow rate and the initial slope of L2F5 association curves.

By applying a linear fit for each binding curve at the initial association phase, and plotting the slope versus the cube root of the flow rate (the inset of Figure 4.4), one obtains a linear relationship. This was the evidence that all the binding kinetics were, indeed, controlled by mass-transport rates at the early stage. It is supposed to originate from:

- 1) The high biotin density and relatively low antibody concentration
- 2) The slow diffusion constant of IgG.

Higher flow rates accelerate the mass-transport controlled interaction, thus generally improving the detection sensitivity by increasing the signal per unit time.

4.6 Avidity influence on the IgG binding kinetics

IgG is a bivalent molecule (with two recognition sites per molecule). Its binding constant to the surface-attached ligands is a function of ligand density due to the accessibility of the antigenic epitopes, which is usually termed as the ‘avidity’ phenomenon. This phenomenon has been revealed by an antibody-peptide interaction model by SPR.⁷⁸ Mathematical model of multivalent binding to fixed ligands are also available.⁷⁹ These studies are especially valuable in understanding the basic mechanisms involved in signal transduction across cell membranes, which are generally initiated by the interaction between a multivalent molecule and membrane-restricted binding partners.

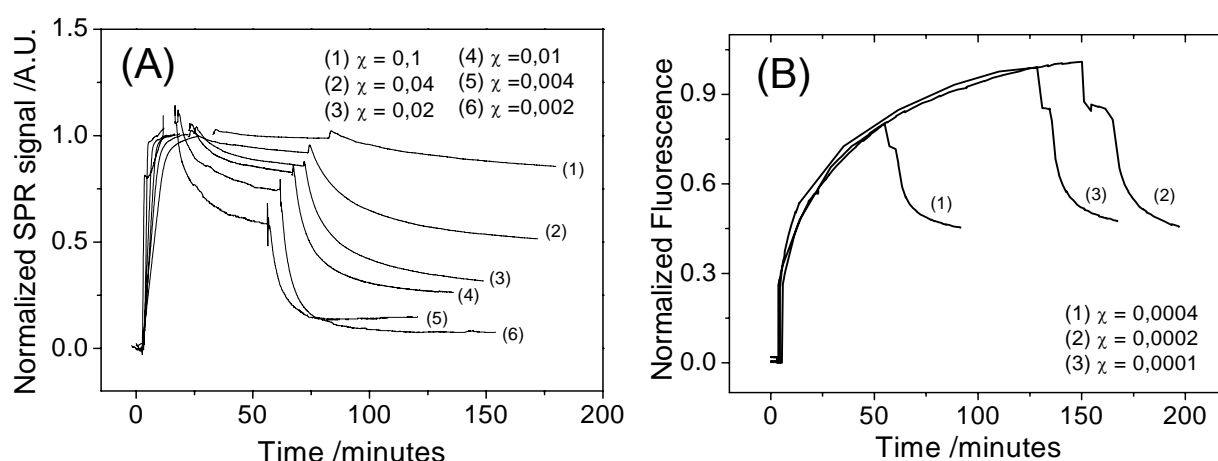


Figure 4.5: Representation of avidity controlled interaction between an antibody and its surface-coupled antigen. (A): SPR curves of the 2F5 associations/dissociations on surfaces with higher biotin densities; (B): Fluorescence kinetics of the 2F5 associations/dissociations on surfaces with lower biotin densities.

Our mixed SAM system shows its compatibility to conducting this study, since the surface biotin (epitope to 2F5) density can be systematically varied. A series of surfaces functionalized by different molar ratios of biotin/spacer thiols, χ ($\chi = 0.1, 0.04, 0.02, 0.01, 0.004, 0.002, 0.001, 0.0004, 0.0002, 0.0001, 0$ respectively), were used for this demonstration. The 2F5 antibody solution (20 nM) was introduced into the flow cell, and followed by a rinse step with pure buffer. In order to rule out the influence of interfacial rebinding, a competitive rinsing with a 1 mM biotin

solution was subsequently conducted. For the surfaces of $\chi < 0.002$, label-free detection by SPR was unable to give any convincing signal for kinetic evaluations. Therefore, L2F5 was applied instead and the fluorescent signal monitored. The SPR curves for the surfaces with $\chi \geq 0.002$ are plotted in Figure 4.5(A), normalized to the equilibrium amount bound, in order to allow for a better comparison of the adsorption/desorption rates of the antibody to various biotin surfaces.

The mass-transport effect firmly controlled the adsorption kinetics for all the surfaces studied, resulting in identical slopes at the initial binding phases for all the raw experimental curves (i.e. without normalization), which were virtually straight lines (cf. Figure 4.4). Typically, this effect is apparent at high surface site densities and low analyte concentrations. Normalized adsorption curves showed that the higher surface biotin density was, the later the binding could reach equilibrium, because times needed to reach equilibrium were limited by the delivery rate of antibodies from the bulk to the interface. Mass-transport played such a dominant role, that the adsorption phase did not allow to derive useful kinetics information. On the other hand, calculations⁷⁸ confirmed that the release of the antibody from the surface and the diffusion of free biotin towards the surface are much slower than the mass-transport rate in our experimental condition. Therefore, desorption rates reflected the affinity between the bound antibody and the biotin-moieties of the SAM surfaces. As shown in Figure 4.5 (A), apparently, the desorption rate increased with decreasing biotin density, for both the normal and the competitive desorbing processes. The trend clearly indicated a transition from a 1:2 to a 1:1 interaction stoichiometry between the antibodies and the surface antigens, because statistically less antibodies were able to bridge two biotins at more diluted biotin SAM surfaces.

Taking advantage of the sensitivity of the fluorescent monitoring mode, the binding signal on the surfaces of $\chi = 0.0004, 0.0002, 0.0001$ could be resolved, which are shown in normalized forms in Figure 4.5 (B). At such low surface densities, the adsorption phase was controlled by interaction kinetics, as indicated by the absence of the linearly increasing phase. Also, statistically, the IgG was unable to bridge two biotins at these low biotin densities. Therefore, the adsorption/desorption behaviors all represented the interaction between one Fab fragment with biotin, which were visibly identical. Of course, one could calculate the ‘critical biotin density’ based on the dimension of an IgG molecule.⁸⁰ However, it is difficult to be quantitative if ignoring, e.g., the phase separation of mixed SAMs,⁸¹ the conformation of the IgG, etc.

4.7 Self-quenching of Cy5 and AF 647

Alexa Fluor 647 and Cy5 are both widely used fluorescent dyes and spectrally identical.⁵⁹ For SPFS studies of DNA/PNA system, Cy5 labeling is more versatile due to the availability in the market. However, a better performance of AF dyes is usually suggested,⁵⁹ in terms of high brightness, pH insensitivity and less self-quenching, etc. Therefore, it is of great interest to compare their performances in SPFS protein studies, especially noticing the fact that most of the fluorescently labeled proteins contain multiple labels.

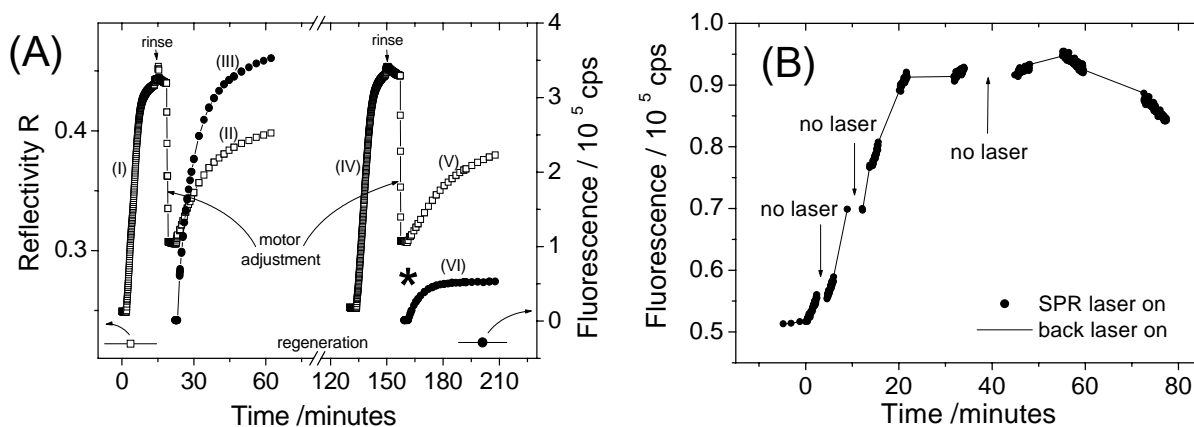


Figure 4.6: (A) Comparison of the performance of AF and Cy5 labeled secondary antibodies. (I), (II) SPR data of a 2F5 binding followed by an AF-RaM binding. (III) fluorescence signal of AF-RaM binding. (IV), (V) SPR data of a 2F5 binding followed by a Cy5-GaM binding. (VI) fluorescence signal of AF-RaM binding. Break axis omits the regeneration step (approx. 1 hour). Motor adjustments were used as indicated in order to keep SPR signal at a linear range. (B) Influence of Cy5 fluorescence by photo-bleaching using the SPR laser or the back laser.

As show in Figure 4.6(A) curve (I), we monitored the binding of label-free 2F5 antibodies to a $\chi = 0.1$ SAM surface. In the subsequent binding of AF-RaM, both the SPR (II) and the fluorescence (III) signals increased with similar kinetics. The surface was then completely regenerated after ~ 1 hour treatment with SDS solution. Afterwards, the same procedure was applied except that this time the secondary antibody was the Cy5-GaM. Nearly identical SPR signals were obtained in both cases (cf. (II) and (V) respectively), suggesting a similar amount of bound secondary antibodies. However, major differences were seen in the fluorescence signals (cf. (III) and (VI), respectively). The fluorescence emitted from Cy5 was much lower than that from AF 647, and did not quite follow the time course of its corresponding SPR signal, most notably seen after the point

indicated by a ‘*’ mark. Referring to the literatures,⁸² it is known that Cy5 easily undergoes intra-conjugate quenching by dimer formation or by a fluorescence resonance energy transfer (FRET) mechanism, if several dye molecules are attached to the same conjugate. On the contrary, higher density incorporation to the conjugate is allowed for AF dyes.⁵⁹ From this, we infer that for Cy5-GaM, not only intra- but also inter- conjugate quenching exists after exceeding a critical surface packing density ($\Delta R \approx 0,03$). Self-quenching, to some extent, counteracts the fluorescence increase due to the interfacial enrichment of Cy5-GaM, thus produced a strong saturation of the fluorescence kinetics curve after the ‘*’ point.

In order to derive a further understanding of the self-quenching effect of the Cy5 dyes, another experiment was conducted after refilling the flow cell with buffer in order to wash out all free antibodies in the bulk phase. A second HeNe laser (5mW, $\lambda = 633$ nm) was mounted on the backside of the flow cell allowing for a direct illumination of the sample surface from the prism backside. In Figure 4.6 (B), the fluorescence signal was relatively stable before time 0 attributed to the slow dissociation kinetics of the primary and the Cy5-GaM antibodies. The laser shutter was opened at time $t = 0$. The SPR laser kept illuminating the sample for a while in order to induce the expected photo-bleaching. However, the fluorescence signal increased instead. The increase paused if the shutter shielded the SPR laser. The same phenomenon was observed by the illumination from backside, by which any special effect attributed to the surface plasmon electromagnetic field was excluded. There are clearly 3 sections in the curve, namely a period of increasing fluorescence intensity during 0~25 minutes, a quasi-stable section during 25~60 minutes and a phase of decreasing intensity at times longer than one hour. We believe that in the early stage, the bleaching of a fraction of the fluorophores raised the total fluorescence yield by alleviating the self-quenching, which was in agreement with the ‘dequenching-by-bleaching’ report.⁸³ At a certain time the signal then starts to decrease because the amount of active fluorophores constantly decreases due to the ‘normal’ photo-bleaching effect. In contrast, only a very slow signal decrease was observed with AF labeled antibody upon continuous excitation by either one of the two lasers (data not shown). We conclude that AF dye is qualified for SPFS protein studies with the merit of less self-quenching and good photo-stability. Noteworthy is, the intermolecular self-quenching for AF dyes could also be observed at a three-dimensional matrix, after exceeding a critical packing density.

4.8 Detuning of fluorescence

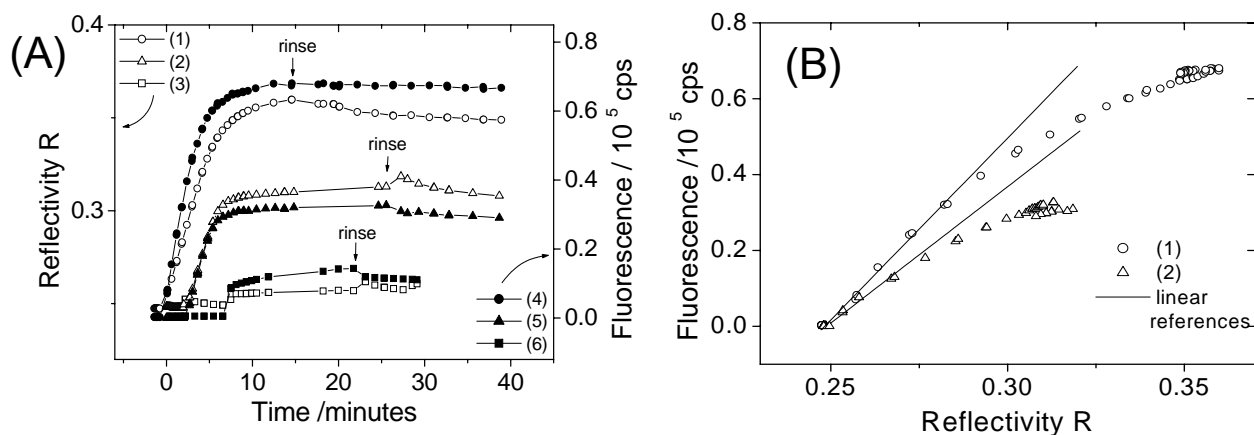


Figure 4.7: (A) Overlay of SPR and fluorescence results obtained on different mixed SAM surfaces. (1), (2), (3) are the SPR signals on $\chi = 0.04, 0.01, 0.001$ surfaces. (4), (5), (6) are the fluorescence signals on $\chi = 0.04, 0.01, 0.001$ surfaces. (B) The relation between the SPR and the fluorescence signals, (1) $\chi = 0.04$, (2) $\chi = 0.01$.

A direct comparison of the SPR (reflectivity) signals and the corresponding fluorescence intensities measured by SPFS was carried out by injecting 20 nM L2F5 into 3 different cells exposing 3 different biotin densities in the SAMs, i.e., $\chi = 0.04, 0.01, 0.001$, respectively. Figure 4.7 (A) shows the overlay of the kinetic curves. Decent surface plasmon and fluorescence signals were observed for $\chi = 0.04$ and for $\chi = 0.01$, owing to the large size of the IgG units and to the higher biotin density. However, at $\chi = 0.001$, the SPR signal disappeared into the sample exchange turbulence and the normal system noise, while the fluorescence could still be monitored out of the background. Correlations of both signals for $\chi = 0.04$ and 0.01 surfaces are depicted in Figure 4.7 (B), with the fluorescence being plotted versus the reflectivity, R . As expected, both curves show larger deviations from the linear reference curves for higher SPR signals. This fluorescence ‘detuning’ effect has been observed in previous study using biotinylated fluorescent latex particles.¹⁴ The mechanisms are assumed to be the same: since we monitor these two signals at a fixed laser incidence angle, the positive shift of the surface plasmon angular position results in a decrease of the light resonantly coupled which is used to excite the fluorophores. Although the real fluorescence signal can be obtained by performing an angular scan, this so called ‘detuning’ effect in practice could distort the fluorescence kinetic curves, leading to a miscalculation of kinetic constants. However, for the systems studied here, within a slight

variation of the reflectivity (0.03 ~ 0.04, corresponding to 0.1 ~ 0.12 degrees minimum shift), the correlation is approximately linear. On the other hand, the ‘detuning’ effect can be avoided by using a SPR program that follows the minimum as it changes with time or can be compromised by using an alternative setup configuration, e.g., Biacore instruments where the laser beam is pre-expanded to cover the working SPR minimum angle. The different initial slopes of the curves Figure 4.7 (B) may be attributed to sample-to-sample variations, or, to conformation difference of the bound antibodies that influences the effective fluorescence yield (as will be discussed in the next section).

4.9 Three dimensional IgG arrangement

As shown in Figure 4.1, there are two possibilities to realize a fluorescence immunoassay. The direct way needs to have the protein of interest labeled, which is sometimes difficult in real applications. In contrast, the indirect assay normally uses a labeled secondary antibody in order to get the desired signal. Convenient sources are the commercially supplied species-specific anti-IgG antibodies with fluorescent labels. The use of a secondary antibody can generally enhance the signal of the primary binding event. Nevertheless, it prolongs the assay duration and kinetic constants of the antigen - primary antibody binding cannot be obtained directly.

For the following experiments, a series of chips with systematically varied biotin densities ($\chi = 0.1, 0.04, 0.02, 0.01, 0.004, 0.002, 0.001, 0.0004, 0.0002, 0.0001, 0$ respectively) were prepared. Among them, the $\chi = 0$ chip was used as a negative control. In the direct assay experiments, L2F5 was allowed to run over the surfaces for more than 15 minutes. The indirect experiments were done as follows: (1) incubating the surfaces with 2F5 for 15 minutes, (2) switching to running buffer for a brief rinse, (3) exposing the surface to AF-RaM solution for more than 30 minutes. The primary binding (2F5 or L2F5) signals after 15 minutes contact time and the secondary binding (AF-RaM) signals after 30 minutes are given. Reflectivity data were converted to a SPR angle shift by the angular scan curve measured at the beginning of each experiment. Note that a certain underestimation of the fluorescence due to the ‘detuning’ effect, which cannot be excluded completely because the values were obtained from the binding, curves. However, this does not influence the semi-quantitative evaluation.

Plotted in Figure 4.8 are the end-point signals from these measurements. It is worthwhile to point out several interesting features in the figure.

- 1) The SPR data of L2F5 shows an identical trend to that of 2F5 (cf. curve 1 and curve 2). The slightly lower value of the L2F5 binding can probably be attributed to the random attachment of 4.4 dyes per antibody which reduces the affinity of the antibody to some extent, thus reducing the amount of bound antibody at a non-saturation concentration. Labeling may also change other properties such as hydrophobicity, flexibility, diffusion constant of the IgG, etc., which all influence the formation of an interfacial immunocomplex in a unpredictable way. For example, efforts have been reported to understand the effect of extrinsic labeling on protein dynamics.⁸⁴
- 2) Regardless of its further extension to lower biotin contents, the fluorescence signal of L2F5 exhibits a similar trend to its SPR signal (cf. curve 2 and curve 4). However, there is still a subtle nonlinear relation between both signals, which needs further investigation.
- 3) The SPR curve of the AF-RaM does not follow that of the primary binding curve (cf. curve 1 and curve 3). The stoichiometric ratio of AF-RaM to 2F5 reversed at a critical biotin density, i.e., $\chi = 0.014$. This is probably due to steric effects arising from the different surface concentrations of the primary antibody (cf. the schematic model in Figure 4.8). The AF-RaM reacts with all parts of mouse IgG in a rather nonspecific way. If there is sufficient lateral space for the secondary antibody to bind like in the case of lower primary antibody coverage (cf. Figure 4.8 (II)), as many as 2.5 AF-RaM molecules can bind to each individual 2F5 as calculated from the SPR signals (e.g. on the $\chi = 0.004$ surface). As the packing density of 2F5 increases, the epitopes of neighboring molecules start to mutually block each other. Thus, we see a largely reduced number of AF-RaM per 2F5 (cf. Figure 4.8 (III)) while the net amount of AF-RaM remained almost constant because of the increased number of 2F5. Similar findings were reported,^{61(B)} for a titration where the binding of streptavidin was severely sterically hindered by a self-assembled monolayer representing 100% densely packed biotin thiols.
- 4) Referring to the same amount of protein bound (as deduced from nearly identical SPR signal), AF-RaM yields a much stronger fluorescence intensity compared to L2F5 (cf. curve 4 and curve 5 in Figure 4.8, respectively), e.g., the data on the $\chi = 0.02$ surface. Both AF-RaM binding and L2F5 binding have almost the same angular shift (0.43 and 0.46 degrees, respectively), which means almost the same amount of bound IgG. The fluorescence intensity, however, differed substantially by a factor of 5.5 (2.8E5 and 5.1E4 cps, respectively). We noticed that the difference in labeling efficiency (dye-to-protein

ratio 4.8 and 4.4) and the ‘detuning’ effect (existing in both cases) had very little influence on the comparison of intensities.

- 5) The fluorescence intensity does not scale linearly with the SPR signal among the AF-RaM points (cf. curve 3 and curve 5), e.g., the data at $\chi = 0.004$ and 0.04. On the $\chi = 0.04$ surface, the fluorescence yield per unit amount of IgG is 2.5 times as high as on the $\chi = 0.004$ surface. We thus infer that, the fluorescence emission of the labeled antibody is dominated by the interfacial molecular architectures and distance dependent behavior of the fluorescence yield.

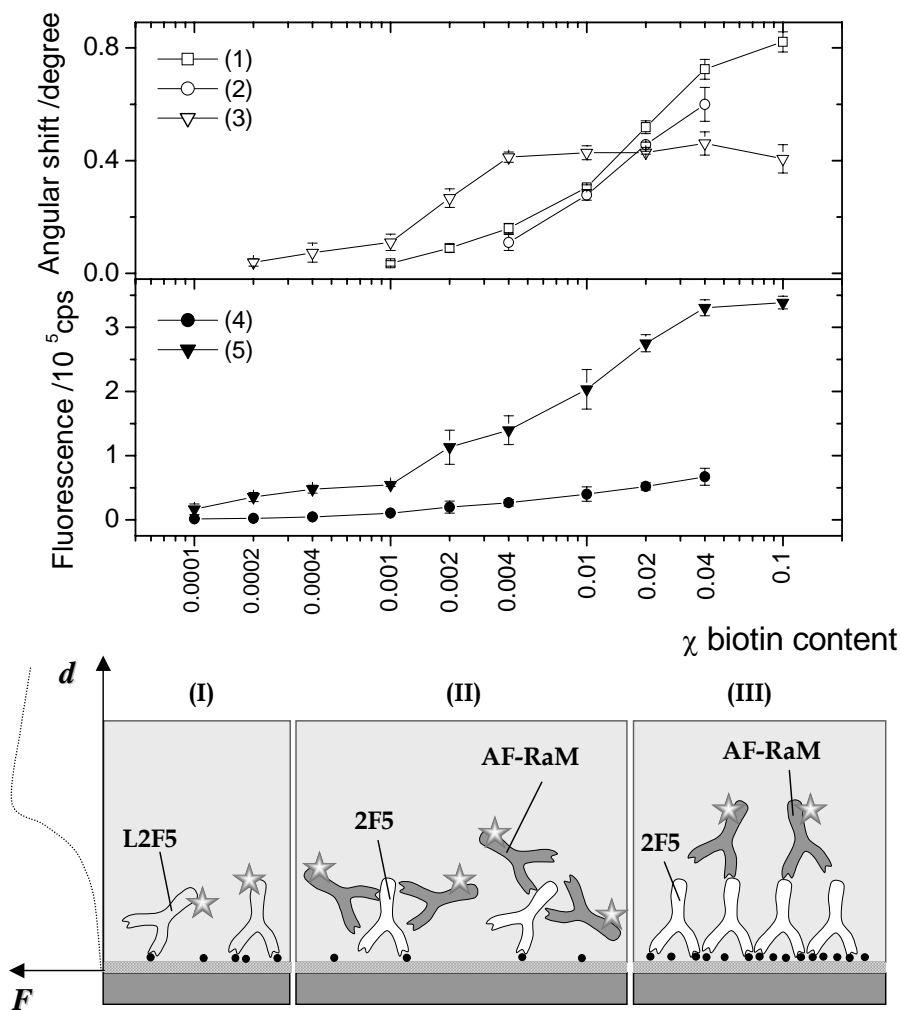


Figure 4.8: (A) The end-point results using the direct and the indirect detection schemes. (1) SPR results of 2F5, (2) SPR results of L2F5, (3) SPR results of AF-RaM, (4) fluorescence results of L2F5, (5) fluorescence results of AF-RaM. (B) More detailed schematics of the interfacial molecular architectures of (I) L2F5 binding, (II) 2F5 + AF-RaM binding on surfaces with lower biotin density and (III) 2F5 + AF-RaM binding on surfaces with higher biotin density. A drawing (F versus d) representing the distance dependent fluorescence yield above the gold/liquid interface is given on the left side.

Known from the fluorescence near metal theory, (cf. chapter 3) larger separation distances give a lower loss of fluorescence radiation in a range of $< 20\sim 30$ nm. The distance profile of the fluorescence yield is schematically drawn in Figure 4.8, scaled approximately to the interfacial protein models given on the right side.

From the crystallographic and transmission electron microscopic observation,⁸⁵ it is known that an IgG protein has a molecular weight of approx. 156,000 Daltons and consists of two identical Fab arms (antigen binding zone) and an Fc region, forming a 'Y' shaped molecule. In our testing system, the Fab arms of 2F5 (L2F5) faced to the SAM surfaces (Figure 4.8 (I)). The vertically orientated IgG has a height of approximately 12 nm (plus 1.6 nm for the mean thickness of the SAM layer^{61(A)}). At this height level, almost all of the primary IgGs were within in the energy-transfer region and the fluorophores attached were substantially quenched. In the indirect detection case, the binding of AF-RaM was based on the layer of primary antibodies. Obviously, a fraction of the dyes was sufficiently away from the metal surface and less quenched. On the other hand, as has been discussed earlier, the secondary binding is strongly affected by steric factors. At a lower primary IgG density, there is enough space around each primary antibody, allowing for a 'lateral approach' of several secondary antibodies, simultaneously (Figure 4.8 (II)). With the increase of the primary IgG density, there are less and less possibilities for the secondary antibody to fit into the residual free space of the primary antibody layer (Figure 4.8 (III)). Thus, the average dye-gold distance increases and the quenching effect is reduced.

4.10 SPFS detection of extremely diluted antigen densities

It is a major advantage of SPFS to have a much higher sensitivity than SPR. The advantage can be amplified by considering small molecules which carry fluorescent labels, e.g., Cy5-oligonucleotide. For the system studied here, it is meaningful to demonstrate the SPFS technique for probing SAM surfaces with extremely laterally diluted functional moieties. Figure 4.9 shows the overlay plots of the fluorescence kinetic curves obtained for $\chi = 0.0004, 0.0002, 0.0001$ and 0 surfaces obtained by the direct and the indirect detection schemes. We have already seen that the direct SPR detection fails for a $\chi = 0.001$ surface (Figure 4.7(A)). Hence the weak and distractive SPR signals obtained are not shown. It seemed that there might have been a trace amount of biotin contamination on the negative control chip surface causing the slow increase of Δf up to 700 cps within 60 minutes (cf. Figure 4.9 (4)), which was absent in the experiment with AF-RaM (cf. Figure 4.2). Despite of that, the Δf of the $\chi = 0.0004$ surface is more than 10 times higher than the

negative control within the same incubation interval, with the $\chi = 0.0002$ and 0.0001 surfaces showing a factor of 4.7 and 4 respectively (cf. Figure 4.9 (1), (2), (3), respectively).

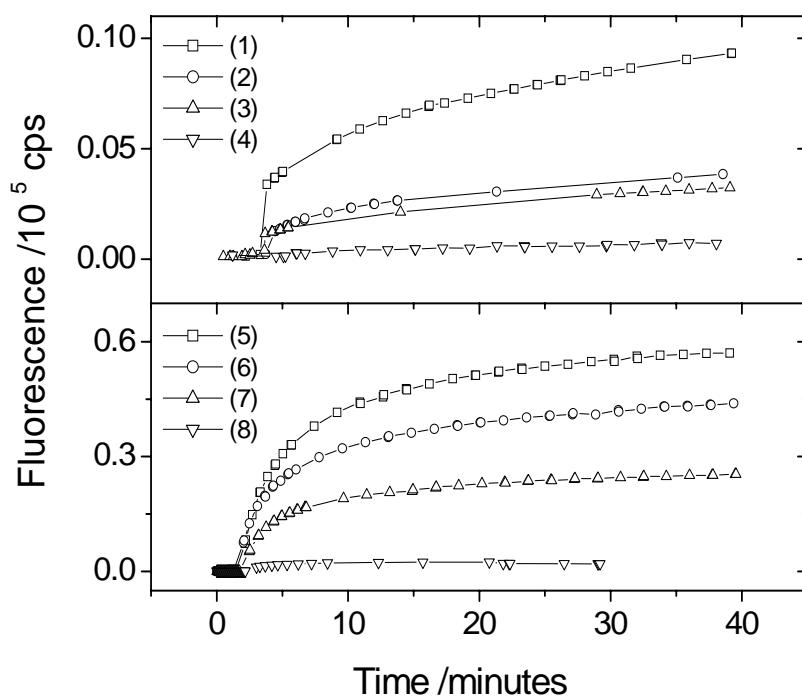


Figure 4.9: Sensitivity evaluations of SPFS on planar surfaces. (1), (2), (3), (4) are fluorescence binding curves of L2F5 on surfaces ($\chi = 0.0004, 0.0002, 0.0001, 0$, respectively). (5), (6), (7), (8) are fluorescence binding curves of AF-RaM on 2F5 treated surfaces ($\chi = 0.0004, 0.0002, 0.0001, 0$, respectively).

In the indirect detection case, the fluorescence signals for the $\chi = 0.0004, 0.0002$ and 0.0001 surfaces were approx. 28, 21 and 13 times higher, respectively, than the negative control (cf. Figure 4.9 (5), (6), (7), (8), respectively). Meanwhile, the signals were much stronger than the direct detection cases, due to the signal amplification by the AF-RaM. The SPR signal of the secondary binding were more pronounced because of the magnified amount of IgG on the surface which are, however, still not far from the noise range (data not shown). Assuming a value for the cross-sectional area of a thiolate of $A = 0.26 \text{ nm}^2$ ⁸⁶ and using the same biotin ratio as in the preparation solution, we calculate that statistically a biotinylated thiolate occupies an area of $2.6\text{E}3 \text{ nm}^2$ on the $\chi = 0.0001$ surface. This means that on average the next neighbor of each biotin is approx. 50 nm away. If each of the binding sites holds one antibody, we can claim that the fluorescence measurements can easily detect surface concentrations as low as 1 molecule per $2.6\text{E}3 \text{ nm}^2$ that corresponds to a surface concentration of approx. 10 ng cm^{-2} or coverage of 1.8% (assuming the cross-section of a Fab $A = 6.5 \times 3.5 \text{ nm}^2$). For smaller analytes, e.g., a protein with

Mw of only 1,000 Daltons (but with the same dye-label ratio), the achievable mass detection limit is approx. 70 pgcm^{-2} .

The model system is by no means optimized for exploiting the limit of detection (LOD) of the method for immuno-reactions. For example, we are still operating with a molecular architecture for which a significant fluorescence loss is unavoidable. Further efforts, such as tuning the thickness of the SAMs, or switching to a different interaction matrix are expected to improve the LOD of SPFS substantially. (cf. chapter 5)

4.11 A layer-by-layer model

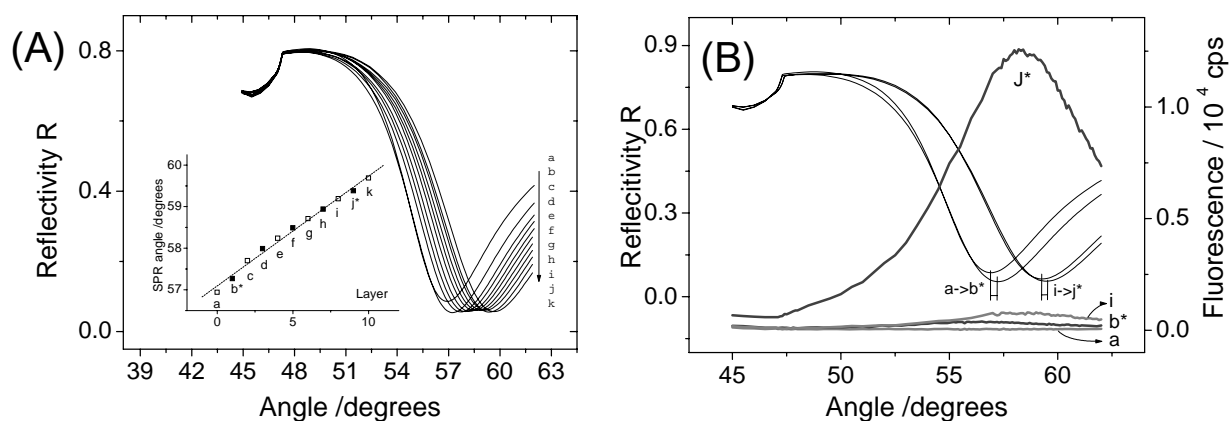


Figure 4.10: A layer-by-layer model built by biotin-streptavidin interaction. (A) the angular SPR curves of each layers. The inset shows the SPR minimum position as a function of layer number. (B) the fluorescence angular scans for layer ‘a’, ‘b’, ‘i’ and ‘j’.

Reports have shown that multi-layer thin films can be fabricated by an alternate deposition of two layers of molecules with affinity to each other. This technique is called layer-by-layer (LBL) deposition. Apart from the electrostatic interaction, a mostly applied strategy for the LBL technique, biological affinity can also be used to deposit proteins by means of, e.g., antigen-antibody interaction,⁸⁷ biotin-avidin interaction,⁸⁸ and sugar-lectin interactions.⁸⁹ A merit of this protocol is that all-protein thin films can be prepared. On the other hand, LBL techniques offer a way to control the separation distance between the molecules of interest to the base surface, which is of particular interest for investigating the distance behavior of fluorescence yield by SPFS.⁶⁸ In the following, we choose streptavidin and biotinylated IgG as the alternating molecules, a strategy reported previously.⁹⁰ The layers can be selectively decorated by applying labeled streptavidin.

A surface coated with self-assembled monolayer of 3-mercaptopropionic-acid, is used for the covalent attachment of AF-SA (Alexa-Fluor 647 labeled streptavidin) by means of active ester chemistry. A fraction of the carboxyl groups on the SAM surface was activated to form reactive N-hydroxysuccinimide esters using a solution of 0.2 M N-ethyl-N'-(3-dimethylaminopropyl) carbodiimide hydrochloride (EDC) and 0.05 M N-hydroxysuccinimide (NHS) in water. After this activation, 20 $\mu\text{g}/\text{mL}$ AF-SA prepared in sodium acetate, pH 5.0, was immobilized via the reaction of its nucleophilic groups (mainly the ϵ -amino groups in lysine residues). Afterwards, excess esters were then deactivated using 1 M ethanolamine hydrochloride adjusted to pH 8.5 with sodium hydroxide, which also desalted loosely bound protein. This reaction yielded a SPR minimum shift of $\sim+0.3$ degrees, corresponding a $\sim 40\%$ coverage of AF-SA molecule if referring to the previous calculations.⁹¹ This AF-SA layer contributed a fluorescence intensity of $\Delta f \sim 350$ cps from peak to peak (through 3 db attenuator), shown in Figure 4.10(B) as curve b. Subsequently, the following two steps were alternated.

- 1) A 20 $\mu\text{g}/\text{mL}$ biotin-IgG (biotinylated goat anti-mouse IgG) solution was injected to the flow cell. The binding equilibrium was reached in ~ 15 minutes. After a brief rinsing by pure buffer, SPR minimum angle was checked by an angular scan.
- 2) A 20 $\mu\text{g}/\text{mL}$ non-labeled streptavidin solution was injected. The binding equilibrium was also reached in ~ 15 minutes. After a brief rinsing by pure buffer, SPR minimum angle was checked by angular scan.

Plotting the SPR minimum shift versus the number of layers (cf. Figure 4.10(A)), we can see a linear correlation, which means the layers were consistently built up without any sign of receding up to 10 layers. A linear fit yielded a slope of ~ 0.26 degree/layer. Therefore the thickness of the multi-layer also increases linearly with the layer number with a slope of ~ 2 nm/layer, assuming a refractive index of 1.45 for both streptavidin and biotin-IgG.

On top of the 8th layer (a biotin-IgG layer) or the 4th double layer, i.e., a distance of ~ 16 nm to the Au surface, another AF-SA layer was built, yielding a much stronger fluorescence signal of $\Delta f \sim 12000$ cps, which compares dramatically to the fluorescence yield from the first AF-SA layer, by a factor of ~ 34 . This immediately gives the intensity difference between quenched and un-quenched fluorescence molecules, which strongly manifests the need of a decent spacing layer for the fluorescence molecules in real sensing applications.

Interestingly, the fluorescence peak from 1st AF-SA layer increased from ~ 400 cps to ~ 750 cps, after building up 7 bare protein layers. Two possibilities are speculated:

- 1) It was due to the conformational change of the 1st layer of AF-SA induced by subsequent layers on top of it;
- 2) The surface plasmon electro-magnetic field re-distribution due to the altered local refractive index, by the subsequent dielectric layers.

4.12 Affinity determination between hIL8 and its antibody fragments

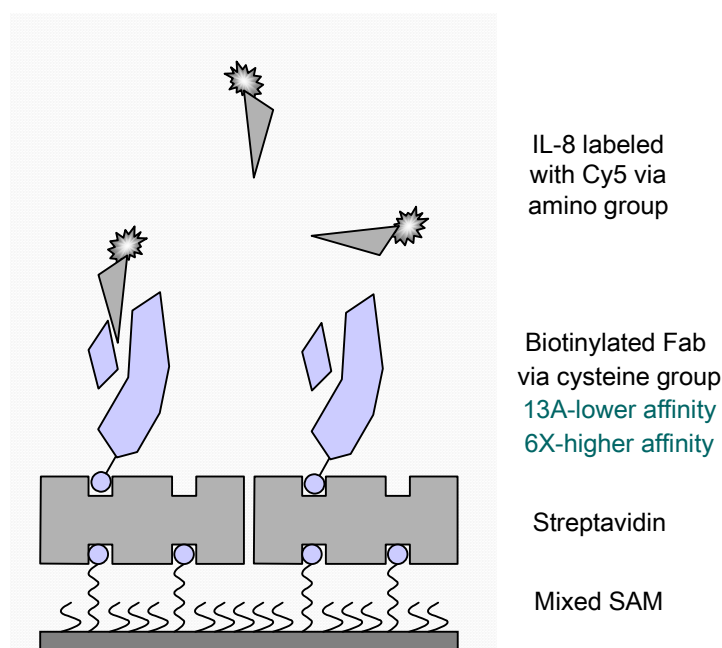


Figure 4.11: Schematic drawing of the hIL8 binding experiments performed on a supra-molecular architecture.

As an example of SPFS immuno-assay for clinically relevant samples, the affinity determination of hIL8 (human interleukin 8) with its antibody fragments (Fab13A and Fab6x) were performed, based on a multi-layer functional architecture (cf. Figure 4.11). Due to the small size of hIL8 (~18 kDa), SPR analysis is usually quite challenging. So we used dye labeled hIL8 and studied its binding kinetics through the fluorescence signal channel.

Firstly, streptavidin (SA) was bound to the biotin SAM (1:9), forming a functional layer for the attachment of the biotinylated Fab, as well as a layer to separate the fluorophore from being too close to the metal surface. Typically, the density of the SA monolayer is $\sim 2.2\text{-}2.5 \text{ ng/mm}^2$.⁹¹

Then, the biotin-Fabs were attached and saturated the SA surface at a level of $\sim 2.7\text{-}2.9\text{ ng/mm}^2$. Therefore, the stoichiometry of SA/Fab was close to 1.3, considering the molecular weights of SA and Fab (60 kDa and 55 kDa). In order to reduce the effects from the steric-hindrance/mass-transport/rebinding, experimentally we operated at a moderately reduced Fab density level, i.e., $\sim 2.1\text{ ng/mm}^2$ for Fab13A and $\sim 1.7\text{ ng/mm}^2$ for Fab6x, respectively. Finally, 100 nM hIL8 solution prepared in HBS buffer containing 500 $\mu\text{g/ml}$ BSA was injected across the Fab-derivatized surface and the interaction started. Upon equilibrium, the sample solution was exchanged against HBS buffer (with 500 $\mu\text{g/ml}$ BSA), and the dissociation process was recorded.

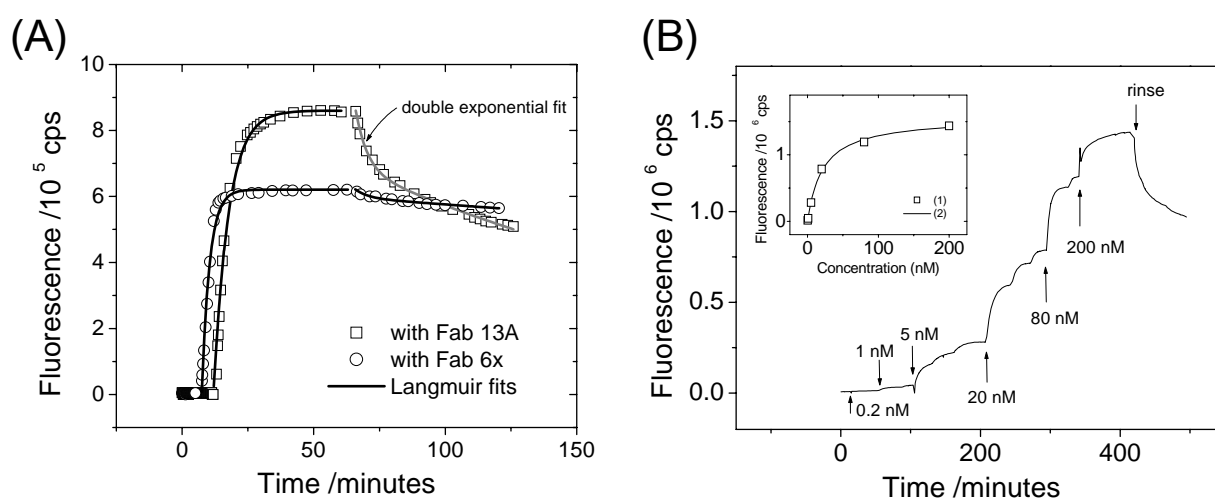


Figure 4.12: (A) Binding curves of hIL8-Cy5 on an unsaturated Fab surface. (B) The equilibrium titration of hIL8-Cy5 on saturated Fab surface, yielding the dissociation constant $K_D=21\text{ nM}$.

The complete binding curves are shown in Figure 4.12(A). A single-exponential kinetic model (cf. 2.4.3) was applied to yield the kinetic constants (k_{on} and k_{off}) and subsequently the affinity constants (K_A and K_D). However, an apparently bi-exponential dissociation behavior of hIL8/Fab13A made it difficult to yield the kinetic constants. Therefore, step-wise titration as an alternative way was applied to yield the Langmuir adsorption isotherm (cf. 2.4.4) and to determine the affinity of hIL8/Fab13A on a saturated Fab13A surface, shown in Figure 4.12 (B). The endpoint fluorescence values, as well as the calculated affinity parameters are listed in Table 4.1. Two features are noteworthy:

- 1) The affinity parameters obtained through the fluorescence channel were comparable to those through the label-free determination on a Biacore instrument (by Zyomyx Inc.). The

remaining small differences may be attributed to the influences from: a) the dye labels; b) different interaction matrices; c) the error from the bi-exponential behavior of the interaction.

- 2) The end-point fluorescence signals on Fab13A and Fab6x surfaces are different, due to the difference in the Fab density. By normalizing the signal to the corresponding Fab density, we yield similar ‘binding stoichiometry’. This is not surprising: the number of the hIL8 binding sites are similar for surfaces with similar Fab density for both Fabs, although their affinities are differed by ~ 2 orders of magnitude. 100 nM hIL8 solution was about to saturate both Fab surfaces, since this concentration was already significantly larger than both K_D values.

	SA (SPR)	Fab (SPR)	hIL8-Cy5 (Fluorescence)	Binding stiochiometry of hIL8/Fab †	K_D (SPFS)	K_D (Biacore)
Lower affinity Fab (13A)	0.49°	0.40°	8.5×10^5 cps	2.1×10^6 cps/°	21 nM	50-100 nM
Higher affinity Fab (6x)	0.50°	0.31°	6.2×10^5 cps	2.0×10^6 cps/°	0.3 nM	0.2nM

† : Fluorescence of hIL8/SPR of Fab

Table 4.1: Kinetic and affinity parameters obtained from the Cy5-hIL8/Fab interaction curves.

4.13 Conclusion

This chapter confirmed the potential of SPFS for the in-depth study of protein binding on a planar surface matrix. The interfacial binding models combined advantageous features of using mixed SAMs, e.g., in terms of controlling the antigen density and minimizing the nonspecific adsorption. Some fundamental understandings of SPFS protein study, as well as points towards the realization of an SPFS-based immunoassay have been addressed in this chapter. A portion of the work in this chapter has been published.⁹²

Firstly, it was shown that mixed SAMs provided an ideal system in terms of low non-specific protein binding and robust chemistry against regeneration treatment. Secondly, the kinetic features of the antibody binding to the surface-confined antigens (biotin) were investigated. Thirdly, the use of fluorophore Cy5 and Alexa Fluor 647 in SFPS-based immunoassays was compared. It was found that Cy5 exhibits strong self-quenching which makes it rather unsuitable for quantitative measurements. Fourthly, for the in-situ measurement of the binding kinetics, an angular ‘detuning’ effect was confirmed to negatively interfere with the fluorescence signal in

cases where large SPR signals were detected. Fifthly, an in-depth comparison between the SPR and the fluorescence signal reveals that the fluorescence yield of the dyes depends strongly on the separation-distance from the gold surface. Sixthly, we stress the ability of SPFS to detect binding to surfaces containing extremely diluted antigen-density, where the SPR signal failed to follow. Seventhly, a protein-based layer-by-layer system manifested and alleviated the problem of metal-induced fluorescence quenching. Finally, an immuno-recognition between hIL-8 and its Fab antibodies was studied based on the supra-molecular architecture built on the SAM.

5 SPFS immunoassay on 3D matrix

5.1 Motivations

Immunoassays have been demonstrated extensively employing a large variety of label-free sensing formats, including surface plasmon resonance (SPR),^{6, 93} waveguide sensors,⁹⁴ ellipsometry,⁹⁵ quartz crystal microbalance (QCM),⁹⁶ reflectometric interference spectroscopy (RIFS),⁹⁷ nanomechanics,⁹⁸ etc. SPR is one of the most versatile and sensitive tools among those, and has been well established both theoretically and instrumentally. However, it is still rather challenging if the direct detection of small molecules is required.⁹⁹ It seems that, less and less room is left for the sensitivity improvement within the label-free detection concept. In order to fulfill the stringent requirements in diagnosis, for drug discovery, proteomics or for the detection of environmentally hazardous compounds, etc., labeling detection remains the mainstream strategy.

In addition to the label-free SPR probing channel, SPFS offers a fluorescence signal channel that can similarly record biomolecular interaction kinetics. The fluorescence channel offers a very sensitive surface probing since it is a combination of: 1) the already very sensitive fluorescence technique and 2) the surface plasmon field enhancement. Concerning this, we predict that SPFS has the potential to become the method of choice in many of those aforementioned applications. Two reported examples have preliminarily demonstrated the sensitivity of SPFS. (1) Early in 1991, a (first) attempt was reported to develop a surface plasmon resonance based fluoroimmunoassay for human Chorionic Gonadotrophin (hCG), where a detection limit of less than 240 pM of hCG in serum was achieved.¹⁰⁰ (2) In year 2000, our group introduced surface plasmon field-enhanced fluorescence spectroscopy (SPFS) in detecting hybridization reactions between surface attached oligonucleotide probes and single-strand target DNA molecules binding from the bulk solution phase, with an estimated sensitivity of 100-200 strands per μm^2 .^{22(A)} With the excellent signal-to-noise ratio (SNR) of SPFS, investigations of subtle details of oligonucleotide interactions could be conducted.^{22(C)}

However, the establishment of the physical detection concept is only one side of a successful biosensor, a qualified surface matrix for molecular interactions is of equal importance. In the

previous chapter, all the studies were based on planar functional surfaces with the ligands attached in a 2D arrangement and distributed in a rather narrow distance range to the metal surface. Those planar matrices at least meet the following requirements as a functional matrix for biosensing: (1) they suppress non-specific protein adsorptions, (2) expose easily accessible moieties for protein immobilization, and (3) exhibit robust chemistry against regeneration conditions. However, such matrices have to face two major concerns before come into use in SPFS immunoassays. Firstly, the fluorescence emission from the bound fluorophores encounters significant quenching by metals for very small dye-to-metal distances (e.g. <10-30 nm), which compromises the benefits obtained from the SPR field enhancement. Secondly, a distinct distance-dependent fluorescence profile, originating from the co-effect of the decay of the evanescent surface plasmon field and the metal-induced quenching, suggests a potential signal deviation by, e.g., the unpredictable orientation and/or conformation of the analyte molecules, which is not desirable for practical sensing concerns. The fluorescence profile can be theoretically predicted (cf. Figure 5.1 (A)) and experimentally documented with model systems incorporating so-called ‘surface’⁶⁸ and ‘localized’¹⁰¹ plasmon phenomena, respectively.

In a cooperation with Biacore, we recognized that the three-dimensional (3D) surface layer from their commercial chips can be utilized to overcome these drawbacks of SPFS by extending the interaction layer away from the metal, as well as by integrating the fluorescence emission from the fluorophores at different distances from the sensor surface. Hence the CM5 sensor chip, a commercially versatile Biacore chip that gained significant reputations in the biosensing market, is employed in this study. Tethered to a SAM surface, the carboxymethyl-dextran (CMD) chains on the CM5 chip extend some 100 nm into the bulk medium, offering numerous carboxylic acid groups ready for the covalent attachment of bio-molecules. Although the precise distribution of bound bio-molecules along the CMD chains remains unclear, the larger steric hindrance near the tethering point may help to prevent the bio-molecules from being too close to the metal. Hence, such a layer-architecture perfectly matches to the optimized sensing region indicated in theoretical predictions. Similarly, other spatially extended functional chains (e.g. polymer brushes¹⁰²) or networks (e.g. plasma polymerized layers¹⁰³) can also be expected to offer the same features for SPFS, which however demand additional synthetic efforts at the current research stage.

In the following, we start with introducing the CM5 chip and its attaching chemistry, as well as its applicability in SPFS systems. Then, the correlation between the SPFS signal and the Biacore signal is established, for a quantitative description of the fluorescence response. Subsequently, the investigations on two immunoassay systems are presented. Firstly, a simple two-component interaction is employed, for the assessment of the limit of detection (LOD) of SPFS (cf. Figure

5.1(B)). Secondly, a sandwich SPFS assay is applied for the detection of prostate-specific antigen (PSA), which is considered as an example of real application of SPFS immunoassay (cf. Figure 5.1(C)).

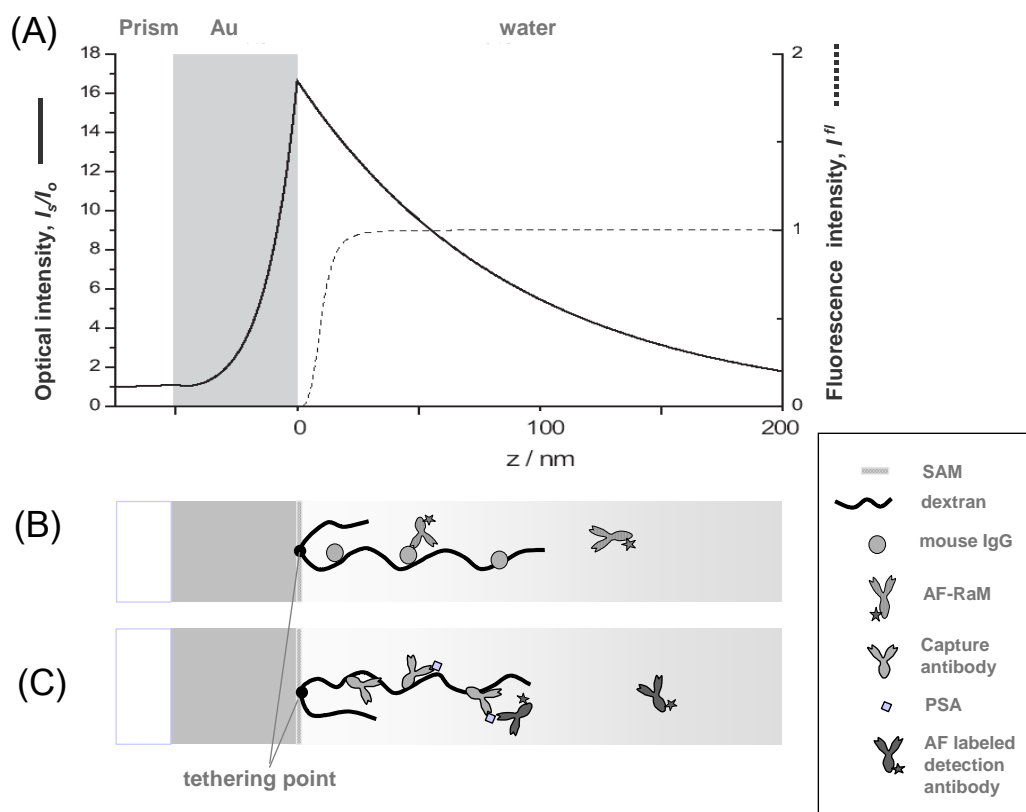


Figure 5.1: (A) Intensity profile of a surface plasmon with the evanescent field extending into the dielectric medium (water) in contact with the metal (Au) layer (solid line), and the fluorescence intensity profile of a fluorophore near a (quenching) metal surface (dashed line). (B) Schematic cartoon of an antibody-antigen interaction in a dextran matrix for LOD evaluation. (C) Schematic cartoon of a sandwich assay of f-PSA.

5.2 LOD assessment of SPFS

5.2.1 Materials

Modifying gold surfaces by CMD matrix for SPR sensing purposes was firstly described by Stefan Lofas in 1990.¹⁰⁴ Since then, it has been a great benefit to the enormous success of the commercial Biacore instruments. Briefly speaking, the matrix is constructed from a composite of a hydrophilic SAM and a covalently bound flexible carboxy-methyl-modified dextran brush. The SAM layer, created by adsorption of long-chain $1,\omega$ -hydroxyalkyl thiols on gold surfaces, serves as a barrier layer between the gold and the bulk solution. The hydroxy terminated layer is then

treated by epichlorohydrin to generate epoxy groups. Dextran, a linear polymer based on 1,6-linked glucose units, is then coupled to the epoxy groups in basic conditions. Subsequent reaction with bromoacetic acid results in the formation of carboxylic groups along the backbone of the dextran. These steps finally generate highly stable, flexible, non-crosslinked brush-like layers, which typically extends ~100 nm from the surface under physiological buffer conditions. Other than the properties for SPFS as mentioned before, some other properties of the dextran layers are appreciated for the immunoassay. Firstly, the dextran layer, together with the SAM, provides an effective barrier between the bulk solution and the gold surface, minimizing the non-specific binding of ligands. Secondly, its three dimensional structure greatly enhances the surface sensing area and thus enhances the binding signal.

CM5 chips without the plastic cartridge, amine-coupling kit (containing N-ethyl-N'-(3-dimethylaminopropyl)carbodiimide hydrochloride (EDC), N-hydroxysuccinimide (NHS) and ethanolamine), HBS-EP buffer, acetate buffer (10 mM, pH 5.0), glycine buffer (10 mM, pH 1.7), mouse IgG 2F9.1 were obtained from Biacore (Uppsala, Sweden). Alexa Fluor 647 labeled rabbit anti-mouse antibody was purchased from Molecular Probes (dye-to-protein ratio = 4.8).

5.2.2 Use of CM5 chip in the SPFS set-up

Of special interest for this work was the use of the commercially available CM5 chips also in our system. It uses D263 glass ($n = 1.523$ at 588 nm) as its substrate with a thickness of about 0.5 mm. Obviously, a refractive index mismatch existed between the prism (LASFN9, $n=1.85$ @ 633 nm) and the substrate. However, the surface plasmon reflectivity dip and the fluorescence peak appear at the same position as usual as shown in Figure 5.2. Theoretical explanation for this phenomenon has been given in 2.1.4.1. Briefly, addition of the 'extra' parallel glass layer between the prism and the metal does not change the in-plane component of the wavevector of the incident light, $k_{||}$, which is already increased by the high index prism to fulfill the momentum matching condition for the excitation of the surface-plasmon mode. On the other hand, we did observed two 'unusual' phenomena in the reflectivity signal when employing such a configuration. They are: (1) an abrupt increase of reflectivity at ~65 degree, luckily, slightly higher than the surface plasmon resonance minimum, which is clearly the commence of another total reflection at the prism/substrate interface, and (2) a weak interference pattern superimposed onto the originally 'smooth' angle-reflectivity curve, which originates, presumably, from the interference between two beams reflected from the interfaces of prism/substrate and substrate/water, respectively. The latter phenomenon is more troublesome because it sometimes influences the precise positioning of the total reflection angle and the resonance minimum in the angular scan curve. However, both

observations do not compromise the fluorescence detection, shown by an interference free fluorescence curve in Figure 5.2, curve (c).

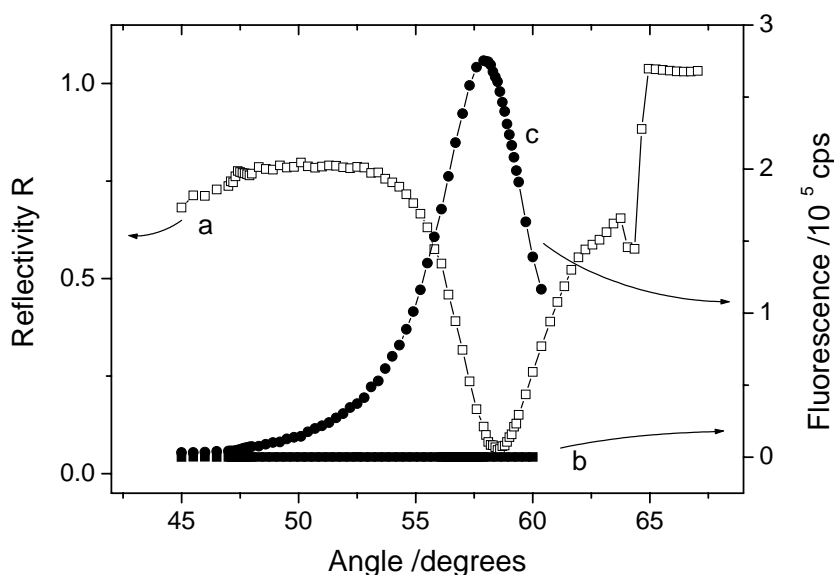


Figure 5.2: Example of a SPFS measurement with the CM5 chip. SPR reflectivity (a) and the corresponding fluorescence angular scan before (b) and after (c) the binding of Alexa Fluor 647 dye-labeled antibody.

5.2.3 Calibrate the SPR signal to surface protein concentrations

When operating with SPFS, the mass and the fluorescence signals arising from the binding of labeled analyte molecules can be recorded simultaneously. This is particularly more interesting for protein studies than for the DNA case, because the size of proteins is usually large enough to generate a good SPR signal. Thus, it is possible to establish a correlation between the fluorescence and the surface concentration of the bound molecules. Moreover, the correlated information from SPFS allows us to extract information about the three-dimensional interfacial arrangement of biomolecules.⁹²

In 1990, Stenberg and his colleagues at Biacore calibrated the SPR signal, i.e., the shift of the SPR minimum, with the absolute molecular surface concentration σ determined by using radio labeled proteins.¹⁰⁵ They found the correlation is $\Delta\theta/\sigma = 0.10 \pm 0.01 \text{ }^\circ (\text{ng mm}^{-2})^{-1}$, largely independent of the size of the protein. Thus they defined 1 RU (resonance unit) corresponding to a protein concentration of 1 pg mm^{-2} . This enables us to correlate our SPR signal to the absolute surface concentration, if we can establish a correlation between the SPR signals measured by our instrument and Biacore, respectively.

	SPFS	Biacore
Wavelength of laser	633 nm	760 nm
Geometry of Prism	Right-angular	Half-cylindric
Refractive index of Prism	1.85 at 633 nm	1.52 at 760 nm

Table 5.1: Comparison of some instrumental parameters of the two SPR set-ups

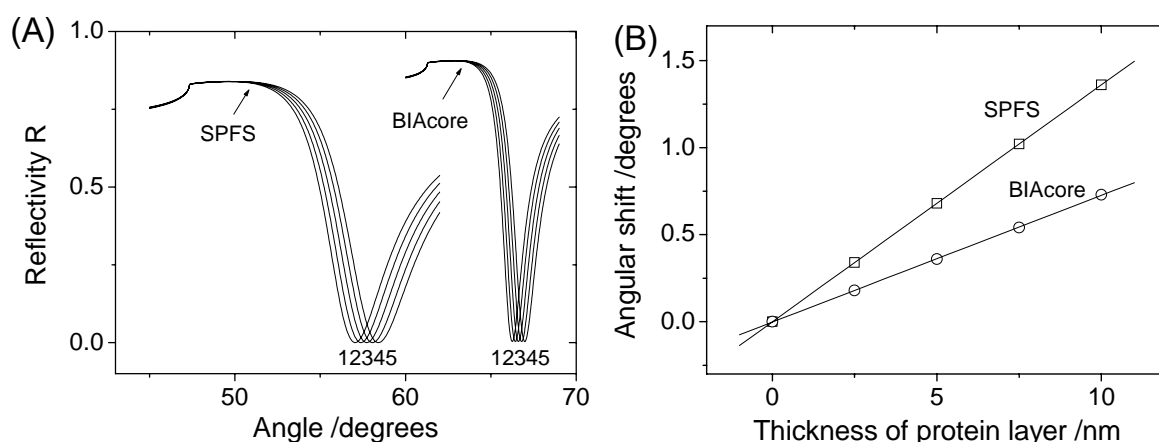


Figure 5.3: (A) Fresnel 4-layer (prism, gold, protein, water) simulation curves for the Biacore and the SPFS reflectivity measurements, respectively. In both cases, 50 nm gold layer is assumed and curve (1), (2), (3), (4), (5) corresponds to the protein ($n=1.45$) thickness of 0, 2.5 nm, 5 nm, 7.5 nm and 10 nm, respectively. (B) Simulated SPR minimum shift versus assumed protein layer thickness. Both solid curves are a linear fit to the data.

Due to the differences in the optical arrangement between the Biacore instrument and our instrument (listed in Table 5.1), the SPR responses are different upon the same amount of binding, e.g., from a protein. Based on those parameters, angle-reflectivity curves can be calculated by Fresnel calculation for a 4-layer system (Figure 5.3 (A)). The thickness of the ‘protein’ layer (the 3rd layer) was chosen at 0 nm, 2.5 nm, 5 nm, 7.5 nm and 10 nm, respectively, assuming its refractive index $n = 1.45$. The corresponding angular shifts of the SPR minima are plotted for both instruments, respectively, in Figure 5.3(B). Each group of data can be perfectly fitted by a straight line, which confirms the linear SPR response to such a range of film thickness variations. The difference in slope, on the other hand, indicates the difference in response. With the same thickness growing, our instrument obtains a higher angular shift of the resonance minimum by a

factor of 1.866, which is a direct consequence of the difference in the optical design. Thus, the surface concentration correlation for our SPR is:

$$\Delta\theta/\sigma = 0.19^\circ (\text{ng mm}^{-2})^{-1}. \quad \text{--- 5.1}$$

Another approach is determined the surface protein concentration by extrapolating refractometric measurements.⁹¹ By applying the following relation the protein density A can be calculated:

$$A = d \cdot \frac{(n - n_0)}{\partial n / \partial c} \quad \text{--- 5.2}$$

where d is the thickness of the protein layer, n and n_0 are the refractive index of protein and water, respectively. $\partial n / \partial c$ is the refractive index increment of the dissolved protein molecule in solution, determined by refractometric measurement. For instance, for a streptavidin in solution, $\partial n / \partial c$ is $0.212 (\text{g/mL})^{-1}$. From a typical SPR measurement of streptavidin binding on a 1:9 biotin SAM surface, we usually obtain a SPR minimum shift of $0.47^\circ \pm 0.02^\circ$, which yields a thickness of 4.0 nm, assuming $n=1.45$ and $n_0=1.33$. From these parameters, the protein density is calculated to be $A=2.26 \text{ ng/mm}^2$ using Equation 5.2. Therefore, the experimental surface concentration correlation is $\Delta\theta/\sigma = 0.21^\circ (\text{ng mm}^{-2})^{-1}$, which is in good agreement with the value from the first calculation. The small discrepancy may originate from the experimental errors and/or the error from the linear extrapolation of $\partial n / \partial c$ from solution to the surface.

The correlation applies for commonly used proteins, since they have similar refractive indices and do not differ considerably with respect to their SPR response.¹⁰⁵

5.2.4 Protein immobilization to a dextran matrix

A mixture of EDC and NHS can be applied to generate sites (active NHS-esters) for the coupling of amino- or hydrazine groups. Commonly, proteins can be directly coupled to the activated sites via their nucleophilic groups (e.g. ϵ -amino groups in lysine residues). The immobilization of IgG onto CM5 chip is quite straightforward by using the commercial kit and following a repeatedly tested protocol. The key of this protocol is utilizing electrostatic attraction forces for pre-concentration of the protein in the matrix. For that, a solution with a pH smaller than protein's isoelectric point and low ionic strength is used for the protein preparation. As a result, the positively charged proteins accumulate in the activated matrix possessing significant residual negative charges, which facilitates an efficient and fast covalent immobilization.

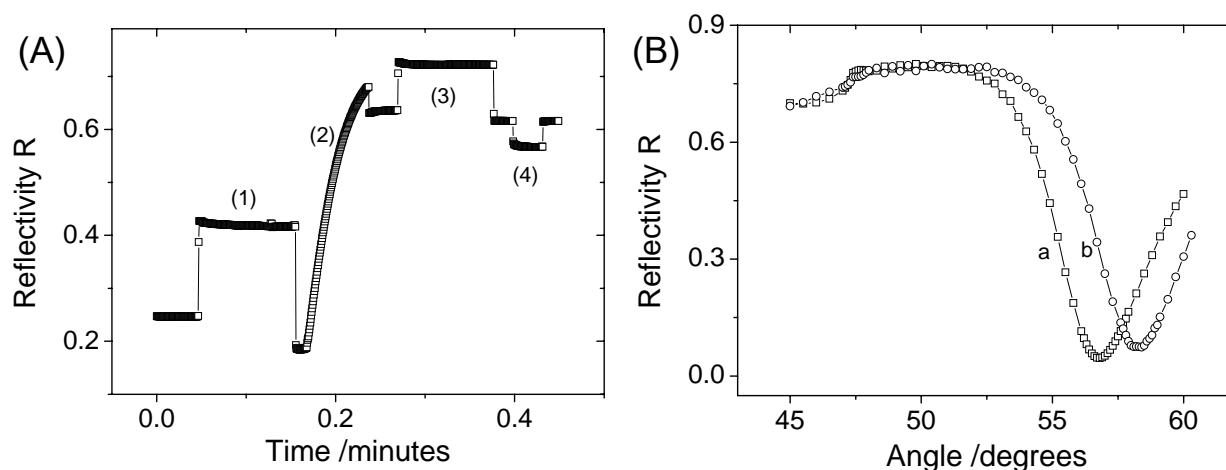


Figure 5.4: (A) Typical immobilization curve of α -MIgG1 to a dextran surface. (1) Activation of the carboxyl groups by a mixed EDC/NHS solution. The observed response is due to the differences in the bulk refractive indices between EDC/NHS solution and the running buffer HBS-EP. (2) Injection of 30 $\mu\text{g/ml}$ α -MIgG1 in sodium acetate buffer. (3) Deactivation of unreacted esters and desalting of electrostatically bound protein by injection of 1 M ethanolamine at pH 8.5. The observed response is due to the differences in the bulk refractive indices between the ethanolamine solution and the running buffer HBS-EP. (4) A pulse injection of glycine buffer. (B) Angular scan curves before (a) and after (b) the immobilization of α -MIgG1. The angular shift corresponded to a IgG concentration of 7 ng mm^{-2} .

A typical working diagram is shown in Figure 5.4 (A). The dextran matrix was activated for 10 minutes by exposing to a fresh mixture of EDC/NHS, forming the terminal NHS ester moieties ((1) in Figure 5.4 (A)). IgG is then injected at a concentration of $\sim 30 \mu\text{g/ml}$ prepared in sodium acetate buffer (10 mM, pH 5.5) and incubated with the surface for a certain period of time ((2) in Figure 5.4 (A)). Controlling the reaction time during this period can quantitatively control the loading of IgG. Unreacted active groups were deactivated by an injection of ethanolamine hydrochloride solution ((3) in Figure 5.4 (A)), which also desalted the loosely bound IgGs. Finally, a pulse injection (3 minutes) of glycine buffer (10 mM, pH 1.7) was applied as a so-called ‘chip-conditioning’ step ((4) in Figure 5.4 (A)). This step aims at further desorbing loosely bound IgGs and provides a more stable baseline for the following SPFS assay. Two angular scan curves (Figure 5.4(B)) were obtained before (a) and after (b) the immobilization step in order to assess the amount of protein immobilized. The angular shift can be converted to a surface IgG concentration by Equation 5.1.

5.2.5 LOD of SPFS

A simplified interaction model is needed for exploring the minimum number of target molecules per unit area that can be detected by SPFS. In the following, we focused on the interaction between mouse IgG and its labeled antibody, by covalently immobilizing the mouse IgG 2F9.1 on

the surface and then study its interaction with a series of concentrations of AF-RaM solutions. Two kinds of surface architectures were compared, namely a lipoic acid functionalized surface (LA chip) and a dextran surface for demonstrating the advantage of the three-dimensional matrix in boosting the sensitivity of SPFS.

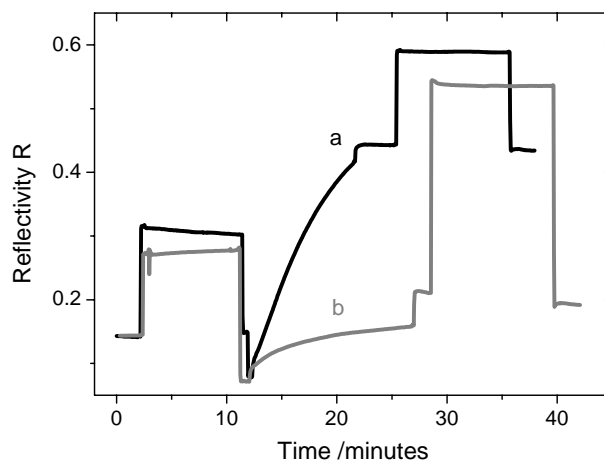


Figure 5.5: Immobilization of 2F9.1 on (a) the dextran matrix and (b) a planar lipoic acid modified surface. The starting levels of both curves are adjusted, for better comparison.

Lipoic acid is a versatile reagent for functionalizing gold surfaces with a decent amount of carboxylic acid groups.¹⁰⁶ LASFN9 substrates with a freshly evaporated 50 nm gold film were immersed for $t > 24$ hours into a 2 % (w/v) alcoholic LA solution at room temperature. Before use, the substrates were rinsed with a copious amount of ethanol and dried by a stream of nitrogen.

Immobilization diagrams for 2F9.1 on both the LA chip and the CM5 chip are shown in Figure 5.5 at room temperature. The 2F9.1 loading level on the LA chip (angular shift of the SPR minimum, $\Delta\theta = 0.18^\circ$) was much lower than that on the CM5, due to the difference in the amount and the accessibility of carboxylic acid groups between the 2D and 3D matrices. By controlling the contact time of the 2F9.1 solution (cf. step (2) in Figure 5.4(A)), we could easily manipulate the loading level on 3D matrix to mimic the 2F9.1 amount on LA surface. Four different loading levels were realized for the CM5 chips, corresponding to 1.51, 1.33, 0.61 and 0.088 degree of the SPR minimum shift, respectively.

For the concentration analysis by SPFS, we operated under mass-transport limited binding conditions in the association phase (cf. 2.4.2). Usually, at a relatively low analyte bulk concentration, the initial binding is under mass-transport control. The binding rate is constant and not related to the interaction affinity. The slope of binding is proportional to the (active) analyte

concentration. The linear zone of the dose-response curve at the lower concentration end is theoretically unlimited.

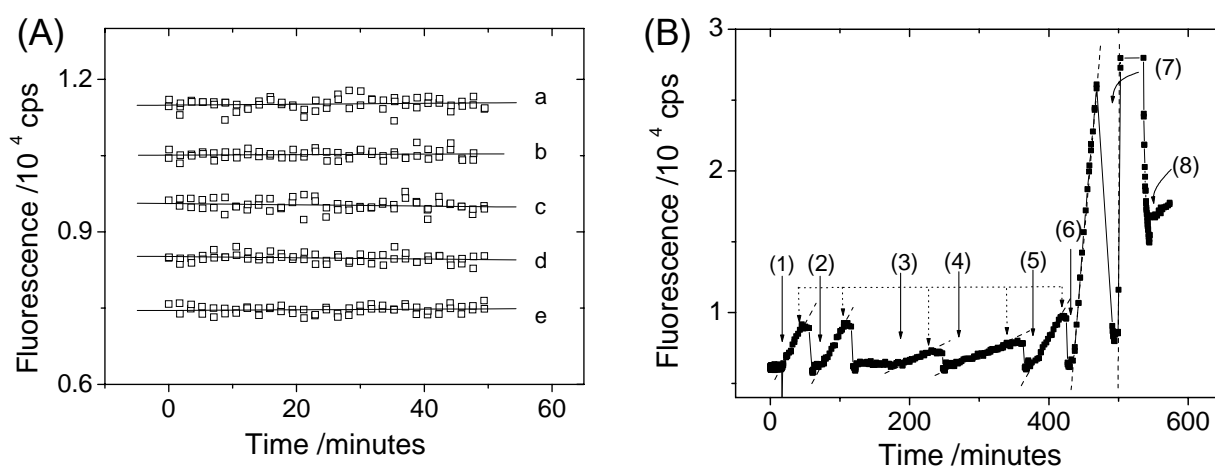


Figure 5.6: (A) Vertically spread fluorescence responses upon 5 repetitive injections of HBS-EP buffer as a blank. All original curves have the same fluorescence signal level. Solid lines are the linear fits for obtaining the different slopes, (a) 0.87, (b) 0.49, (c) -1.25, (d) -1.21 and (e) 0.61, respectively. Mean and SD of these values are -0.098 and 1.043, respectively. Thus, mean+3*SD is 3.03 cps min⁻¹. (B) One of the working curves for LOD evaluation. The 2F9.1 loading level is 1.33 degree. (1) 333 fM, (2) 333 fM, (3) 67 fM, (4) 67 fM, (5) 333 fM, (6) 3.3 pM, (7) 33 pM of AF-RaM and (8) pure HBS-EP buffer were injected subsequently. Connected dotted arrows indicate the points where a brief rinse by HBS-EP buffer was started. Regeneration was performed after every injection. Dashed lines are the linear fits to the binding curves. Flow rate was 3 mL/min for all the experiments.

5.2.5.1 Baseline deviation

Before circulating the AF-RaM solutions over the sensor surface, five replicates of HBS buffer injection as ‘blank’ were applied in order to quantify any baseline deviation at room temperature. One example is shown in Figure 5.6(A). Five slopes were obtained by linear fitting, and analyzed statistically. The sum of the mean and 3 times the standard deviation (SD) is considered as the baseline fluctuation, which is typically 3-5 cps min⁻¹.

5.2.5.2 Dose-response curve

A typical working curve at room temperature is shown in Figure 5.6(B) on a CM5 chip with a considerable 2F9.1 loading level (1.33°). As can be seen, a constant slope was obtained in every binding curve, which means that mass-transport limited conditions were established at all AF-RaM concentrations studied. The interaction period for each concentration was typically 30 ~ 60 minutes and was at least duplicated in order to get a dose-response curve. Note that the regeneration by glycine buffer was incomplete after higher concentrations were applied, but visually better in the case of lower concentrations, which was probably due to the poorer SNR condition in the latter case. One drawback of the current regeneration strategy is that, the sensor

chip may be ‘contaminated’ when analyte solution at a higher concentration (> 10 -fold) is analyzed, which makes the baseline rather high and unstable and no longer suits the analysis of the lower concentrations (e.g. the baseline after a HBS injection at arrow (8) in Figure 5.6(B)).

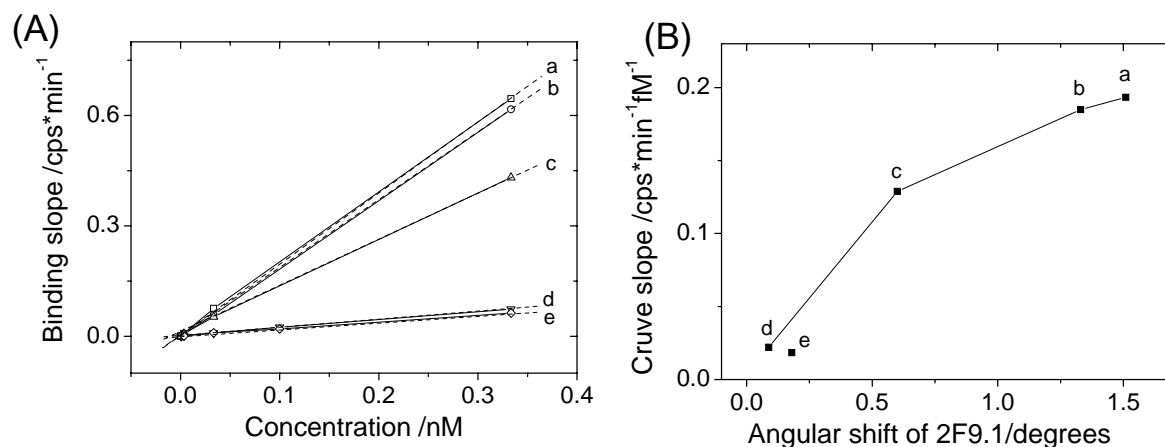


Figure 5.7: (A) Dose-response curves of the different surfaces with different 2F9.1 loading levels. (a) CM5, 1.51° , (b) CM5, 1.33° , (c) CM5, 0.61° , (d) CM5, 0.088° , (e) LA, 0.18° . Dashed lines are the linear fits. (B) Slopes of the dose-response curves versus the 2F9.1 loading level. (a) CM5, 1.51° , (b) CM5, 1.33° , (c) CM5, 0.61° , (d) CM5, 0.088° , (e) LA, 0.18° .

The dose-response curves on different surfaces are presented in Figure 5.7(A). Apparently the slopes of the dose-response curves, representing the binding probability of AF-RaM, are dependent of the 2F9.1 loading level on the CM5 chips as shown in Figure 5.7(A) (a), (b), (c), (d). The curve that links these points deviates from a linear relation which can be explained by the following consideration. Firstly, the epitopes are mutually blocked at high surface antigen density, leading to a decrease of the recognition site number. Secondly, one antibody can actually access two antigens if the distance among the antigen molecules is statistically closer at higher density (antibody ‘avidity’). Thirdly, a higher antigen density causes a higher probability for cross-linking the dextran matrix, which increases the viscosity of the interaction environment. A much lower slope was obtained for the dose-response curve of LA chip (Figure 5.7(A) (e)), although the 2F9.1 density was higher than (d). One obvious explanation is that the metal induced fluorescence quenching is less for the CM5 chip than for the LA chip. Another possibility is the difference in antibody’s recognition efficiency between the two matrices. As one can expect, the dextran chain extends ~ 100 nm into the bulk solution, providing a nearly homogenous condition for biomolecular interaction and thus a higher interaction probability. However, it will be more difficult for the antibody to approach the epitope fixed on flat surface due to steric hindrance issues. This can be further clarified by comparing their dose-response curves obtained from the

label-free response from pure SPR measurements. In any case, the fact that one can obtain dose-response curves with much steeper slope (thus higher sensitivity) confirms the advantage of using a 3D matrix in the SPFS-based assays.

A higher sensitivity was achieved on the CM5 chip with the higher 2F9.1 loading density as shown in Figure 5.8 in a double-logarithmic graph. The curve spans more than 4 orders of magnitudes of the analyte concentration (from 13 fM to 333 pM). The linear fitting line illustrates the excellent quality of the dose-response curve as long as the concentration analysis is performed under mass transfer conditions. Extrapolating the linear curve to the baseline deviation level ($\sim 3\text{--}5\text{ cps min}^{-1}$) results in a theoretical detection limit of 7.5 fM. Practically, however, the binding curves at the lowest concentration, 13 fM, were already too weak to provide any clear evidence of binding. Therefore, the LOD is given at 25 fM for an interaction period of less than 1 hour, corresponding a constant signal-growing rate of $\sim 9\text{ cps min}^{-1}$. Obviously, extending the interaction time or increase the flow rate will improve the signal accumulation and realizing better LOD value.

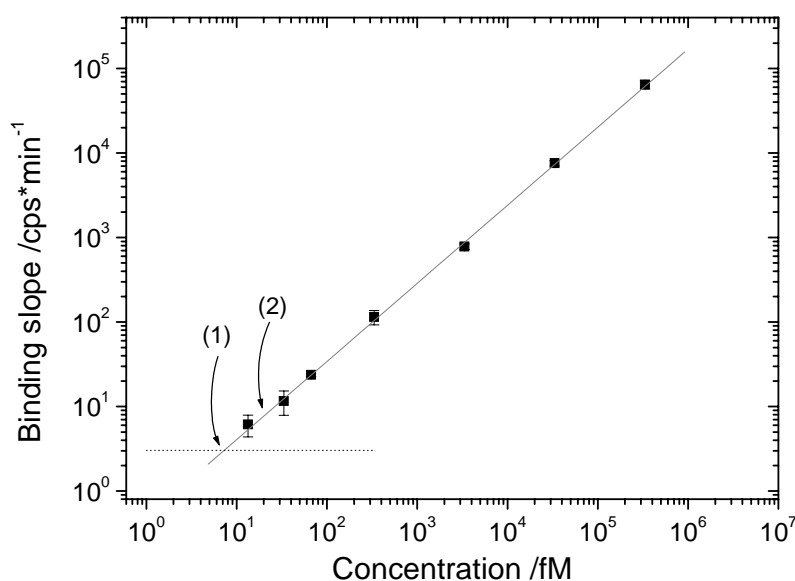


Figure 5.8: Double-logarithmic plot of the dose-response curve of the AF-RaM binding to the dextran surface loaded with highest 2F9.1 level (1.51 degree). The solid line is the linear fit. The dotted line represents the baseline fluctuation level (3 cps min⁻¹). Theoretical (1) and practical (2) LODs are indicated.

5.2.5.3 LOD at atto-molar level

The aforementioned LOD in the lower femto-molar range can be further improved by considering the essential elements of fluorescence detection system. They are: (1) the excitation source, (2)

the fluorophore, (3) the wavelength filters used to isolate emission photons from excitation photons, and (4) the detector that registers emission photons from excitation photons and produces a recordable output. Therefore, efforts were made such as increasing the excitation (laser) intensity ($\times 16$), decreasing the background signal from the excitation source via appropriate masking, as well as by equipping an objective with larger aperture ($f = 50$ mm, diameter = 40 mm) for efficient fluorescence collection. It has been observed that increasing the laser intensity was the most effective way, which intimates that noise level (background fluorescence) grows not as fast as the signal. However, such a strategy is not recommended for usual sensing purposes, since higher excitation intensity induces higher photo-bleaching probability.

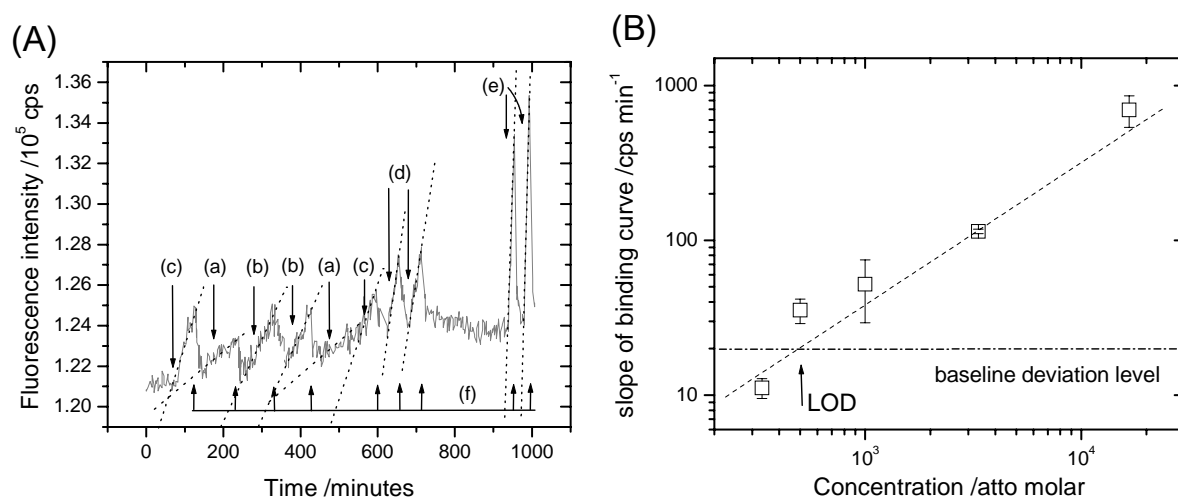


Figure 5.9: (A) Fluorescence intensity upon the injection of sample solutions with (a) 333 aM, (b) 500 aM, (c) 1 fM, (d) 3.3 fM, (e) 16.7 fM concentrations of AF-RaM. Regenerations (f) were performed after every sample injection to re-set the baseline level. Dashed lines are the linear fits to the binding curves to yield the corresponding binding slopes. (B) Double-logarithmic plot of the data from (A), as a dose-response curve. The dashed line is a linear fit. The dash-dotted line represents the baseline deviation level.

Mouse IgG was covalently loaded to the CMD matrix, with a SPR angle shift of ~ 1.5 degrees, corresponding to a surface density of ~ 8 ng mm^{-2} . The baseline stability was tested again by five times injection of mere buffer solution. Due to the increased background signal level, the baseline stability was deteriorated, to a level of ~ 20 cps/min. Then, as shown in Figure 5.9 (A), a series of AF-RaM solutions were tested sequentially, at a concentration range from 333 aM to 16.7 fM, followed by regeneration steps by applying an injection pulse of glycine buffer (10 mM, pH 1.7). The mass-transport limited binding signals from all the applied concentrations could be resolved from the baseline fluctuation, although the dose-response curve (Figure 5.9 (B)) intersects the

baseline deviation level and gives a LOD of ~ 500 aM. Combining the two dose-response curves in Figure 5.8 and Figure 5.9(B), one can see that the time-dependent fluorescence increase is a linear function of the injected AF-RaM concentration over 6 orders of magnitude!!

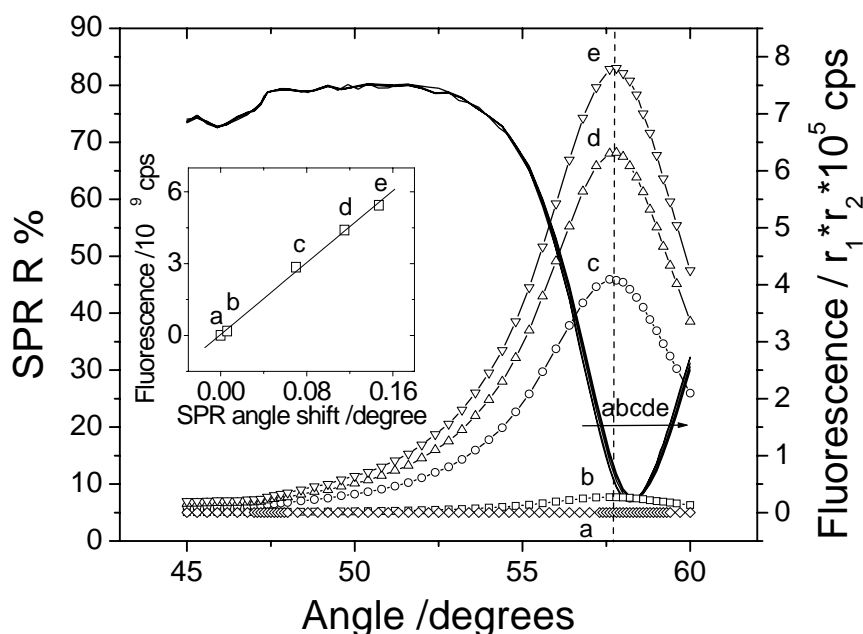


Figure 5.10: Angular scan curves of SPR and fluorescence, at paused stages (a, b, c, d, e) while applying a more concentrated AF-RaM solution (6.7 nM) on the same surface as the one used for the experiments presented in Figure 5.9. The shift of the SPR minimum angles, as well as the increases of the fluorescence signal can be resolved simultaneously. A linear dependence is shown for both signals (cf. the inset). Here, the fluorescence signal was greatly attenuated by applying a much weaker laser intensity (by a factor of $r_1=17$) and by using an attenuator (by a factor of $r_2=410$) for the fluorescence detector, considering the linear working range of the detector and photobleaching issues.

In an effort to establish the correlation between the SPR and the fluorescence signals in order to quantify the number of molecules involved in the binding at the LOD level, a 6.7 nM AF-RaM solution was injected into the flow cell and the binding repeatedly paused by temporarily filling the flow cell with HBS-EP buffer. 5 angular scans (a, b, c, d, e) were taken at each interval (plotted in Figure 5.10). It is worth noting that the dissociation rate of the couple of AF-RaM/Mouse IgG ($k_{off} \approx 6 \times 10^{-5} \text{ sec}^{-1}$) was slow enough to ensure a negligible loss of AF-RaM during the angular scans (which typically takes ~ 120 seconds). By plotting the SPR minimum angles versus the peak fluorescence intensities measured, one obtains the slope of $k = \sim 3.8 \times 10^{10} \text{ cps degree}^{-1}$ (inset of Figure 5.10), which corresponds to $\sim 0.5 \text{ molecule mm}^{-2} \text{ cps}^{-1}$ considering the aforementioned correlation $\Delta\theta/\sigma = 0.19 \text{ degree (ng mm}^{-2})^{-1}$. Therefore, the LOD (20 cps min^{-1}) corresponds to a flux of ~ 10 antibody molecules binding to the sensing area ($\sim 1 \text{ mm}^2$) per every

minute, which is approaching to a single-molecule sensing level. Also, the strictly linear dependence of k , between the SPR and the fluorescence signal, may indicate a nicely convoluted distance-dependence fluorescence profile by virtue of the 3D dextran matrix.

5.2.6 Parallel comparison to Biacore 3000

The LOD of the same antibody binding system was tested in a Biacore 3000 instrument, a high-end level label-free biosensor, for a parallel comparison. Although this commercial instrument is highly automatic, the loading of 2F9.1 on dextran surface was controlled manually, in order to reach a similar level for a direct comparison. The final level of loading was ~ 6800 RU, about 7 ngmm^{-2} (Figure 5.11(A)). Subsequently, a series of concentration, in the pico-molar range, were sequentially injected (5 minutes), rinsed (3 minutes) and regenerated (2 minutes, by glycine buffer). As shown in Figure 5.11 (B), the responses from the AF-RaM solution below 100 pM could hardly be resolved. Therefore, the LOD of Biacore instruments for such an interaction system is roughly in the sub-nanomolar range, which is consistent with the report from Biacore for IgG detection.¹⁰⁷ In conclusion, SPFS is by more than five orders of magnitude more sensitive than Biacore instruments, the best label-free biosensor in the market.

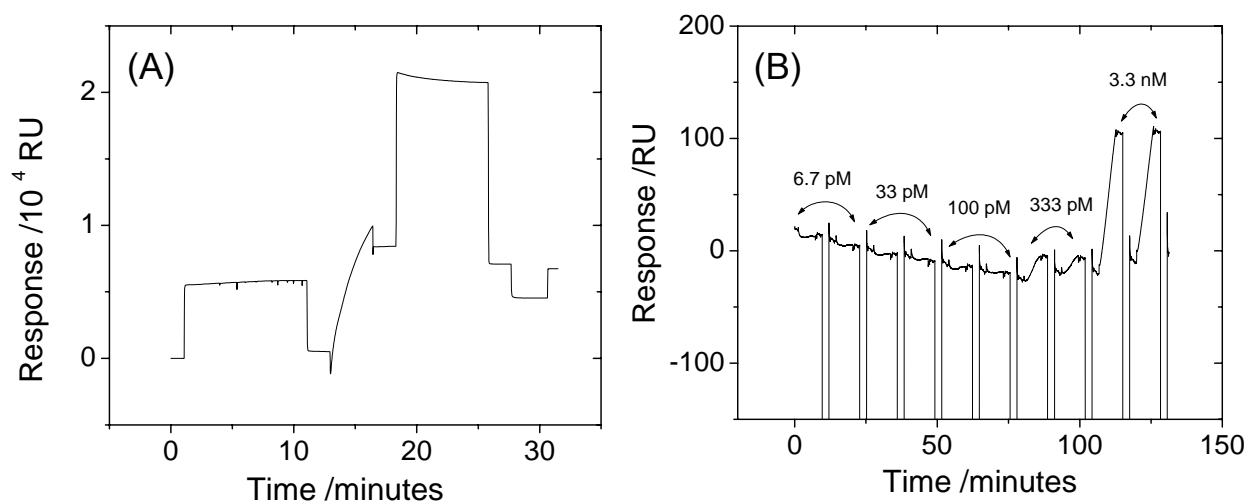


Figure 5.11: A direct comparison experiment using a Biacore 3000 instrument: (A) the loading of 2F9.1, (B) the sequential injections of AF-RaM antibody with increasing concentration series. Regeneration was performed in the intervals.

5.2.7 SPFS in other modes

As a highly modular set-up, SPFS can be upgraded to realize spectroscopic or microscopic detection. Since the optimization of the spectroscopic/microscopic module remains to be done, here only some rather preliminary sensitivity tests are provided.

5.2.7.1 SPFS+FOS

By attaching a fiber optic spectrometer (FOS, from ocean optics), SPFS becomes a real ‘spectrometer’. Being able to resolve spectroscopic information from the fluorescence emission, SPFS+FOS can achieve more delicate detection/characterization modes for, e.g., FRET studies or color multiplexing detections, etc.

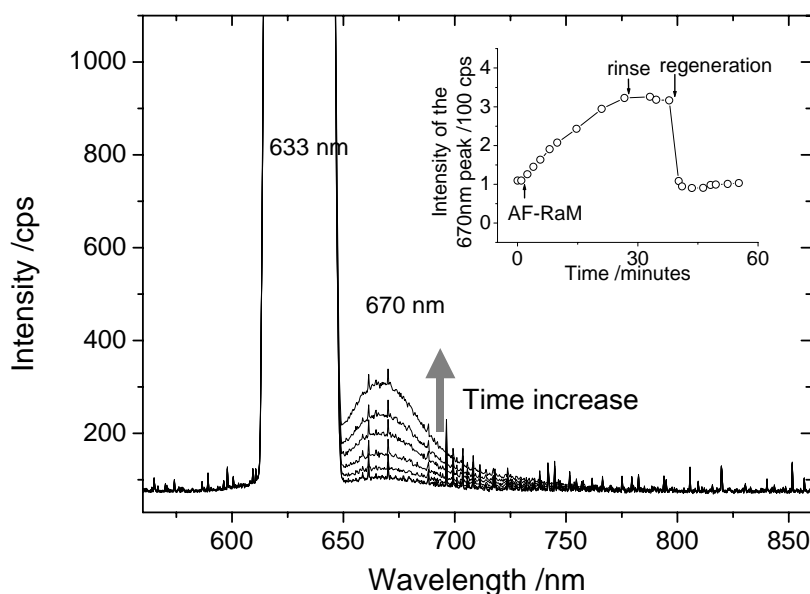


Figure 5.12: Spectra recorded upon the binding of 33 pM AF-RaM on the 2F9.1 surface. The inset shows the time-dependence of the 670 nm peak intensity upon the binding of a 33 pM AF-RaM solution, the buffer rinsing and finally the regeneration by glycine buffer. The integration time of the FOS is 300 msec, average = 2.

As shown in Figure 5.12, on a CM5 chip loaded with 2F9.1, the AF-RaM binding from picomolar solution was recorded as a series of spectra. Before introducing the AF-RaM solution, the spectra exhibited a single peak at ~ 633 nm, corresponding to the wavelength of the laser. This was clearly the elastically scattered laser light, with its intensity being related to the roughness of the surface. Upon the introducing of AF-RaM, another peak at ~ 670 nm emerged and its intensity increased continuously with time. The inset of Figure 5.12 plots the intensity at 670 nm versus the

time upon the injection of a 33 pM AF-RaM solution, the buffer rinsing and finally the regeneration. Such a test also demonstrates the sensitivity of SPFS+FOS was at least at the lower pico-molar concentration range, corresponding to several pico-gram per mm^2 using the previously established correlations.

5.2.7.2 SPFM

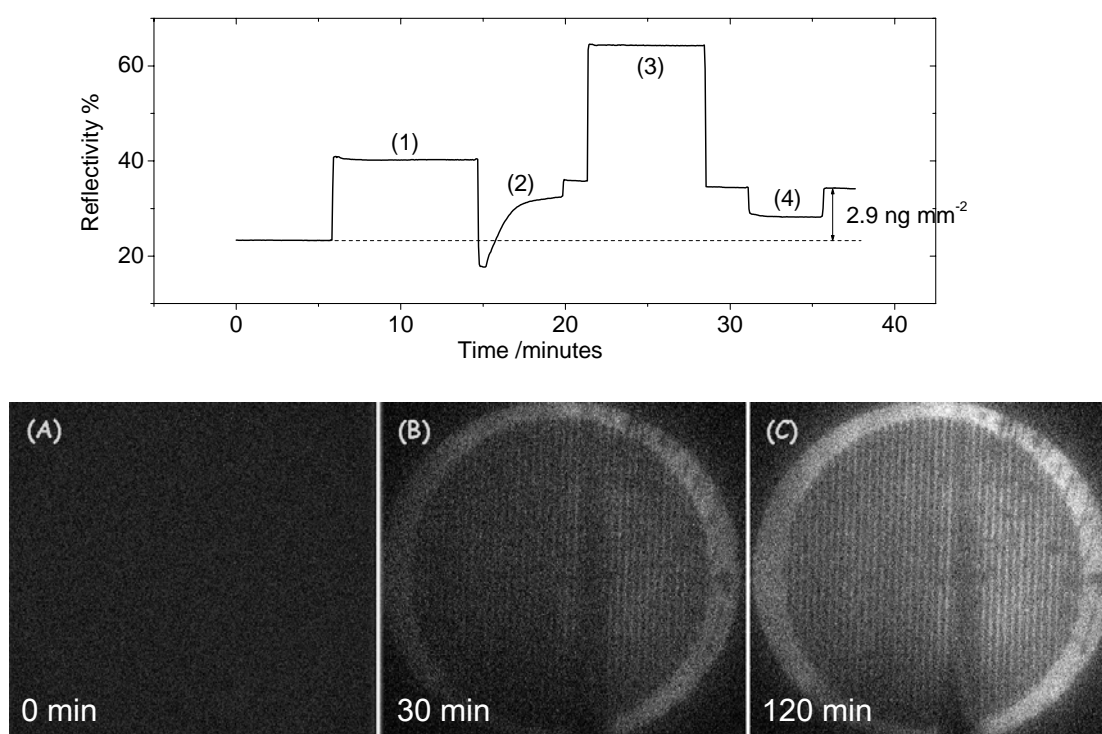


Figure 5.13: (Upper panel) Immobilization of 2F9.1 on dextran surface patterned by UV-lithography. Procedure (1), (2), (3) and (4) correspond to those in Figure 5.4. (Lower panel) SPFM images obtained before (A) and after (B)(C) the binding of 60 pM AF-RaM on the 2F9.1 derivatized dextran surface. The CCD camera were operating under $-30\text{ }^{\circ}\text{C}$, intergration time = 15 sec, bining = 2.

Surface plasmon fluorescence microscopy, or SPFM, has also been developed for spatially-resolved DNA sensing, which can directly meet the needs in reading DNA¹⁰⁸ or protein microarrays. It is also meaningful to demonstrate its sensitivity, based on the same dextran chip.

In order to generate the surface pattern, a dextran surface was illuminated by UV light (254 nm) through an SEM copper grid (pattern (A) in Figure 3.10) for 40 minutes. Due to the photo-oxidation mechanism, the area exposing to the UV light was oxidized and removed by rinsing with copious amount of water. The exposed bare Au was then passivated, by dipping the substrate into the EG thiol solution (500 μM in ethanol) for 10 minutes. The remaining dextran layer was then covalently loaded by a decent amount of 2F9.1, followed by the SPR response which was the

averaged response on the patterned surface (cf. Figure 5.13(A)). As a result, the averaged loading density of 2F9.1 was $\sim 2.9 \text{ ng mm}^{-2}$. The value was $\sim 41\%$ of the density obtained on un-patterned matrix ($\sim 7 \text{ ng mm}^{-2}$, cf. Figure 5.4), which is nicely in agreement with the areal ratio $\rho=39\%$ of pattern (A) in Figure 3.10. As expected, the patterned dextran layer showed no feature under a CCD camera with a wavelength acceptance of $670 \pm 5 \text{ nm}$. (cf. (A) in Figure 5.13). Upon the introducing of a 60 pM AF-RaM solution, the fluorescence pattern gradually became visible within 30 minutes (cf. (B)) and the contrast kept enhancing up to 120 minutes (cf. (C)). It strongly demonstrates (1) a successful generation of the surface heterogeneity by the UV-lithographic strategy, and (2) the at least pico-molar sensitivity of SPFM.

5.3 SPFS PSA assay

The prostate-specific antigen (PSA) is a 32- to 33- kDa single-chain glycoprotein (by Lilja, et al.¹⁰⁹), which has been characterized as a serine protease with restricted chymotrypsin-like specificity belonging to the human kallikrein gene family. The protein is secreted by the epithelial cells of the prostate and levels increase in patients with prostate cancer (PCa). Recent work has confirmed the existence of two predominate molecular isoforms of PSA, i.e., free- and complexed-PSA (c- and f-PSA).¹¹⁰ PSA complexes many proteins, however, the complex with the $\alpha 1$ -antichymotrypsin (ACT) is predominant and mostly immunologically detected. Immunoassays measuring serum PSA concentrations have been used as screening tests or to facilitate clinical management of PCa. Especially, it became possible to sensitively measure total PSA (t-PSA), PSA-ACT and f-PSA level, and calculate PSA-ACT/t-PSA, f-PSA/t-PSA, or f-PSA/PSA-ACT ratios.^{110, 111} This greatly enhances the predictive value of PSA measurement for early diagnosis of PCa, excluding from, e.g. benign prostate hyperplasia (BPH) which shows higher f-PSA portion than PCa.¹¹²

Currently, the clinically available PSA assays are mostly based on enzyme-linked immunosorbent assays (ELISA), while fluorescent (e.g. time-resolved fluorometric immunoassay), chemiluminescent labels are also used for achieving higher sensitivities. Because of the importance in the detection of PCa, PSA assay has been frequently tested for the proof of concept when brand-new sensing technique was developed, such as nanoparticle-based bio-bar-code, microcantilever, surface-enhanced Raman scattering, etc. As an effort towards the direct detection of PSA, label-free PSA detections have been also reported using surface plasmon resonance, microcantilever, QCM, electrochemistry, etc.

Since SPFS has shown extraordinary sensitivity in tracing a few molecules, it is highly demanding to test its ability in detecting some clinically relevant samples. Therefore, in the following, we will introduce an SPFS-based sandwich immunoassay for f-PSA, utilizing an antibody couple from a commercial source.

5.3.1 Experimental

Prostate-specific antigen (PSA, $\geq 95\%$ pure from human seminal fluid, Mw. = 30 kD) and an antibody couple against PSA are obtained from Biosite (Täby, Sweden). The capture antibody and the detection antibody are named M37230M and M86506M, respectively. M37230M is a monoclonal antibody (mouse IgG1) recognizing a hidden epitope specific for free PSA. M86506M is a monoclonal antibody (mouse IgG2a) specific for epitope 6 in total PSA determination. Human plasma (from female) and free CM-dextran are obtained from Biacore.

For the SPFS PSA assay, we used a sandwich assay format, which is an analogue of the widely applied ELISA technique. PSA was bound first by the immobilized capture antibody (M37230M), and then a fluorescently labeled detection antibody (M86506M) bound to the captured PSA, forming a capture/PSA/detection protein ‘sandwich’ (schematically described in Figure 5.1 (C)). PSA concentration was measured indirectly by measuring the fluorescence intensity of bound fluorophores attached to the detection antibody.

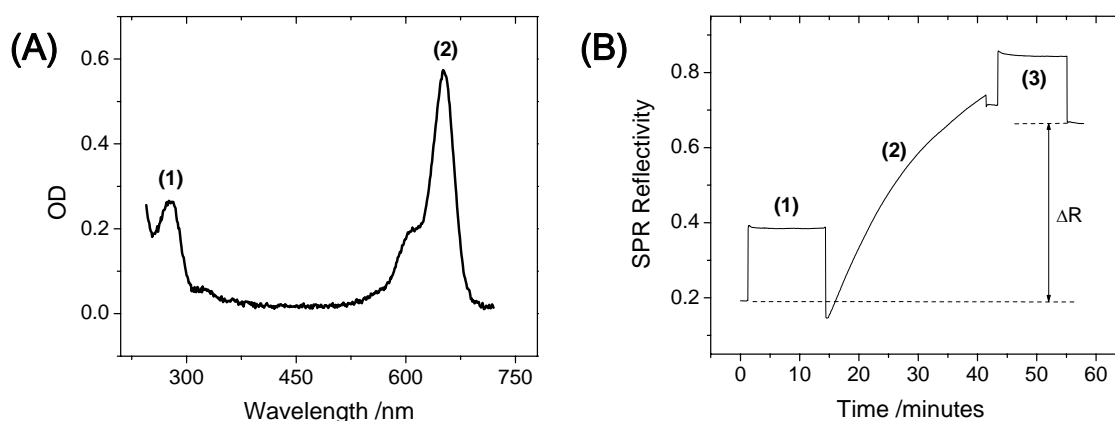


Figure 5.14: (A) UV-VIS spectrum of the Alexa Fluor 647 labeled detection antibody - LM86506M. Peak (1), (2) corresponds to the protein adsorption wavelength (280 nm) and the AF 647 adsorption wavelength (647 nm), respectively. (B) The covalent immobilization of the capture antibody M37230M to the dextran matrix. (1), (2), (3) represents the EDC/NHS activation, antibody immobilization (30 $\mu\text{g}/\text{mL}$), EA deactivation, respectively.

M86506M was fluorescently labeled using a commercial Alexa Fluor 647 labeling kit. The dye-to-protein molar ratio (D/P), e.g., the labeling efficiency was determined spectroscopically by an UV-Vis spectrometer. The spectrum is shown in Figure 5.14 (A), which yielded $D/P = 2$. An antibody recovery of $>95\%$ was achieved after the labeling process. Labeled M86506M will be abbreviated as LM86506M.

The capture antibody, M37230M, was covalently immobilized to the dextran matrix on a CM5 chip using the amine-coupling protocol. The immobilization procedures are recorded by the SPR kinetic mode and shown in Figure 5.14 (B). A final loading level ΔR of M37230M was typically 8 ng mm^{-2} . This value compares favorably to, e.g., a typical coating level of capture antibody of $\sim 1.5 \text{ ng mm}^{-2}$ physically adsorbed on a polystyrene well for ELISA detection, and can be directly translated into a sensitivity enhancement.

The sandwich assay with the PSA sample was performed in HBS buffer and in female serum, respectively. A flow rate of 3 mL/min was used in all SPFS measurements.

5.3.2 Affinity determination

As schematically drawn in Figure 5.15 (A), we deal with two dynamic equilibria, i.e. k_{on1}/k_{off1} and k_{on2}/k_{off2} , existing in the format of sandwich assay. Since the PSA and the detection antibody were sequentially introduced into the flow cell, the binding of the detection antibody was accompanied by the dissociation of PSA from the capture antibody. In other words, the detection antibody was binding to a surface with the number of binding sites (i.e. PSA) constantly decreasing. This is a general remark for all the sandwich immunoassays, although nothing needs to be worried if following a standardized assay protocol and/or using high affinity antibodies. Here, as a prerequisite to design the assay protocol, the affinity picture of Figure 5.15 (A) was learned firstly.

In order to quantify the affinity between the capture antibody and the PSA, their interaction was measured by SPR in a label-free way. Approximately, 1.8 ng mm^{-2} M37230M antibody was loaded on the dextran surface by controlling the time of step (3) in Figure 5.15 (B). This amount of M37230M was designed to be low, in order to minimize the mass-transport effect for a correct affinity determination. (cf. 2.4.5) The interaction with a $1 \text{ }\mu\text{M}$ PSA solution is shown in the inset of Figure 5.15 (B). By a nonlinear fitting to pseudo-single-exponential models, k_{on1} , k_{off1} , K_{A1} were calculated to be $2.2 \times 10^4 \text{ M}^{-1}\text{sec}^{-1}$, $3.2 \times 10^{-4} \text{ sec}^{-1}$, $6.9 \times 10^7 \text{ M}^{-1}$, respectively. As a test closer to the experimental condition (i.e. high M37230M density and low PSA concentration), another SPR study was conducted between 200 nM PSA and a 8 ng mm^{-2} M37230M antibody surface (cf. curve (1) in Figure 5.15 (B)). A clear kinetic discrepancy is presented by plotting a simulation

curve using the kinetic constants (k_{on1} , k_{off1}) obtained in a ‘correct’ way (cf. curve (2) in Figure 5.15 (B)), which indicated a significant deviation from pseudo-single-exponential binding in the experimental condition by mass-transport/rebinding effects. Due to the bi-exponential characteristic, it was mathematically difficult to quantify k_{off1} .

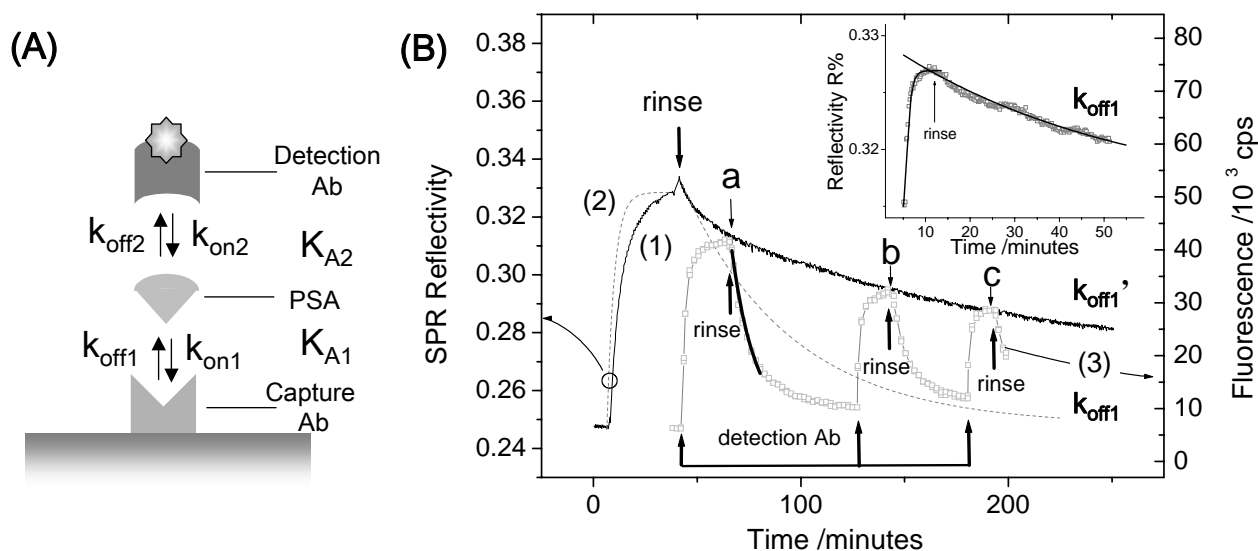


Figure 5.15: (A) Schematic illustration of two dynamic equilibria existing in the sandwich assay format. (B) Experimental efforts to learn the affinity picture: (1) SPR study of the association/dissociation of 200 nM PSA on a high density M37230M surface (8 ng mm^{-2}). (2) Simulated curve with k_{on1} , k_{off1} without the influence from mass-transport effect. The k_{on1} , k_{off1} was obtained by an interaction study between $1 \mu\text{M}$ PSA and a low-density M37230M surface (1.8 ng mm^{-2}), as shown in the inset. (3) A sequential association/dissociation of a 24 nM LM86506M solution on a high density M37230M surface (8 ng mm^{-2}) pre-incubated with 5 pM PSA for 30 minutes, studied by the fluorescence signal channel. The background fluorescence was subtracted.

The subsequent association/dissociation of the detection antibody was superimposed to the dissociation ($k_{off'}$) of PSA. To show that, a series of capture antibody (LM86506M) solutions were sequentially injected and rinsed on an M37230M surface (density = $\sim 8 \text{ ng mm}^{-2}$) pre-incubated with a 5 pM PSA solution for 30 minutes (cf. curve (3) in Figure 5.15 (B)). Several interesting points emerged in aligning curve (3) with curve (1). Firstly, the association of capture antibody reached an ‘apparent’ equilibrium in 20-25 minutes, however, at a time ‘a’ where $\sim 18\%$ PSA already dissociated from the surface, indicating a signal underestimation. However, if following the dissociation trail of curve (2), then $\sim 34\%$ PSA will be lost at time ‘a’, which indicates a benefit from the mass-transport limited dissociation of PSA provided by high density M37230M in curve (1). Secondly, the dissociation of LM86506M was visually much faster than that of the PSA. This ‘apparent’ dissociation k_{offa} was a result of two dissociation processes, i.e., k_{off1} (or more accurately, k_{off1}') and k_{off2} and could be expressed as,

$$k_{offa} = k_{off1}' + k_{off2}$$

--- 5.3

A single-exponential fit yielded $k_{offa} = 1.4 \times 10^{-3} \text{ sec}^{-1}$, which was over one order-of-magnitude larger than k_{off1} (which was significantly larger than k_{off1}'). Therefore, we can conclude that $k_{off2} \gg k_{off1}'$, preliminarily meaning that $K_{A2} \ll K_{A1}$. Thirdly, due to slower desorption of PSA, the remaining PSA could be repetitively decorated by the LM86506M. Interestingly, the equilibrium levels of these decoration steps matched the dissociation trail of PSA provided by SPR (cf. curve (1)) at time 'a', 'b', 'c', respectively. This suggests that the whole process of curve (3) was considered as a pure 'rinsing' process to PSA, with little disturbance from the LM86506M association/dissociation.

5.3.3 Sandwich PSA assays

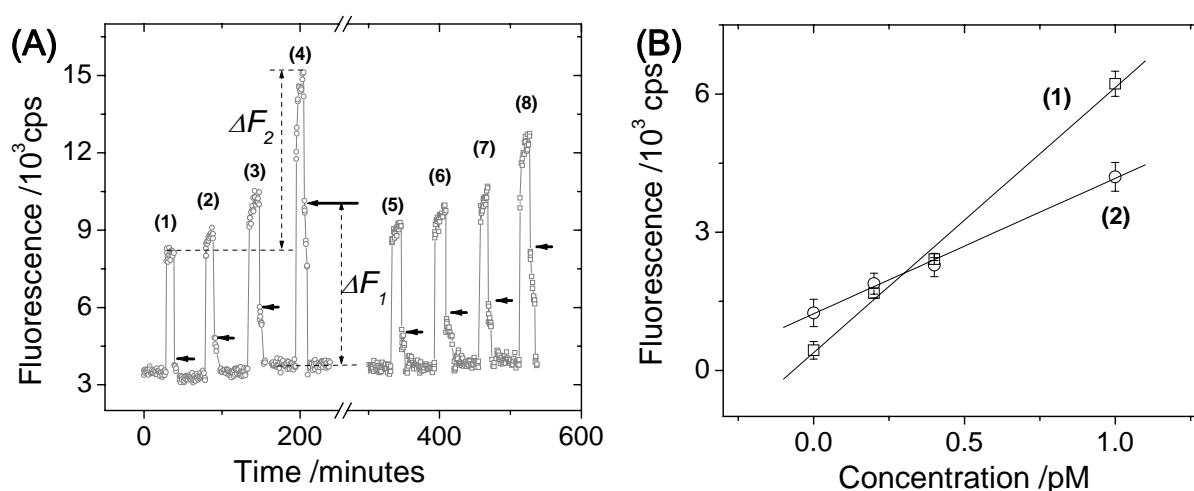


Figure 5.16: Demonstration of an SPFS based sandwich f-PSA immunoassay in both buffer and human plasma. (A) Kinetic fluorescence working curves acquired by the injection of 12 nM LM86506M after the surface treated for 30 minutes with various PSA concentrations of (1) 0 fM, (2) 200 fM, (3) 400 fM, (4) 1 pM in HBS buffer; and of (5) 0 fM, (6) 200 fM, (7) 400 fM, (8) 1 pM in female plasma. (B) Dose-response curves constructed by ΔF_1 signals in (A) obtained in buffer (curve (1)) and female plasma (curve (2)).

For every experimental injection, 500 μL PSA samples with desired concentration were prepared in HBS buffer or in female plasma from a 10 μM stock solution (in HBS buffer). For preparing the samples in plasma, a fixed HBS/plasma ratio of 1:9 was used. The sample with a concentration between 200 fM to 1 pM was injected into the flow cell and circulated in the loop for 30 minutes. Then, after a brief wash of < 1 minute by pure HBS buffer, 12 nM LM86506M solution prepared in HBS buffer was injected and circulated in the flow cell for 10 minutes. Finally, the LM86506M solution was rinsed away by HBS buffer for < 5 minutes, and the surface

was regenerated using a glycine buffer (10 mM, pH 1.7). A typical working curve is shown in Figure 5.16 (A), presented by the measured fluorescence signal. Two alternative ways could be used to acquire the fluorescence signal increase, ΔF , for plotting the dose-response curves: (1) ΔF_1 is the difference between the baseline and the first data point after the LM86506M solution was rinsed away; (2) ΔF_2 is the difference between the equilibrium levels from the negative sample and the PSA sample (cf. Figure 5.16 (A)). From a practical sensing point of view, getting ΔF_2 is faster, since the step of solution removal and buffer replacement is unnecessary. However, it requires very consistent preparations of the LM86506M concentration since ΔF_2 subtracts the equilibrium signal as a fixed background signal (cf. (1) in Figure 5.16 (A)). Therefore, for pursuing the limit of detection, ΔF_1 was the choice. Although due to the fast dissociation rate of LM86506M from the surface, using ΔF_1 could slightly underestimate the signal.

For the negative test with pure buffer (cf. step (1) in Figure 5.16 (A)), by injecting the fluorescently labeled detection antibody, there was an abrupt background jump but the signal almost completely leveled back to the baseline signal upon rinsing with pure buffer, giving a typical $\Delta F_1 = 200$ cps in the noise level. It suggested that there was no detectable non-specific binding (NSB) between the dextran matrix and LM86506M, as well as between M37230M and LM86506M. The fluorescence background signal is usually seen in analyzing fluorescence samples (cf.4.3), which is the contribution from the bulk fluorescent molecules excited by the tail of the SPR evanescent field and the surface-scattered light, therefore scales linearly to the sample concentration. For the surface incubated with the positive samples containing PSA ranging from 200 fM to 1 pM, the injection of LM86506M solution not only induced the initial background jump, but a subsequent signal climbing, which reached equilibrium in 10-20 minutes. Exchanging the LM86506M solution by the HBS buffer abruptly leveled down the signal, however, at a higher level than the baseline, indicating a certain amount of bound LM86506M in recognizing the bound PSA and forming the immuno-triplex.

For the experiments in plasma, there were two new features found. Firstly, for the negative sample, i.e., mere female plasma, a significantly higher NSB signal, e.g., $\Delta F_1=1500$ cps was shown (cf. step (5) in Figure 5.16 (A)). This probably arose from a certain amount of sticky substances in the plasma, which interacted with the dextran matrix and/or the detection antibody. Secondly, for all the samples in the human plasma, the signal ΔF_1 were significantly less than the corresponding concentrations in HBS, reflecting a decreased binding efficiency of PSA. Consequently, comparing the dose-responses curves in buffer and in plasma (cf. Figure 5.16 (B)), the later shows a deteriorated initial level and a smaller slope, which represents a poorer

sensitivity. We inferred that it could be due to the different diffusion behaviors of PSA in buffer and in human plasma, respectively.

5.3.4 Binding in buffer and human plasma

The capture of PSA by M37230M in the experimental condition was an interaction between extremely diluted analyte (named as A) and high-density catcher molecule on the surface (named as B), which was firmly under mass-transport control. Under such a condition, the surface concentration of the AB complex, i.e. $[AB]$, formed in unit time Δt is proportional to the diffusion constant k_M and analyte concentration $[A]$, which can be expressed by the following equation derived from Equation 2.54 and 2.55:

$$[AB] \propto k_M [A] \Delta t \propto \left(\frac{D}{h}\right)^{2/3} \left(\frac{v}{bx}\right)^{1/3} [A] \Delta t \quad \text{--- 5.4}$$

where D , the diffusion coefficient, is inversely proportional to the viscosity η of the sample medium, according to the Stokes-Einstein equation:¹¹³

$$D = \frac{kT}{6\pi\eta a} \quad \text{--- 5.5}$$

where k is the Boltzmann constant, T is the temperature, a is the radius of the analyte. In summarizing Equation 5.4 and 5.5, the relation between the slope of the dose-response curve $S = [AB]/[A]$ and the viscosity η is:

$$S = \frac{[AB]}{[A]} \propto k_M \propto \eta^{-2/3} \quad \text{--- 5.6}$$

Note that this is based on the assumption that the nonspecific contribution, e.g., from the plasma, is constant for all studied PSA concentrations. From Equation 5.6, one can conclude that a higher medium viscosity leads to a slower binding rate in that medium.

The slope of the dose-response curves (1) and (2) were 5756 cps/pM and 2940 cps/pM, respectively. This gave a slope ratio of $S_1/S_2 = \sim 1.96$. From a textbook, we get the water viscosity $\eta_1 = 0.89$ mPa.s at room temperature.¹¹⁴ A typical plasma has a viscosity of $\eta_2 = 1.39 \pm 0.08$ mPa.s,¹¹⁵ however, slightly lowered here due to the mixing with buffer for the sample preparations (cf. before). Using these theoretical values, $(\eta_1/\eta_2)^{-2/3}$ was approximately 1.35, considerably smaller than the ratio of the S_1/S_2 . Therefore, the medium viscosity cannot completely explain the retarded PSA binding rate in the plasma. Although we have no clear evidence yet, but the dense macro-substances in the plasma could also shield the PSA-antibody recognition, which consequently reduce the effective PSA amount. As an extension of this

speculation, we infer that a fraction of f-PSA could be converted to c-PSA by binding to, e.g., protease inhibitor α 2-macroglobulin (AMG), ACT, the pregnancy zone protein and the protein C inhibitor (PCI), which probably still existed in female plasma. Consequently, the complexed PSA (c-PSA) will not be recognized by M37230M, which is only specific for f-PSA.

5.3.5 Removal of plasma NSB and LOD evaluation

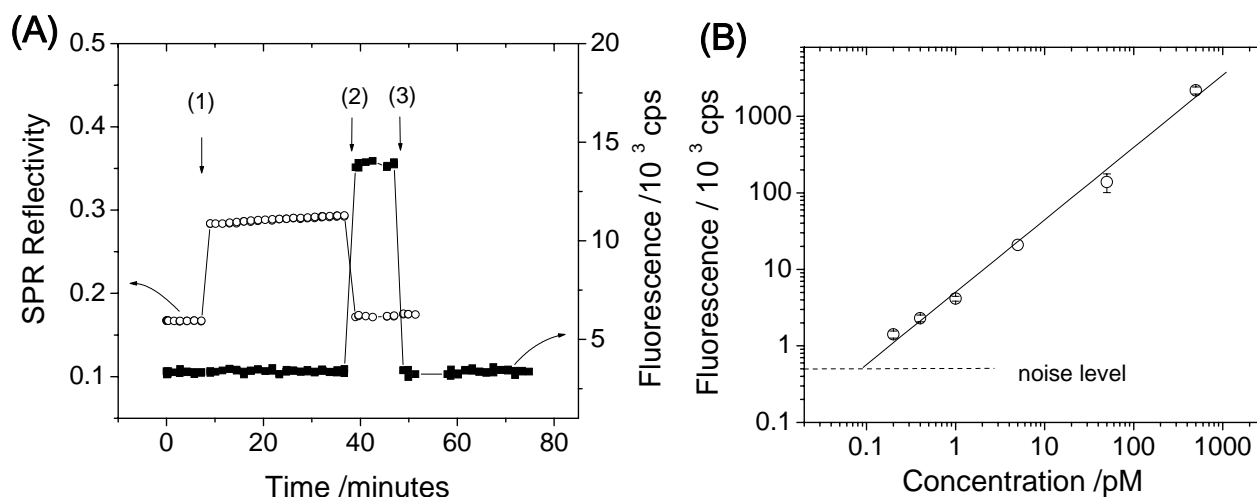


Figure 5.17: (A) Demonstration of the success removal of plasma NSB by adding 0.5 mg/mL free CMD in the sample. See text for detail. (B) Dose-response curve of the PSA assay in plasma with CMD.

In an effort to eliminate the NSB from plasma, free carboxymethyl-dextran (CMD) was added to the sample. As demonstrated by Figure 5.17 (A), the dextran surface derivatized by M37230M was exposed to a 9:1 plasma/HBS solution containing 0.5 mg/mL CMD for ~30 minutes (cf. (1)->(2)). After a brief rinse with HBS buffer, the flow cell was filled with a 24 nM LM86506M solution for ~10 minute (cf. (2)->(3)). Upon the backfilling with buffer (cf. (3)), the fluorescence signal was completely recovered back to the baseline level, indicating a complete removal of plasma NSB by free CMD. One of the possible explanations is, that the free CMD molecules competitively bound to the substances that were responsible to the NSB signal and carry most of them away by the buffer rinsing.

The LOD of the SPFS PSA assay in plasma was therefore evaluated with the aid of CMD. A linear dose-response curve ranging from 200 fM to 500 pM of PSA was plotted in Figure 5.17 (B). In theory, such a linear correlation between the ‘dose’ and the ‘response’ preserves as long as the PSA is persistently under mass-transport control during the interaction time. Since the signal from the negative control sample was virtually un-detectable by adding free CMD, the LOD was

defined as three times SD of the baseline signal fluctuation (cf. the dashed line in Figure 5.17(B)). The linear extrapolation of the dose-response curve intersects the LOD at ~ 80 fM of PSA, corresponds to ~ 2 pg/mL of PSA. This LOD was achieved in 40 minutes under room temperature. Apparently, it could be easily improved by, e.g., increasing the contact time, working temperature or flow rate of the PSA sample, due to the mass-transport limited nature of the interaction between PSA/M37230M. This LOD was significantly better than that of an assay based on ELISA (e.g. LOD = 3.3 pM¹¹⁶), microfluorometric assay (e.g. LOD = 14 pM¹¹⁷) and nanomechanics (e.g. LOD = 6 pM⁹⁸), etc. It is close to the PSA detection based on SERS and immunogold labels (LOD = 40 fM).¹¹⁸ However, it was still an order of magnitude lower than some ultra sensitive detection schemes, e.g., the time-resolved fluorometric immunoassay based on rare earth labels.¹¹⁹ No doubt, all the methods fulfill the clinical requirement, where the t-PSA concentration < 120 pM in the body is considered to be 'safe'. However, the low level detection of PSA could still be greatly beneficial in the identification of PCa relapse or in breast cancer screening and diagnosis.

5.4 Conclusion

Using the three-dimensional functional dextran matrix of the CM5 sensor chip of Biacore, the substrate (Au metal) induced fluorescence loss of bound fluorophores monitored in SPFS can be greatly reduced. Moreover, the distance-dependent fluorescence of the fluorophores located at different positions relative to the metal surface is convoluted to result in a coverage-independent fluorescence yield. (cf. Figure 5.10) This is then optimized for the LOD assessment of SPFS. The first model system employed is a direct binding assay with mouse IgG covalently immobilized to the carboxymethyl dextran matrix of the CM5 sensor chip. Time-resolved detection of fluorophore (AF 647) labeled rabbit anti-mouse antibody down to 500 aM (10^{-18} M) was accomplished, corresponding to a binding rate of ~ 10 molecules mm^{-2} minute^{-1} . A sandwich assay of f-PSA by SPFS is subsequently presented as a clinically relevant system. Even with the presence of human plasma, SPFS was capable to detect f-PSA in pico-gram range within 40 minutes, which fulfills clinical requirements in large abundance. The results of this chapter strongly support that SPFS technique is among the most sensitive techniques for biosensing.

6 Surface plasmon diffraction

6.1 Background

A number of biosensors have been reported involving the diffraction detection concept. They cover an analyte spectrum ranging from organic compounds¹²⁰ to proteins¹²¹ or even whole cells¹²². However, all of those reported strategies were based on conventional diffraction configurations in a transmission or reflection mode using plane waves, i.e., normal photons. The transmission mode suggests adsorbing materials to boost the diffraction signal,^{120(B)} which is not applicable for label-free biosensing applications. A very recent progress is, with the aid of Au nano-particle label, DNA detection was possible on chemoresponsive diffraction gratings incorporating a multicolor detection scheme.¹²³ The reflection mode was mostly found in biological sensing assays based on surface diffraction. For example, by Goh's group,^{121(C)} a protein sensor was reported based on a TIR geometry, realizing a quantitative measurement of the biomolecular interaction in-situ and in real-time. However, due to the insufficient sensitivity, secondary antibodies conjugated with gold nano-particles were also applied to amplify the signal. Consequently, they yielded a linear dose-response curve covering a range from 0.17 to 3.4 nM of IgG analyte.

As early as 1987, our group has proposed that the diffraction efficiency can be greatly amplified by surface-plasmon enhancement.¹⁷ Note, that this has to be differentiated from the extensively studied approaches in which metallic gratings are used to enhance the momentum of a far-field light for SPR coupling.^{10,124} In our approach, the light was coupled into surface-plasmon modes through a prism, and a dielectric grating fabricated on the planar metal surface was to diffract the non-radiative PSP field into the light radiation (cf. Figure 6.1). The grating structure with a periodicity Λ provides an additional multiple of a small momentum g with $|g|=2\pi/\Lambda$ and delocalizes the surface-plasmon field, giving rise to a typical diffraction phenomenon. The periodicity Λ is chosen to be much larger than the light wavelength, concerning that the surface-bound electromagnetic modes can exist only in a narrow range of (ω, k) given by their dispersion behaviour, i.e., any scattering (or diffraction) will be an efficient process only if the final state is

within the density of states accessible to surface plasmons. Therefore, one can add only a small g as ' Δk ' in order not to (try to) scatter the plasmon into a range in which it can not exist, i.e., outside the angular (or momentum) range given by the width of the reflectivity curve. As a comparison to the conventional diffraction schemes, the diffraction efficiency was reported to be 6 times higher than that in the normal TIR configuration with the aid of the SPR enhancement, even in the case of poor SPR coupling ($R > 0.35$).^{17(A)} The gain in diffraction efficiency represents a sensitivity enhancement for sensing applications.

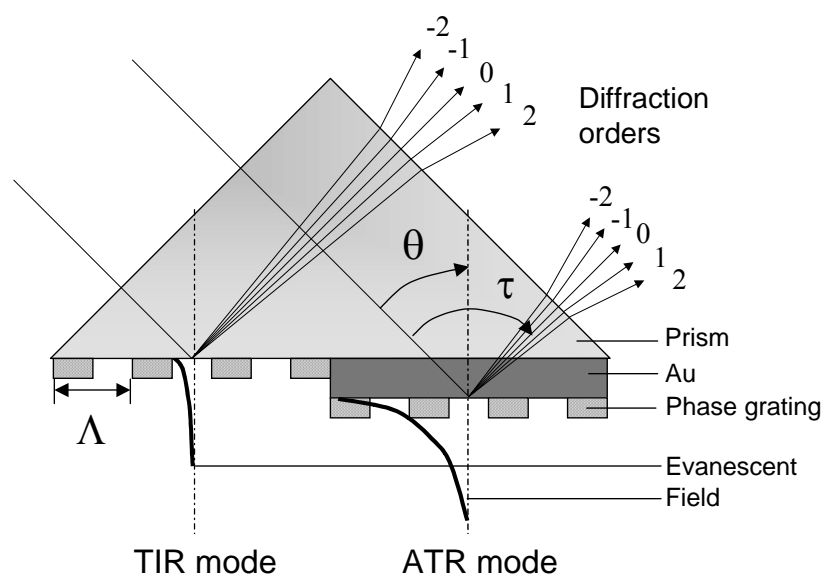


Figure 6.1: Schematic drawing of two types of diffraction sensors based on TIR and ATR modes, respectively.

The application of SPP-enhanced diffraction phenomena in biological sensing involves the use of micro-patterning technique, e.g., micro-contact print (μ CP) or photolithography, to generate a surface grating structure composed of functional and non-functional areas. Generally, receptor molecules are immobilized on the functional area, which is for simplicity a pattern of repeating parallel lines within which functionalized and non-functionalized lines alternate. This pattern is identical to a shallow surface grating, which yields a diffraction pattern consisting of a row of spots. The grating amplitude subsequently modulated by the association/dissociation events of the analyte to the receptor molecules is monitored by recording the variation in the diffraction intensity (or diffraction efficiency).

6.2 Diffraction enhancement by surface plasmon fields

In addition to the previous study¹⁷ the surface plasmon enhancement of the diffraction intensity was demonstrated. UV-illumination through copper grid masks was used to generate patterns on spin-coated polystyrene (PS) layer on Au and glass surfaces. (cf. 3.4.3) Consequently, well-defined PS patterns can be clearly seen in SPM images or depicted by surface profiler (cf. Figure 6.2). Note that SPM could resolve features with a size of $8\ \mu\text{m}$ from the hexagonal pattern [D]. These PS patterns induced visually striking diffraction patterns (cf. Figure 6.3), in agreement with their corresponding 2D Fourier transformation results. Cross-sectional analysis by the surface profiler showed that the amplitude of the patterned PS layers are $\sim 10\ \text{nm}$ on a Au surface and $\sim 13\ \text{nm}$ on the glass surface, respectively. This slight difference in thickness was within the experimental error.

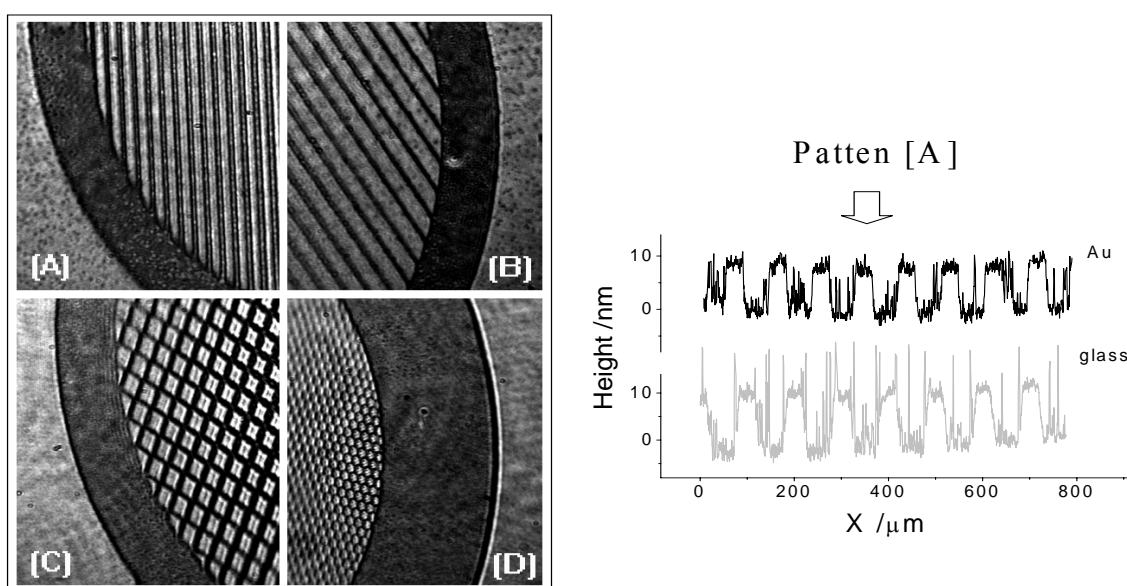


Figure 6.2: (Left) the SPM images for PS patterns on Au surfaces. The dimensions of their corresponding copper grids were described in the experimental chapter. (Right) the cross-sectional analysis of PS patterns (from [A]) on Au and glass.

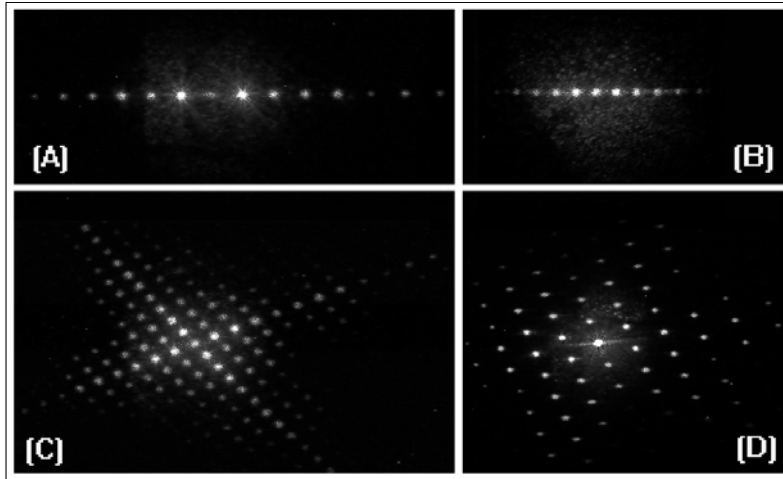


Figure 6.3: Optical photographs of the diffraction patterns generated by various PS patterns on Au surfaces, corresponding to Figure 6.2.

As shown in Figure 6.4, positioning the laser incident angle at the resonance angle θ_R , a series of diffraction peaks could be recorded in the vicinity of the reflected laser beam (zeroth diffraction order) in a nearly symmetrical distribution. The intensities of these orders were significantly higher than the diffraction by the PS pattern on the glass surface (i.e. a TIR configuration), although the grating amplitudes of both PS patterns were close (cf. Figure 6.2).

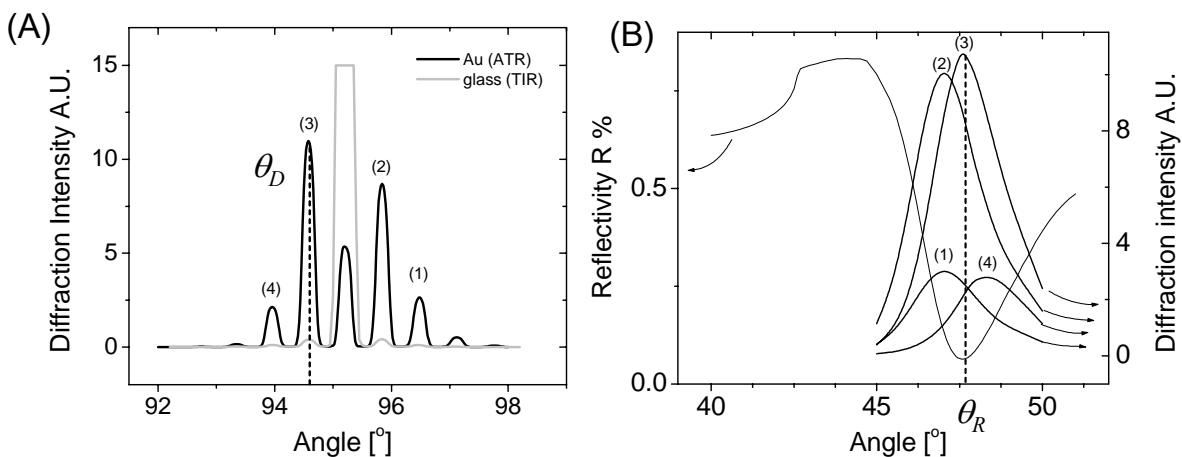


Figure 6.4: (A) The diffraction signals obtained from PS patterns on Au and glass surfaces, respectively. For the surface plasmon diffraction on Au and TIR diffraction on glass, the laser incident angle was both set at the angle θ_R shown in (B). (B) The angular dependence of the SPR reflectivity and the diffraction intensity of the +2nd (1), +1st (2), -1st (3) and -2nd (4) diffraction orders, shown in (A). One can see an obvious dispersion between the angles of diffraction maxima and the angle of SPR minimum.

An enhancement factor of ~18-20 was obtained by comparing the corresponding diffraction orders obtained from ATR and TIR configurations respectively, e.g., at θ_D in Figure 6.4(A), which was in quantitative agreement with the theoretical prediction (cf.2.1.6). Figure 6.4(B) shows that the intensity of the -2nd, -1st, +1st, +2nd diffraction orders were strongly dependent on the laser incident angle, i.e., the PSP coupling efficiency, which demonstrated the surface plasmon field-enhancement for the diffraction efficiency (referring to the intensity of the incident laser). The dispersion of the angular maxima of different diffraction orders is related to a sequential opening and closing of the surface plasmon decay channel via the corresponding diffraction orders.¹²⁵ More theoretical effort is needed to look inside this phenomenon. However, for this study, the biological applications of this novel concept will be emphasized as the major part.

6.3 Theoretical description

Like the TIR diffraction mode, the ATR-based diffraction mode also allows for the observation of holographic information stored in the region of the interfacial evanescent optical field. The localized PSP wave can be diffracted by gaining (or losing) discrete momenta $m \cdot g$, which is generated by the periodic surface structure of periodicity Λ . The diffraction angle deviates in discrete increments from the specular-reflection angle (i.e., zeroth-order diffraction) in fulfillment of the corresponding momentum-match condition:

$$k_{diff}^m = k_{PSP} \pm mg \quad \text{--- 6.1}$$

where k_{diff}^m is the wavevector of the m th diffraction order, k_{PSP} is the wavevector the PSP wave, g is the grating constant with $|g|=2\pi/\Lambda$ and m is the diffraction order. In general, for a shallow sinusoidal grating composed of non-absorbing materials, the diffraction intensity I_d can be approximated by the following expression:¹²

$$I_d \propto I_0 \left(\frac{\pi \Delta nd}{\lambda} \right)^2 \quad \text{--- 6.2}$$

where I_0 and λ are the intensity and wavelength of the source field respectively, Δnd represents the grating amplitude in an optical thickness format. This equation conveys two important messages: 1. The diffraction intensity I_d is proportional to the intensity of the excitation source –

the evanescent field, which emphasizes the importance of the surface plasmon field enhancement.

2. I_d is proportional to the square of the grating amplitude Δnd . For a small optical contrast variation ∂nd on the initial contrast Δnd ,

$$\frac{\partial I_d}{\partial nd} \propto \Delta nd \quad \text{--- 6.3}$$

This implies that the diffraction signal modulated by a unit amount of optical contrast variation ∂nd increases linearly with the level of initial contrast Δnd . Therefore, in principle, a larger sensitivity can be achieved on the basis of a ‘thicker’ matrix defining the functional regions. In addition to that, having some initial contrast helps to locate the diffraction orders for intensity recording in real-time.

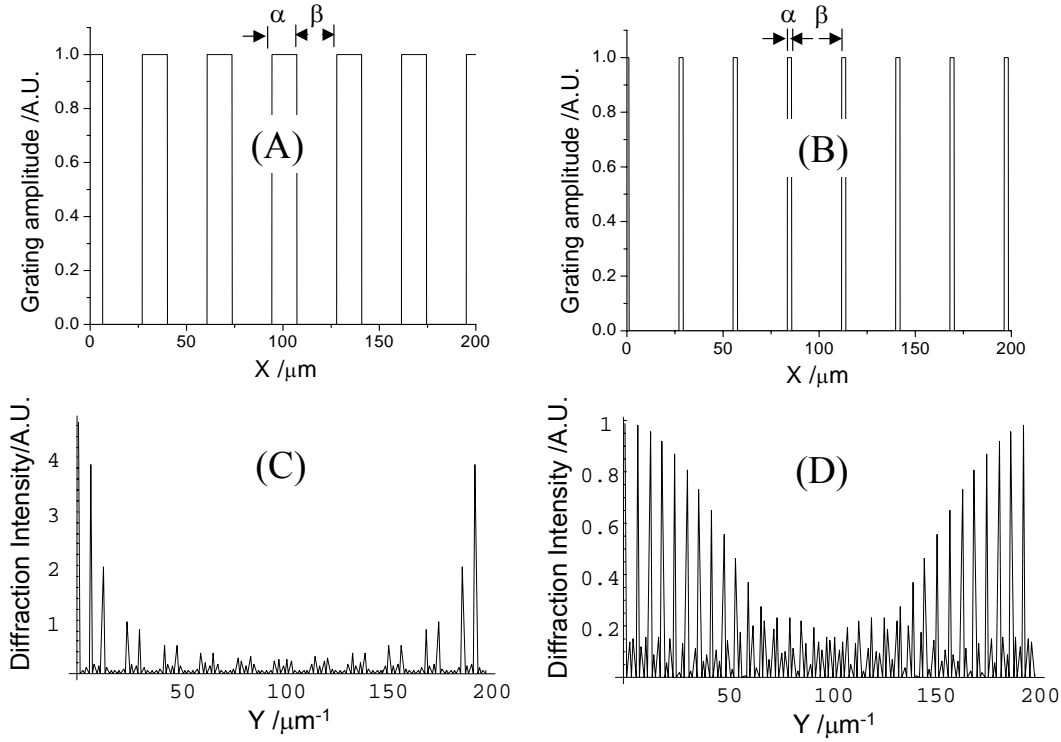


Figure 6.5: Simulations for the diffraction pattern of two kinds of surface periodic structures, both having the same periodicity and contrast while different line widths. The top graphs, (A) and (B), show the cross-sectional profiles of a more symmetric and an asymmetric surface periodic structure; the bottom graphs, (C) and (D), show the Fourier transforms of (A) and (B), representing their corresponding diffraction patterns and intensities.

As indicated by Fourier diffraction optics, the diffraction pattern is a Fourier transformation of the source pattern, which can assist in the proper grating design. For simplicity, patterns of repeating parallel lines were applied represented by square-wave functions. Figure 6.5 shows pattern (A)

and (B) with the equal amplitudes and periodicities ($A=\alpha+\beta$) but different aspect ratios $\rho=\alpha/\beta$, and their corresponding Fourier transforms (C) and (D). A symmetric pattern with ρ closer to 1 concentrates the diffracted intensity at the first several diffraction-orders (cf. Figure 6.5(C)), as it resembles a sinusoidal grating and contains less frequency artifacts. For an asymmetric grating, the diffraction orders are evenly distributed (cf. Figure 6.5(D)), with the intensity being significantly reduced. Therefore, a symmetric grating pattern renders higher diffraction intensity, which generally meets the sensing demand.

6.4 Antibody binding to patterned SAM

6.4.1 Microscopic characterization on patterned surfaces

The Au surface was patterned by μ CP technique using stamp A and B, as is described in chapter 3 (cf. 3.4.2). The patterned Au was designed to have a binary SAM with biotin/spacer thioliates on the functional lines, whereas to have only spacer thioliates on the nonfunctional lines. Two patterns, namely pattern A and pattern B, were fabricated defined by the corresponding stamps. An ‘un-patterned’ surface, means a surface completely covered by a mixed SAM composed of biotin and spacer thiol with molar ratio of 1:9 unless otherwise mentioned.

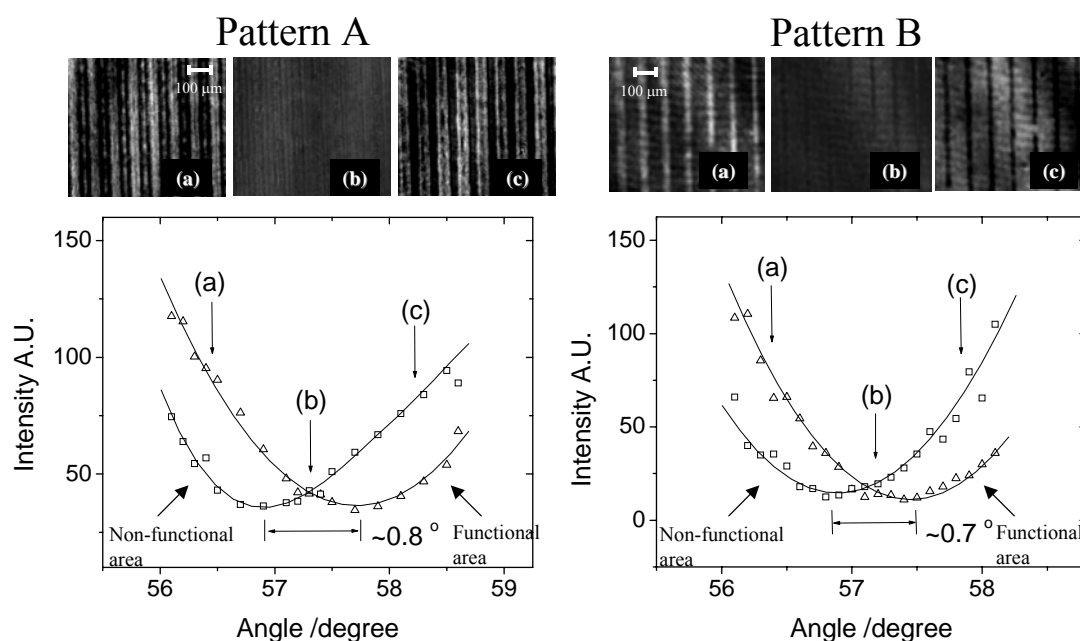


Figure 6.6: SPM angular analysis for pattern A (left panel) and pattern B (right panel) treated with the anti-biotin antibody. The SPM images shown were taken near the SPR resonance angles (their corresponding

angular positions are marked in the plots below, by ‘(a)’, ‘(b)’, ‘(c)’, with the image contrast of both functional and non-functional areas being reversed at the angle position of (b).

An antibody monolayer was bound on the functional regions by exposing the patterned surfaces to an anti-biotin solution (20 nM). The SPM images of both pattern A and B surfaces can be seen in Figure 6.6. By sampling the grayscale value in a series of angular SPM images, the angular reflectivity curves equivalent to SPR were obtained for both functional and non-functional regions, for determining the SPR minimum angle shift $\Delta\theta$, which is proportional to the grating amplitude Δnd . For pattern A and B, the obtained $\Delta\theta$ was $\sim 0.8^\circ$ and $\sim 0.7^\circ$ between functional and non-functional areas, respectively. While on an un-patterned surface completely covered by the biotin SAM (ratio = 1:9), the binding of anti-biotin gave $\Delta\theta = 0.83^\circ \pm 0.03^\circ$ (cf. chapter 4). It manifested that the antibody coverage on the functional stripes of pattern A was nearly as much as that on the un-patterned surfaces. Whereas, the coverage was slightly lowered on the pattern B. This could suggest a decreased molar fraction of the biotin thiolates in the functional area of pattern B (as will be discussed in 6.4.4).

6.4.2 Antibody monolayer induced light diffraction

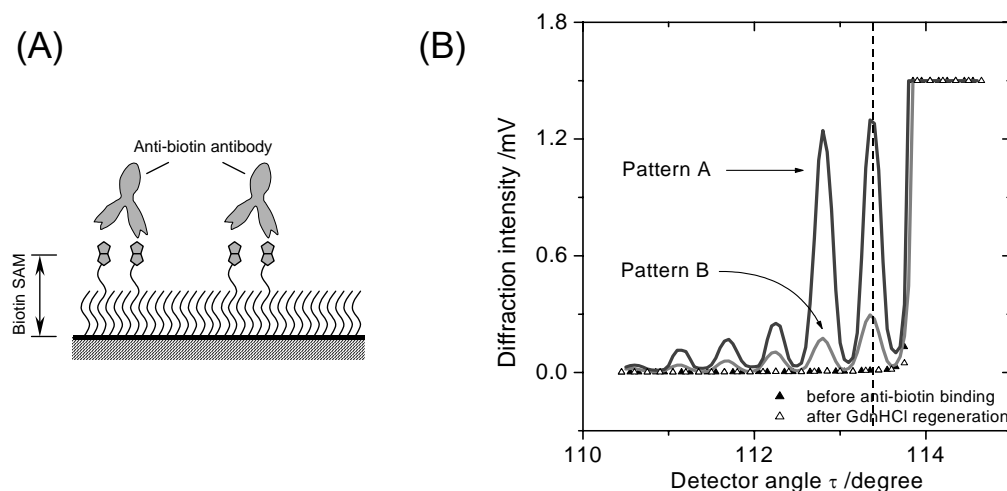


Figure 6.7: (A) Schematic of the anti-biotin antibody binding to the patterned surfaces. (B) Diffraction angular scans obtained on the patterned surfaces with (full black and grey curves for pattern A and B, respectively) and without (full and open triangles) the binding of the anti-biotin.

Prior to the anti-biotin binding, the optical contrasts of both patterned surfaces were originated from the 10% biotin thiol (slightly larger than the spacer thiol), which were insufficient to render measurable diffractions (cf. full triangles in Figure 6.7(B)). Subsequently, significant diffractions

were observed upon exposing the surfaces to the antibody solution (cf. full curves in Figure 6.7(B)). For pattern A, the first two observable diffraction orders had more pronounced intensities, in agreement with the simulation for a symmetric pattern (cf. Figure 6.5(C)). For pattern B, the diffraction intensity was more evenly distributed, also in agreement with the simulation for an asymmetric pattern (cf. Figure 6.5(D)). Noteworthy is that pattern A provided stronger diffraction peaks than pattern B with the close grating amplitudes ($\Delta\theta = 0.8^\circ$ and 0.7°). Moreover, the bound antibodies could be completely denatured and removed from the surface by a pulse injection (<5 minutes) of a 4 M aqueous guanidine hydrochloride solution. The removing of the antibody reset the diffraction pattern to the original level (cf. open triangles in Figure 6.7(B)). Another injection of the anti-biotin antibody resulted in identical diffraction signals, which suggests the surfaces were as $\sim 100\%$ functional as pre-regeneration (data not shown). The patterned surfaces were highly robust to sustain the regeneration condition for many times.

6.4.3 Quadratic effect of diffraction intensity

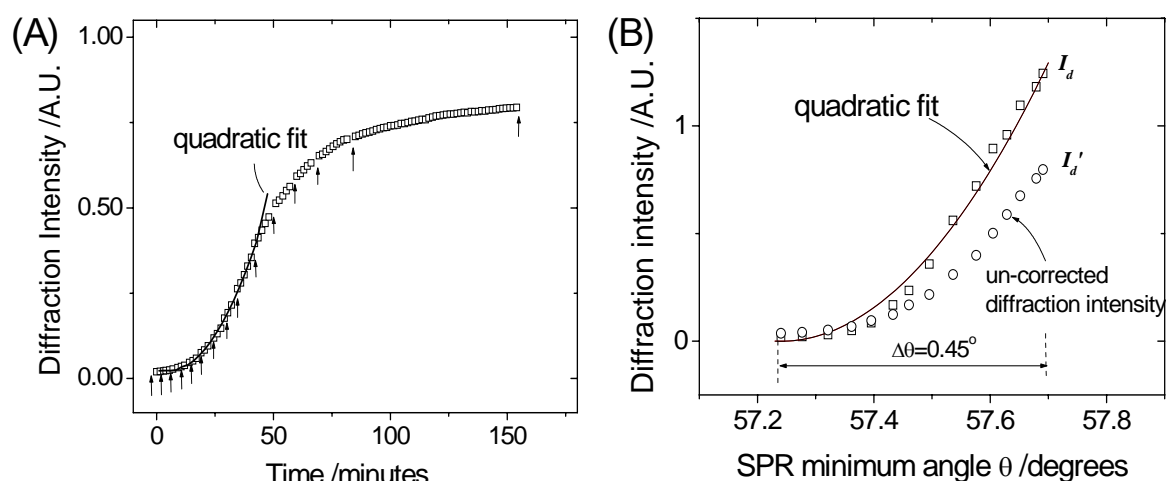


Figure 6.8: (A) Time-resolved diffraction signal upon the binding of anti-biotin antibodies from a 5 nM solution on the surface of pattern A. At each point indicated by an arrow, an SPR scan was performed and the diffraction signals on both the un-corrected and the corrected incident angles were obtained. The kinetic curve started with a quadratic behaviour and gradually reaches equilibrium due to the saturation of the surface biotin sites. (B) Corrected and un-corrected diffraction intensities versus the corresponding SPR minimum angles. (See text for details)

The diffraction intensity could be monitored as a function of time, realizing a kinetic observation of biomolecular bindings. Before introducing the antibody, the incident light was set at the SPR minimum θ_0 to generate a strong PSP field. The detector arm was tuned to the angle of the first observable diffraction peak (cf. dashed line in Figure 6.7(B)). Having a larger biotin area, pattern A surface could give significant SPR and diffraction signal upon the antibody binding, and then a

relationship between both signals could be established. The working concentration of the anti-biotin solution was 5 nM, in order to realize a mass-transport limited binding. Under such condition, the antibody binding could be paused for quantitative SPR/diffraction angular scans by manipulating, e.g., the flow rate of the sample delivering. The following steps were performed at each point indicated in Figure 6.8(A) by an arrow:

- 1) The flow rate was reduced to zero, which largely ceased the antibody binding. Then a diffraction scan was performed to get I_d' .
- 2) An SPR angular scan was performed to obtain the new SPR minimum angle θ . The laser incident angle was then corrected to be at the new θ , to ensure identical PSP coupling. Another diffraction angular scan was performed to obtain I_d .
- 3) The laser incident angle was adjusted back to the original angle θ_0 and the kinetics was continued by recovering the sample flow.

For a typical mass-transport limited binding, a linear signal/time relationship is expected at the initial phase under, e.g., SPR recording. However, a quasi-quadratic increase of the diffraction intensity was observed in the kinetic curve (cf. Figure 6.8(A)). This could be interpreted by the quadratic relationship between the SPR and the diffraction signals as plotted in Figure 6.8(B). Considering that the SPR minimum shift is a linear measure of the grating amplitude Δnd , the relationship coincided with the theoretical prediction (Equation 6.2), as well as the experimental observation by other group.^{120(A)} The angular correction (step 'c') was found to be essential for eliminating the strong "detuning" effect of PSP field (cf. 'un-corrected curve' I_d' - θ given in Figure 6.8(B)) and eventually obtaining proper I_d values. The diffraction signal was considerably underestimated (I_d' versus I_d) if the laser incident angle was kept constant, because the SPR shifted positively up to $\Delta\theta = 0.45^\circ$ causing a corresponding decrease of the PSP coupling efficiency ('detuning').^{14, 92} This needs to be taken into account if the analyte binding induces significant SPR shifts.

6.4.4 Estimation of the biotin density

It remains unclear whether the ratio of the thiolates in the stamped binary SAM is the same as that in the binary SAM prepared in solution, i.e., the 'normal' way (cf. 3.4.1). A rigorous investigation requires the involvement of surface characterization instruments like X-ray photoelectronic spectroscopy (XPS), IR spectroscopy, etc.⁶² However, a general conclusion is still hard to be

drawn since it may vary with different thiol couples. In the following, we attempt to get a preliminary sense of the thiol ratio by the diffractive study of the interaction kinetics.

Due to the bivalent nature of an antibody (two recognition sites per molecule), the desorption kinetics between a bound antibody and its surface-tethered antigen is strongly dependent on the surface density of the antigen, due to a 1:1 to 1:2 binding stoichiometry evolution. In return, knowing the antibody desorption kinetics allows one to estimate the antigen density. In order to calibrate the dependence, an SPR study on a series of ‘un-patterned’ surfaces exposing various biotin densities was conducted. The surfaces were prepared by incubating the Au substrates in mixed thiol solutions with various molar ratios of biotin/spacer thiol from 1:9 to 1:249. The antibody solution (20 nM) was then brought into contact with the surfaces. Upon the binding equilibrium, the antibody was partially desorbed by rinsing with pure buffer, followed by a competitive rinse with a 1 mM biotin solution in order to rule out the influence of any rebinding effect. (cf. 4.6)

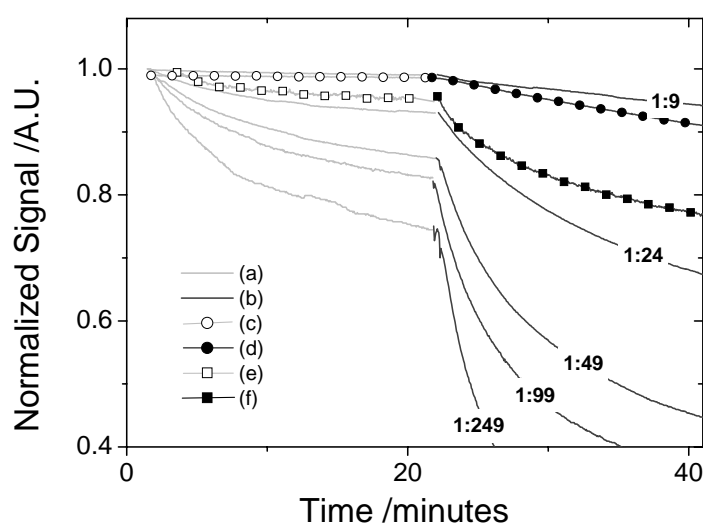


Figure 6.9: Normalized desorption curves for the surface biotin density determination. SPR kinetic results show the desorption (a) and competitive desorption (b) of bound anti-biotin antibody on ‘un-patterned’ SAM surfaces prepared by biotin/spacer thiol mixtures with ratios of 1:9, 1:24, 1:49, 1:99, 1:249, respectively. Curve (c), (d), (e), (f) are the diffraction kinetic curves: (c) and (d) are the desorption and competitive desorption obtained on pattern A surface, (e) and (f) are the desorption and competitive desorption obtained pattern B. The diffraction intensities have been corrected by a square root conversion, considering the quadratic effect of the diffraction signal.

The normalized SPR desorption curves were plotted in Figure 6.9, for a clearer comparison of the desorption rates. In agreement with the prior work,⁷⁸ all the desorption curves had double exponential behaviors, which made the mathematical treatment too complex to quantify the

affinities. Qualitative comparison was given in this sense. For both the normal (cf. curves (a) in Figure 6.9) and the competitive (cf. curves (b) in Figure 6.9) desorbing processes, the antibody desorption was faster on SAM surfaces possessing a lower biotin ratio. Assuming that the cross-sectional area of a thiolate is $A = 0.26 \text{ nm}^2$ and a homogenous mixing of both thiolates, we calculated that the distance between the neighboring biotin thiolates were 1.6 nm, 2.6 nm, 3.6 nm, 5.1 nm, 8.1 nm for 1:9, 1:24, 1:49, 1:99, 1:249 SAM surfaces, respectively. Considering the dimension of a Fab fragment ($\sim 6.5 \times 3.5 \text{ nm}^2$) of an IgG, these distance values could influence the probability of an antibody to bridge between two biotins. Hence, we infer that the experimental affinity evolution indicates a 1:2 to 1:1 transition of interaction stoichiometry between the antibody and the surface biotin, with the statistical enlargement of the biotin distance.

The aforementioned binding/desorbing/competitive desorbing process was performed on the pattern A and B surfaces, monitored by the diffraction kinetic mode. The linearized results were placed into the affinity transition curves calibrated by SPR in Figure 6.9. One can notice that the desorption behavior on pattern A (cf. curve (c), (d) in Figure 6.9) resembled that on the 1:9 surfaces, except a small deviation in the competitive desorption phase. This indicates that the biotin ratio on the functional areas of pattern A was close to that on an un-patterned 1:9 SAM surface. The ratio on the pattern B surface was slightly lower than that on an un-patterned 1:9 SAM surface, as was implied by the faster desorption (cf. curve (e), (f) in Figure 6.9). Both observations were in agreement with the above SPM results, that is, the antibody coverage was slightly lower on pattern B than on pattern A (cf. section 1). We infer that the narrower embossed lines in stamp B (see the supporting information) would probably encounter a deformation that resulted in an incomplete formation of the SAM layer on the contacting areas. The defects were subsequently filled with the spacer thiol, leading to a dilution of the biotin thiolates.

6.5 Self-referencing property

In principle, the SPR signal is sensitive to the refractive index variation within the extension of the evanescent field. Therefore, it can not differentiate between a surface refractive index change by specific molecular binding and any bulk refractive index change, e.g., by temperature or pressure fluctuations. In fact, the engineering approach to fabricate a reference channel (RC) is one of the most efficient ways to improve the quality of SPR sensing.¹²⁶ Accurate referencing is also a crucial aspect for many other label-free biosensors, such as waveguide sensor,¹²⁷ micro-cantilever sensor,¹²⁸ etc. However, since the RC is normally a replication of the sensing channel, it requires an extra set of optical, electronic and fluidic system. Consequently, the whole system

tends to be more expensive and less integrated. In addition to that, the surface preparation of the RC is also a time-consuming step. A recent progress was made by Ratner et al.,^{126(B)} who fabricated a more integrated on-chip RC for SPR. However, it was still based on the concept of ‘dual-beam subtraction’.

For the diffraction-based sensor, only the binding occurring specifically to the functional zone modulates the optical contrast of the ‘dynamic biological grating’, inducing a change of the diffraction efficiency. On the other hand, bulk effects simultaneously influence both functional and non-functional areas, and, hence, are largely compensated. Therefore, in theory, the diffraction-based sensor is inherently ‘self-referencing’. However, special features in SPR-based diffraction sensor need to be taken into account. Since the incident angle of the laser is kept constant for surface plasmon excitation, any bulk effect can influence the diffraction intensity by shifting the surface plasmon minimum angle, thus de-tuning the coupling efficiency of the light to the surface plasmon mode. Therefore, practically it is necessary to fix the incident light at an angle so that a certain shift of the SPR spectrum will have a minimum impact on the plasmon field intensity (i.e. detuning effect^{14, 92}).

As a model system for demonstrating the self-referencing property of the diffraction sensor, streptavidin and biotinylated rabbit anti-goat antibodies (biotin-RaG, from molecular probes) were used to build up the initial surface contrast as well as the functional sub-layer on the patterned biotin SAM (using stamp A, cf. chapter 3), as shown in Figure 6.10(A) schematically. The thickness of the SA and biotin-RaG layers were 3.7 nm and 3.6 nm, respectively, calculated from the SPR response, assuming a refractive index of $n=1.45$ for both proteins. Consequently, significant diffraction peaks emerged, rendering an initial diffraction intensity of ~ 1.05 mV. Meanwhile, there was still a certain amount of un-reacted biotin groups of biotin-RaG for the next interaction study with anti-biotin antibody 2F5.

Figure 6.10(B) shows the corresponding SPR and diffraction responses, respectively, as a function of time recorded after injection of different concentrations of 2F5 (50 pM, 100 pM, 400 pM, 750 pM, 1 nM, respectively) on the same sensor surface. The SPR response was measured by tuning the laser incident to an angle slightly smaller than the SPR minimum angle and monitoring the reflectivity change of the reflected laser beam (i.e., the zeroth diffraction order). On the patterned surface, SPR measures a weighted average of SPR responses from both functional area and non-functional area.¹²⁹ Since there was no contribution from the non-functional area due to the passivation by the spacer thiol,⁹² the SPR response was directly linked to the geometric ratio of the functional area. After each binding assay, the anti-biotin antibodies could be completely

removed from the surface by a pulse injection of glycine buffer (10 mM, pH 1.7), without damaging the strong biotin-SA linkages underneath, as indicated by a stable baseline level. At such low analyte concentrations, the mass-transport rate from the bulk to the functional interface dominated the binding kinetics, and the slope of the binding curve (binding rate) represent a direct relationship with the bulk concentration. Using the diffraction signal, 2F5 binding from a 50 pM solution can still be detected. In contrast, it was difficult to detect the signal from a 100 pM solution of 2F5 by SPR, although one should consider that the effective area contributing to the SPR signal was only approximately 43% (43 μm strips on a 100 μm pitch). However, for practical applications, this small advantage of the diffraction mode can be greatly amplified by considering its baseline stability, given by its self-referencing property.

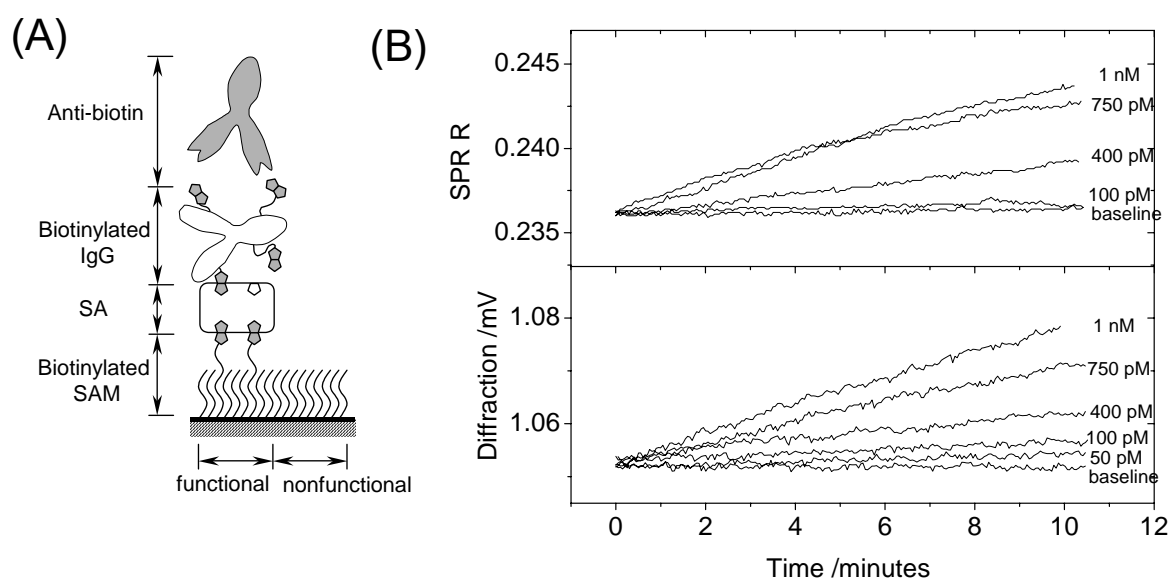


Figure 6.10: (A) Schematic representation of the architecture employed to directly compare the detection limit of the SPR and SP-enhanced diffraction sensor based on the same set-up, respectively. (B, top) SPR binding curves of the surface interacting with 2F5 solutions of different concentrations. (B, bottom) Diffraction kinetics curves of the same surface interacting with 2F5 solutions at different concentrations.

To demonstrate this self-referencing experimentally, a stepwise temperature increase was conducted by a direct comparison between the SPR and the diffraction modes, respectively. On the same sensor surface, two temperatures (32 °C and 43 °C) were subsequently applied and both SPR and diffraction signals were recorded, as shown in Figure 6.11. The temperature in the flow cell was maintained by continuously circulating the bulk solution through a temperature-controlled water bath. At a flow rate of 3 mL/min, it took ~2-3 minutes to bring the in-cell temperature to a new steady state. As a reference, the binding signals of 1 nM solutions of 2F5 are shown in parallel in the figure. As can be seen, a significant decrease of the SPR signal when

applying higher temperatures was found, known to be a consequence of the refractive index change of the bulk solution.¹³⁰ However, little changes could be seen for the diffraction signal when applying the same temperatures, indicating a nearly perfect compensation by its self-referencing mechanism. As a quantitative assessment by referencing to the specific binding signal of 1 nM 2F5, the diffraction signal was at least 50 times less sensitive than the SPR signal to the temperature fluctuations. Such a robustness of the diffraction signal to environmental conditions can be immediately translated into an enhancement of sensitivity. In reality, for un-referenced SPR detection, the noise from switching sample solutions can often exceed the signal, e.g., from a 1 nM 2F5 binding reaction, which is sometimes quite misleading.

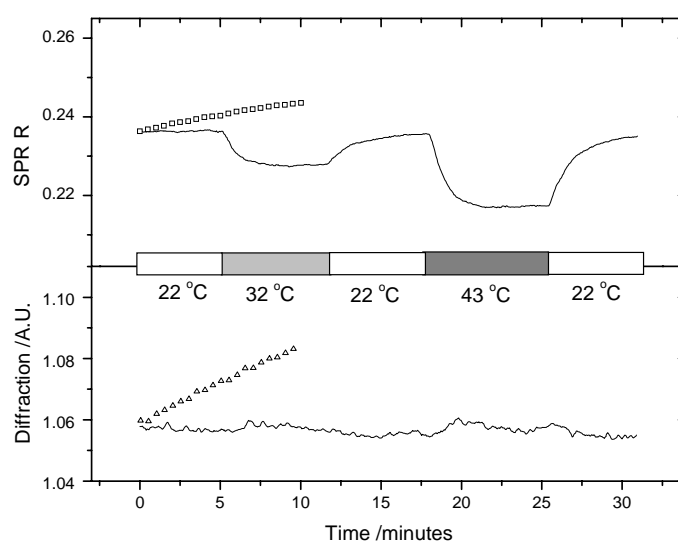


Figure 6.11: Temperature variation study for both SPR- and diffraction modes, respectively. Solid curves are the temperature response of both signals with only buffer solution in the flow cell. The signals from a 1 nM 2F5 binding assay are also shown in parallel for SPR (\square) and diffraction (\triangle), respectively, for comparison.

6.6 Pico-molar sensitivity for hCG detection

Direct detection of a clinically relevant molecule, the hormone human chorionic gonadotropin (hCG), was tested subsequently in order to establish the lower detection limit of our novel sensor platform. The hCG is a 37 kDa protein secreted during pregnancy. Its antibody fragment, anti-hCG Fab was biotinylated and kindly offered by Roche Diagnostics. A sequential binding of SA and the biotinylated Fab layer, as schematically drawn in Figure 6.12(A), generated the initial optical contrast and the surface functionality. The ‘thickness’ of the SA and the Fab layers were

3.8 nm and 4.0 nm, respectively, as determined by SPR measurements, assuming a refractive index of $n=1.45$ for both proteins. This indicates a nearly 1:1 stoichiometry of the SA/Fab interaction, which coincides with former results. (cf. 4.12)

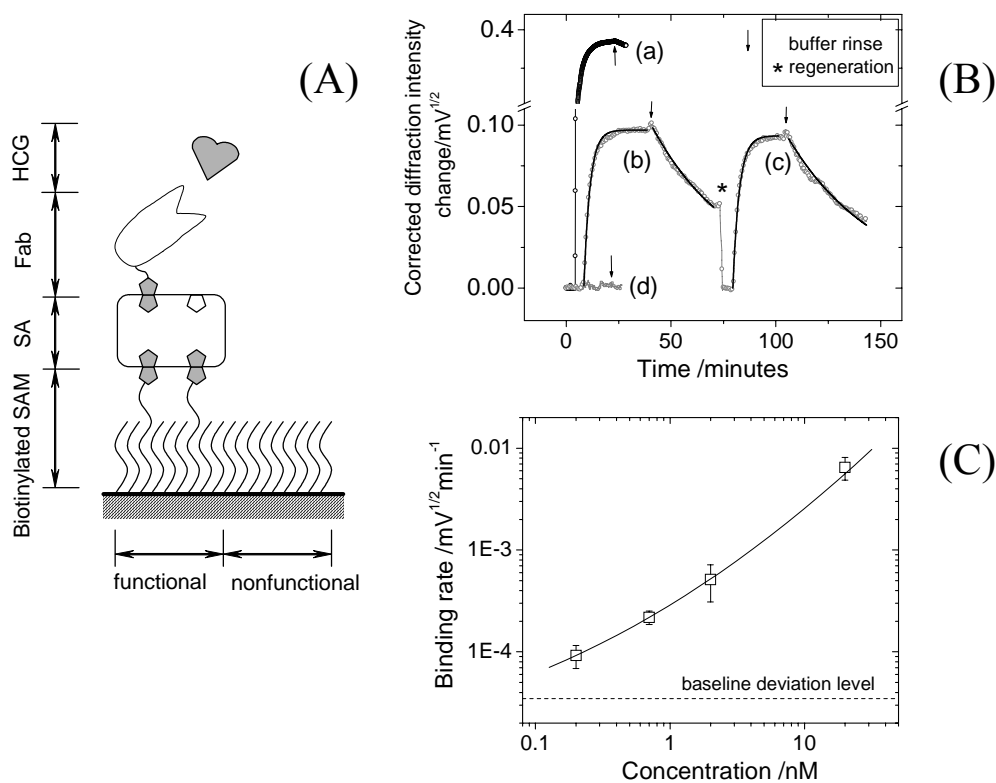


Figure 6.12: (A) Schematic drawing of the diffraction detection of hCG. (B) Curve (a): the binding of 500 nM biotinylated anti-hCG Fab solution on the SA derivatized surface; curve (b) the binding of a 50 nM hCG solution on the Fab surface; curve (c) the binding of a 50 nM hCG solution containing 1 mg/mL BSA on the Fab surface regenerated from (b); curve (d) the non-specific binding of 1 mg/mL BSA solution. Langmuir fits (solid curves) were applied for curve (b) and (c), yielding identical rate constants. The arrows indicate the buffer rinses. (C) Dose-response curve of the direct hCG binding assay. The baseline deviation level was obtained by averaging the responses of pure buffer.

Figure 5(B) shows the binding curves of the Fab, hCG and BSA solutions, respectively. All the kinetic traces were corrected concerning the quadratic effect of the diffraction signal (cf. equation (1)) by the following equation:

$$I_c = \sqrt{I_d - I_b} \quad \text{--- 6.4}$$

where I_c , I_d , I_b are the corrected intensity, the raw diffraction intensity and the background intensity, respectively. I_b is the intensity arising from the random surface scattering due to the surface roughness, which was measured to be typically ~ 0.01 mV on a bare gold surface. By this

correction, I_c linearly reflects the grating amplitude Δnd . As can be seen, a quick binding equilibrium was achieved within 5 minutes after the injection of biotinylated Fab (cf. curve (a)). Little signal loss was seen upon rinsing with pure buffer, owing to the high affinity of the biotin-SA linkage. The binding of hCG from a 50 nM solution to the Fab-derivatized surface (cf. curve (b)) showed a significantly lower endpoint signal than the Fab binding, corresponding to the lower molecular weight of hCG and interaction efficiency. By a pulse injection of the glycine buffer, the Fab surface could be completely regenerated. Another hCG binding in the solution containing 1 mg/mL BSA presented the identical association/dissociation behavior (cf. curve (c)), indicating negligible interference from the presence of ~300-fold BSA. Exposing the sensor surface to the BSA solution rendered no observable signal drift (cf. curve (d)), indicating the specificity of the sensor surface. Single-exponential kinetic fits based on a 1:1 Langmuir interaction model (cf. 2.4.3) could be applied for the association/dissociation analysis of curve (b) and (c). Identical dissociation constants (K_D) were found to be 3.9 nM and 4.0 nM for curve (b) and (c), respectively. These values were in good agreement with the independent SPR studies on an unpatterned surface with the same multi-layer system, which gave $K_D = 6.1 \pm 0.5$ nM. This manifests the applicability of the diffraction sensor for biomolecular interaction studies.

The LOD of the direct hCG assay was assessed by a sequential injection of hCG solutions with decreasing concentrations (20 nM, 2 nM, 700 pM, 200 pM). Since these low bulk concentrations favored the mass-transport limited binding kinetics (2.4.2), the initial slope of each binding curve (binding rate) was calculated and plotted in Figure 5(C). The experimental errors were given by four measures for each hCG concentration. As can be seen, the dose-response curve could be extended into the 200 pM hCG concentration, which is quite remarkable for detecting this small protein. The slope of the baseline fluctuations was still lower than the studied lowest binding signal, indicating the potential of further improvement of the hCG sensor.

6.7 Oligonucleotide hybridization studies

The detection and analysis of genetic material has drawn unprecedented research efforts during the past decades due to the increasing interest arising from both application and fundamental research concerns. Methods for the label-free detection of oligonucleotide DNA binding through base pairing have been reported based on optical¹³¹, electrochemical¹³², piezoelectric¹³³ and nanomechanical¹²⁸ techniques. The basis of operation for a DNA sensor is the coupling between a specific base sequence within a DNA target analyte and the complementary oligonucleotide

sequence immobilized on the solid surface of a transducer substrate. This DNA hybridization can be detected as a physical signal and can be monitored in-situ and in real-time.

Due to the small size (mass) of a typical oligonucleotide, its binding to the surface is usually not sufficient to generate a significant optical contrast. Hence, it is experimentally a major challenge for label-free optical sensors to conduct a thorough investigation of this interaction. A few commercial optical biosensors have realized label-free DNA sensing with the aid of 3-D surface matrices used to enhance the DNA surface coverage.^{131(A),(E)} Only a few reports^{131(C),(D)} were based on planar functional surfaces, and additional signal amplifications were often required for successful investigations.^{8,9} Here, we consider this novel diffraction sensor to be an attractive candidate in detecting and characterizing oligonucleotide hybridization processes.¹³⁴

In order to have a highly functional surface and to obtain correct kinetic and thermodynamic parameters of oligonucleotide interactions, it is also of vital importance to carefully engineer the functional surface matrices in addition to the instrumental development of the optical DNA sensors. A major aim is to overcome hybridization barriers from, e.g., steric hindrance and/or electrostatic repulsion. One successful example, a planar functional layer fabricated by the attachment of thiolated DNA oligonucleotides to the sensor surface via a gold-thiol bond has been shown by SPR^{131(C)} and neutron reflectivity¹³⁵ studies to be nearly 100% functional. We employ here our functional matrix based on a well-developed biotin-streptavidin supramolecular architecture that has been used already extensively in DNA hybridization studies by SPFS. The streptavidin monolayer is formed on a mixed SAM exposing 5-10% biotin functionalities. The remaining biotin-binding pockets (approx. 1-2) in the surface-attached streptavidin allow for a subsequent attachment of biotinylated DNA probes, with the size of the streptavidin providing a natural limitation of the probe surface density for the next interaction step – the target hybridization. This functional multi-layer system has been working quite efficiently for SPFS characterization with extraordinarily high sensitivity and a number of different modes of operation. However, due to the distance-dependent fluorescence yield in SPFS and the lack of label-free information of the oligonucleotide binding, many details of the hybridization process, e.g., the hybridization efficiency remains unknown.

In this study, we examined the interactions of four different oligonucleotide DNA targets of different length and base sequence with surface-tethered probe DNA oligonucleotides by the diffraction sensor. Similar to the hCG detection, the pattern A surface was employed, providing the initial biotin functionality. The biotinylated DNA probe and DNA targets (T15-0, T15-1, T15-2, T75-0, T75-1) were purchased from MWG-biotech, and are listed in Table 6.1. The 75-mer

targets (T75-0, T75-1) consist of the same recognition sequences as the 15-mer targets (T15-0, T15-1), however, have two flanks of poly T (30-mer). The T15-0 and T75-0 are fully complementary to the DNA probe, i.e., they define a mismatch zero (MM0) situation, while one base mismatch (MM1) was designed in the sequences of T15-1 and T75-1, respectively. A two-base mismatch (MM2) was designed for the T15-2 target. HBS-EP buffer (degassed 10 mM HEPES buffer saline, pH 7.4, 150 mM NaCl, 3 mM EDTA, 0.005% (v/v) surfactant P-20, Biacore, Uppsala, Sweden) was used for the preparation of all of the protein/DNA solutions.

DNA probe	biotin-5'-T(15) TGT ACA TCA CAA CTA-3'
Target T15-0	5'-TAG TTG TGA TGT ACA-3'
Target T15-1	5'-TAG TTG TGA <u>C</u> GT ACA-3'
Target T15-2	5'-TAG TTG <u>TCA</u> <u>C</u> GT ACA-3'
Target T75-0	5'-T(30) TAG TTG TGA TGT ACA T(30)-3'
Target T75-1	5'-T(30) TAG TTG TGA <u>C</u> GT ACA T(30)-3'

Table 6.1: DNA oligonucleotide sequences used in this study.

6.7.1 Kinetic studies

The schematic drawing of the employed multi-layer architecture composed of SAM/streptavidin/probe/target is shown in Figure 6.13(A). The processes were recorded as the sequential increase of the diffraction signal as shown in Figure 6.13(B). One can see in the raw experimental data (gray curve) that the initial diffraction intensity induced by the patterned biotin SAM surface was quite weak and almost close to zero. Exposing the patterned surface to a 1 μ M SA solution leads to a quick increase of the diffraction signal followed by a second slower increasing phase. The second phase is considered to be associated with a non-specific aggregation of SA molecules because a pure buffer rinse could gradually wash away the signal accumulated in that phase. After a long-time rinse, the baseline remained at approx. 0.48 mV and was extremely stable. The SPR minimum shift upon the SA binding on the patterned surface was measured to be $\Delta\theta_0 = \sim 0.2^\circ$. Taking into account the fraction (43%) of the functional area relative to the whole surface area, this angle shift on the patterned area is consistent with previous results ($\Delta\theta_0 = \sim 0.45^\circ$, corresponding to a thickness of $d = \sim 3.8$ nm assuming $n=1.45$ for the proteins) obtained on a

surface homogeneously functionalized by a mixed biotin/spacer thiol solution (1:9), confirming the formation of an identical SA coverage ($\sim 2.2 \times 10^{12}$ molecules cm^{-2}). The injection of a 1 μM DNA probe solution induced another quick jump of the baseline to a higher level of approx. 0.68 mV. Only a minor signal decrease was observed upon the exchange of the DNA probe solution by pure buffer, indicating a strong and highly specific binding of the probe oligonucleotides via the biotin-SA linkage.

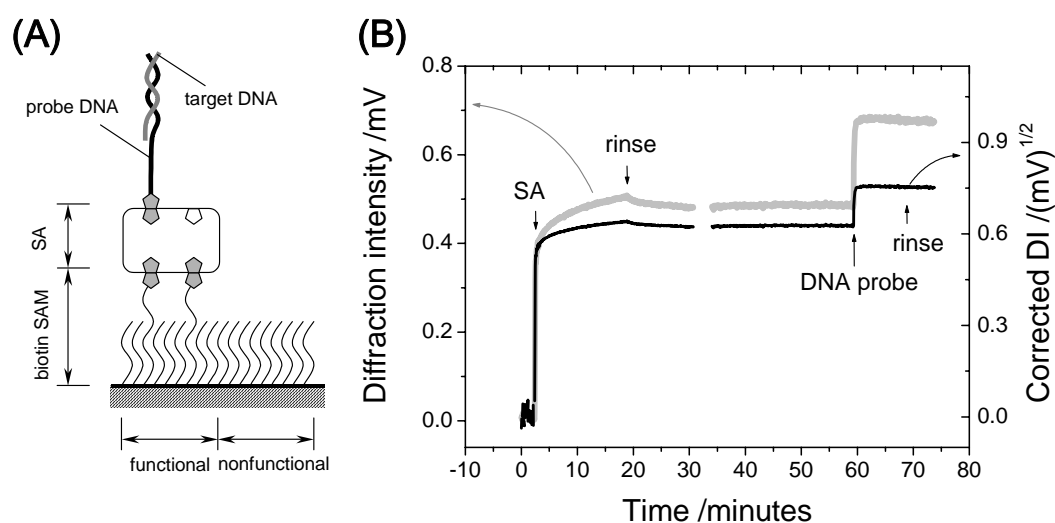


Figure 6.13: (A) Schematic diagram of the multi-layer architecture built on the functional pattern surface. (B) Experimental (gray curve) and corrected (black) kinetic curves of the SA and DNA probe binding (both from a 1 μM solution).

For the quantitative analysis, the experimental curve was corrected (cf. black curve in Figure 6.13 (B)), considering the quadratic relationship between the diffraction intensity (I_d) and the amplitude of the index-of-refraction grating (Δnd), cf. Equation 6.2). One should notice that the background intensity I_b due to the random surface scattering should be subtracted. I_b can be obtained from a measurement on an un-patterned gold surface, and is typically found to be ~ 0.01 - 0.05 mV. (cf. Equation 6.4). Therefore, $\Delta\sqrt{I_d - I_b}$ gives the increment of the corrected diffraction signal that is considered to be a response linear to the optical thickness of each layer, which in return is a linear function of the mass concentration of the bound biomolecules. Taking into consideration that proteins and oligonucleotides have similar refractive indices (n) and do not differ considerably with respect to their SPR response, $\Delta\sqrt{I_d - I_b}$ divided by the corresponding

molecular weight (Mw) provides the relative molar surface concentration, and can be used to calculate the stoichiometry between interacting molecules.

The subsequent association/dissociation measurements of the various DNA targets (T15-0, T15-1, T15-2, T75-0, T75-1) performed sequentially on the same sensor chip are presented as corrected signals in Figure 6.14. The working concentration for each target solution was 1 μM to ensure sufficiently high mass-transport rates for a correct kinetic evaluation. After reaching equilibrium, the target solution was exchanged against the pure buffer in order to dissociate the bound hybrids and to rinse the target strands away. A one-minute-pulse injection of 10 mM NaOH/water solution completely regenerated the probe surface. The same sensor chip could be regenerated at least 30 times and could be used for up to 48 hours without any significant loss of its functionality.

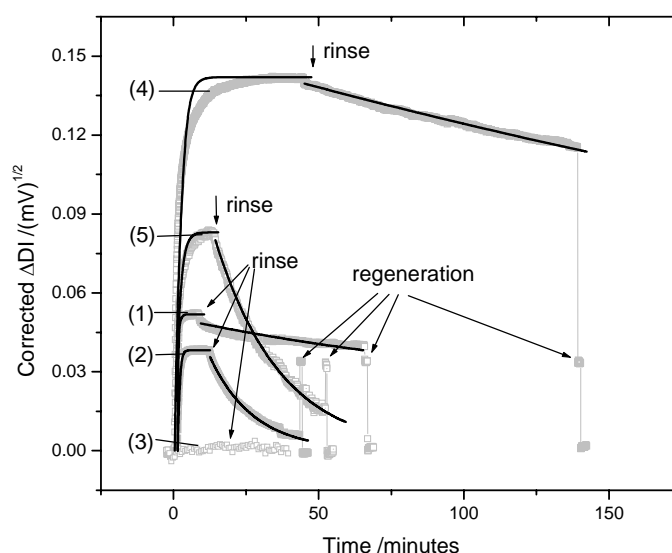


Figure 6.14: Kinetic curves of hybridization from (1 μM solutions) of different targets, i.e., T15-0 (curve (1)), T15-1 (curve (2)), T15-2 (curve (3)), T75-0 (curve (4)), T75-1 (curve (5)) to the probe surface. A 1-minute pulse injection of 10 mM NaOH solution was used to regenerate the probe surface with $\sim 100\%$ recovery. Signal-exponential fits derived from a 1:1 Langmuir model were applied to derive the association/dissociation phases of the binding curves. The obtained corresponding kinetic constants were used for the K_A calculations.

The in-depth analysis of the results of the hybridizations studies, as well as, of the binding of the SA and probe are listed in Table 6.2. Firstly, the binding stoichiometry between probe DNA and streptavidin was $\sim 1: 0.77$. This means that on average 1.3 probe strands were immobilized on each bound SA molecule. Since the surface concentration for the SA monolayer was $\sim 2.2 \times 10^{12}$ molecules cm^{-2} , i.e., each SA molecule occupies an area of approx. 45 nm^2 , the surface concentration of the probe is $\sim 2.9 \times 10^{12}$ molecules cm^{-2} , which is close to a so-called ‘high’ probe density reported by Georgiadis and coworkers.^{131(C)} The HE was also calculated for each target.

High HEs (84%, 62%) were calculated for T15-0 and T15-1 targets, respectively. However, substantially lowered HEs (46%, 27%) were found for the T75-0 and T75-1 targets, respectively. We infer that the extra two poly-T flanks for the 75-mers play a major role in decreasing the HE, owing to the steric/electrostatic hindrance. Also, the longer extension of the hybridized 75-mers away from the surface may slightly lower their contribution to the optical thickness change sensed by the surface plasmon evanescent field, which decays exponentially into the solution with a depth of $L_z \approx 150$ nm.

Name	Mw (kDa)	Response [†]	Stoichiometry ^{††}	k_{off} (s ⁻¹)	k_{on} (M ⁻¹ s ⁻¹)	K_A (M ⁻¹)
Streptavidin	~60	5.1	0.75	--	--	--
biotinylated probe	9.488	1.0	--	--	--	--
T15-MM0	4.622	0.42	0.84	1.32×10^{-4}	6.58×10^4	4.98×10^8
T15-MM1	4.607	0.31	0.62	1.11×10^{-3}	2.42×10^4	2.18×10^7
T75-MM0	22.873	1.14	0.46	3.52×10^{-5}	9.21×10^3	2.62×10^8
T75-MM1	22.858	0.67	0.27	7.41×10^{-4}	1.08×10^4	1.46×10^7

Table 6.2: Molecular weight (Mw), corrected response [†], interaction stoichiometry (hybridization efficiency for probe/target interactions) ^{††}, interaction rate constant k_{on} and k_{off} , affinity constant K_A for the interactions shown in Figure 2 and Figure 3.

[†] Defined as the increment of corrected diffraction intensity (see text for details) normalized to the response of the biotinylated probe.

^{††} Defined as stoichiometry = (SA or DNA target response × Mw of biotinylated probe) / (biotinylated probe response × Mw of SA or DNA target)

The association/dissociation rate constants (k_{on} , k_{off}) of the target oligonucleotides were determined by fitting the working curves to a 1:1 Langmuir model, assuming pseudo-first-order association/dissociation kinetics. Within the Langmuir model we then obtained the affinity constant K_A which is simply the ratio of the two rate constants:

$$K_A = \frac{k_{on}}{k_{off}} \quad \text{--- 6.5}$$

At a first glance, the one-base mismatch induced an apparent difference in the binding curves between T15-0 and T15-1, T75-0 and T75-1, especially in the dissociation phases. The obtained K_A values differed by more than an order of magnitude between the 15-mers (4.98×10^8 M⁻¹, 2.18×10^7 M⁻¹ for T15-0, T15-1 respectively) and the 75-mers (2.62×10^8 M⁻¹, 1.46×10^7 M⁻¹ for

T75-0, T75-1 respectively). A mismatch-two sequence T15-2 was also tested, however, yielded a negligible binding signal. This demonstrated that the obtained hybridization signals were highly specific and the sensor was sensitive to a single-base-pair mismatch. The affinity parameters of T15-0 and T75-0, and of T15-1 and T75-1, respectively, were close, since they contain the same recognition sequences. It is also worth noticing that the pseudo-first-order fitting did not completely match the association behaviors of the 75-mer targets. This reflects, again, the influence from their bulky poly-T flanks. Firstly, extra time/energy might be needed to change their conformation to form the surface double helix. Secondly, bound 75-mers could influence the surface recognition sites, influencing the subsequent binding events electrostatically and/or sterically. Therefore, the Langmuir 1:1 model didn't quite apply for the binding of 75-mers, since the interfacial steric/electrostatic cross talk existed. However, the fits still reflect qualitatively the decrease in hybridization affinity by introducing a single-base-pair mismatch.

6.7.2 Equilibrium titration

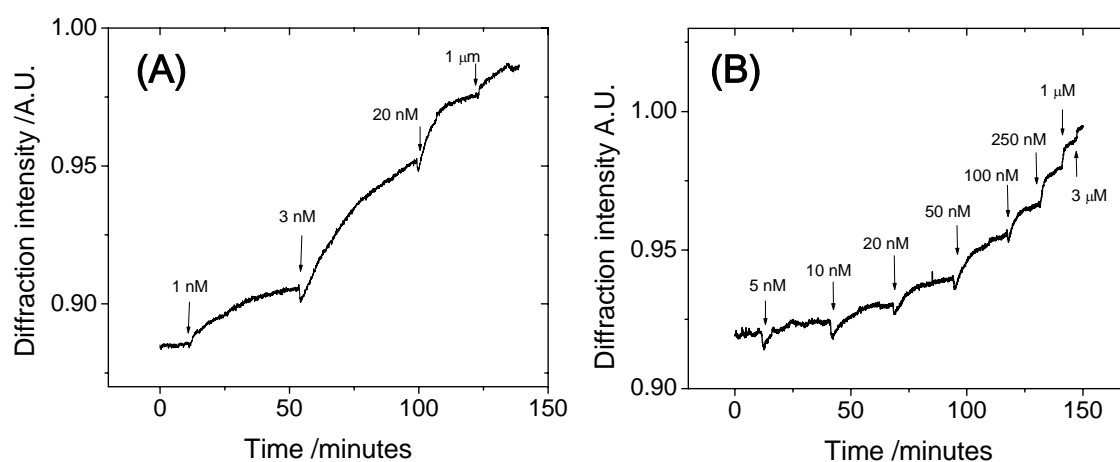


Figure 6.15: Kinetic curves of the equilibrium titrations of T15-0 (A), T15-1 (B) with increasing concentrations to the probe surfaces.

The affinity constants K_A of the 15-mers were also determined by recording the equilibrium binding to the probe surface at different bulk target concentrations c_0 (cf. Figure 6.15). The total span of the target concentration was from 1 nM to 3 μM. The normalized equilibrium response was plotted against the corresponding concentrations c_0 , as shown in Figure 6.16.

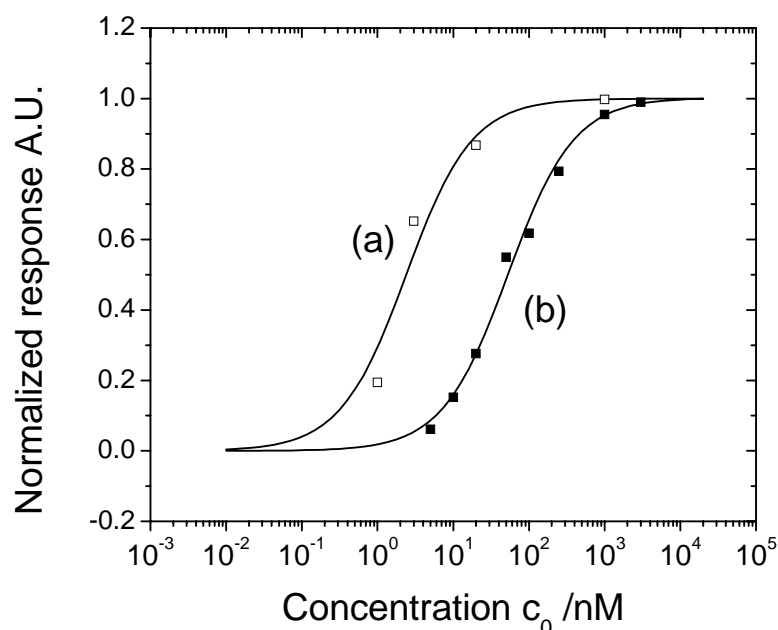


Figure 6.16: The equilibrium signals of titrations with T15-0 (a) and T15-1 (b), respectively. They are normalized to the saturation responses of the corresponding target at its maximum concentration.

A non-linear steady-state fit, based on Langmuir 1:1 model, allows for the determination of K_A , according to:

$$\Gamma = \frac{K_A c_0}{1 + K_A c_0} \quad \text{--- 6.6}$$

with Γ being the normalized response (surface coverage), and c_0 the bulk concentration. The affinity constants for T15-0 and T15-1 were $4.17 \times 10^8 \text{ M}^{-1}$ and $1.92 \times 10^7 \text{ M}^{-1}$, respectively, in good agreement with the affinity constants obtained from the single association/dissociation study. This implies that, the Langmuir model can be applied for the parametrization of the hybridization processes of the 15-mers.

As a preliminary assessment of the LOD of this DNA sensor, we refer back to Figure 6.15. The saturation response of the titration curves for the T15-0 and T15-1 targets corresponds to a coverage of $\sim 2.4 \times 10^{12} \text{ molecules cm}^{-2}$ and $\sim 1.8 \times 10^{12} \text{ molecules cm}^{-2}$, respectively. For T15-1, the 5 nM solution gave an equilibrium signal at 6% of its saturation coverage, which could be easily resolved above the baseline fluctuation. Therefore, we claim that SPDS can detect at least $1.1 \times 10^{11} \text{ molecules cm}^{-2}$ of the 15-mer oligonucleotide, equivalent to a mass concentration of $\sim 800 \text{ pg cm}^{-2}$.

This preliminary LOD level is already comparable to one of the best performance of label-free SPR sensing using near-infrared imaging by Corn's group, where the LOD was reported to be 10

nM for 18-mer oligonucleotide, corresponding to $\sim 10^{11}$ molecules cm^{-2} .^{131(D)} However, the sensitivity is still approximately by a factor of 6 poorer than SPFS assay incorporating a fluorescently labeled DNA target, where the LOD of 2×10^{10} molecules cm^{-2} was estimated.^{22(A)} We expect the LOD of SPDS can be greatly improved with the aid of mass-amplification strategies, by which Keating et al. amplified the SPR response by 1000-fold using Au nanoparticles.^{134(B)}

6.7.3 Probe density engineering

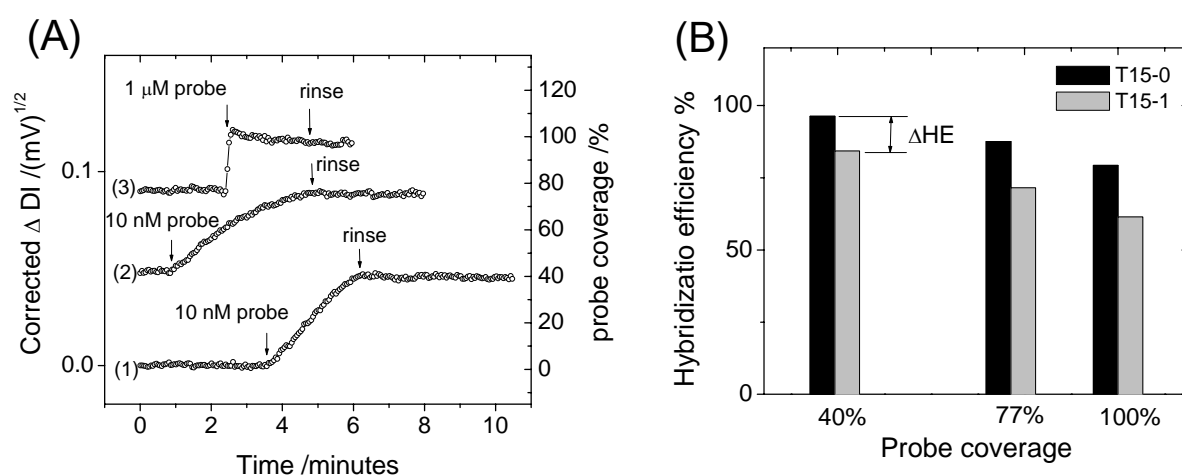


Figure 6.17: Influence of the probe density on the hybridization efficiency of 15 mer targets: (A) Controlling of the probe coverage by a sequential loading strategy at low working concentration. Three steps were applied, with the injections of 10 nM (curve (1)), 10 nM (curve (2)), and a 1 μM (curve (3)) probe solution followed by a buffer rinsing, respectively. (B) Hybridization efficiency as a function of probe coverage for T15-0 and T15-1 target, respectively.

It has been demonstrated^{131(C), 136} that the probe density plays a very important role in the target surface hybridization behaviors, i.e., for the binding kinetics and the hybridization efficiency. In order to conduct this study with our matrix, we controlled the probe density in our system by bringing diluted probe concentration (10 nM) into contact with the SA functionalized surface. Under constant flow conditions, the binding of the probe was completely controlled by the mass-transport rate due to the low bulk concentration of probe molecules. Thus, the binding was greatly slowed down and linear in time before nearly saturating the surface sites, which facilitated an easy control of the probe density. Based on the known interaction stoichiometry between SA and probe, the increasing signal could be immediately stopped at any desired probe density level by exchanging the probe solution by pure buffer. As can be seen in Figure 6.17(A), we thus controlled the probe density at 3 levels of coverage, i.e., 40%, 77% and 100%. In order to ensure

the 100% coverage for the third (final) level, a 1 μM biotinylated probes solution was applied. Competitive desorption of a very small amount of SA from the surface that usually could be seen, resulted in a small drop following the abrupt initial jump upon the sample exchange (cf. curve (3) in Figure 6.17(A)). These levels of coverage were calculated to be equivalent to a probe density of $\sim 1.2 \times 10^{12}$ molecules cm^{-2} , $\sim 2.2 \times 10^{12}$ molecules cm^{-2} , $\sim 2.9 \times 10^{12}$ molecules cm^{-2} , respectively.

The hybridization experiments using 15-mer oligonucleotide targets at a concentration of 2 μM were performed at each level of probe density. The high target concentration was used to ensure the (almost) saturated occupation of the available hybridization sites (cf. Figure 6.16). The endpoint hybridization signals reached at association equilibrium were corrected, considering the quadratic effect of the diffraction sensor. Based on their corresponding molecular weights, the HEs were quantified and plotted in Figure 6.17(B). One can see that the HE of both targets increased with the probe coverage decreasing. This agrees with previous reports using electrochemical^{136(A)} and SPR^{136(B)} approaches and can be explained by the alleviation of the static and/or electrostatic barrier on diluted probe surfaces. For the 40% probe surface density, i.e., at a probe coverage of $\sim 1.2 \times 10^{12}$ molecules cm^{-2} , the HE value of T15-0 reached $\sim 96\%$, indicating that the surface was (nearly) totally functional which can be attributed to the good orientation and moderate density built on the SAM/SA supra-architecture. This result is in agreement with previous observations, where HE reached $\sim 100\%$ at a probe density of 1.5×10^{12} molecules cm^{-2} for a MM0 25-mer and 18-mer targets.^{131(C)} An interesting observation is that the highest HE of the T15-1 target was only $\sim 85\%$ even at the lowest probe density studied, although operating at a saturation concentration, which was also in agreement with result in the same report. This implies a reduced availability of sites for MM1 target hybridization by a higher hybridization barrier due to the internally mismatched base. On the other hand, the difference in HE (ΔHE , cf. Figure 6.17(B)) between the MM0 and MM1 targets could only be slightly alleviated by lowering the probe density, which may indicate certain heterogeneity of the probe distribution. One could speculate that this arises from the partial multiple loading of one streptavidin molecule by probe strands, as already indicated by the average stoichiometry between probe and SA (~ 1.3).

6.8 Conclusions

Surface plasmon enhanced evanescent field at a (noble) metal/dielectric interface can be employed to enhance the diffraction efficiency of surface grating structures composed of biomolecules. Based on a Kretschmann configuration, we realized a diffraction sensor to monitor the dynamic interaction of biological molecules in a label-free way. It was demonstrated by the

binding of an anti-biotin antibody to the biotin functionalized region of a periodically patterned surface, which generated significant optical contrast to diffract the surface plasmon field. With the aid of the simultaneously measured SPR signal, a quadratic dependence of the diffraction signal on the amount of bound antibody was found, which coincides with the theoretical expectation. Time-dependent measurements were conducted to estimate the density of biotin thiols on the functional region. The inherent self-referencing mechanism of the surface diffraction was found to be very effective for compensating fluctuations of the bulk, demonstrated by a temperature variation experiment. Operating with a stable baseline signal, the diffraction sensor offered picomolar sensitivity in directly detecting the binding of hCG hormone. Finally, SPDS was successfully applied for the study of hybridization reactions between DNA oligonucleotides. Signal base-pair mismatch could be discriminated and the lowest detectable coverage for a 15-mer oligonucleotide was at least $\sim 1.1 \times 10^{11}$ molecules cm^{-2} .

7 Summary

In this study, surface plasmon fluorescence spectroscopy and surface plasmon diffraction spectroscopy were used for the in-depth characterizations of the interfacial biomolecular interactions. The efforts in designing, assembling and structurally and functionally characterizing supramolecular architectures for bioaffinity studies and for (bio-)sensor development were included.

In the first part of this study, the SPFS was used to characterize the protein interactions on planar functional surface matrices, initialized with mixed self-assembled monolayers. A model system incorporating the interaction between a surface attached biotin (antigen) and antibodies in the solution was firstly applied to address the fundamental features of the SPFS protein study, such as the surface inertness to non-specific bindings, sensor regeneration, mass-transport limited binding, antigen density controlled antibody avidity, fluorescence detuning effect, the fluorescence self-quenching, etc. Especially, taking advantage of the distance-dependent fluorescence profile on the planar interface, the three-dimensional nature of the protein arrangement was deduced by collecting information from both SPR (interfacial refractive-index) and fluorescence (distance-dependent quenching) signal channels. The ability of SPFS to detect binding to surfaces containing extremely diluted antigen-density was also stressed. Then, a layer-by-layer protein assembly was used to build a protein multilayer, offering a functional matrix with alleviated fluorescence loss. The affinity determination of hIL8 with its antibody fragments was done on the multilayer functional matrix, showing comparable results to the commercial biosensor.

In the second part, a three-dimensionally extended functional matrix, dextran matrix from Biacore, was applied to SPFS offering significantly less metal-induced fluorescence quenching and larger protein binding capacity than the two-dimensional matrix. These advantageous features enabled SPFS to detect extremely diluted analyte, e.g., at attomolar (10^{-18} M) or zeptomole (10^{-21} Mol) level. PSA sandwich assay by SPFS was also established, even with the interference of human plasma. The LOD of PSA was ~ 80 fM, which adequately fulfills the stringent requirements in clinical diagnosis. With the aid of the dextran matrix, SPFS becomes arguably one of the most sensitive biosensor.

In the final part, a novel biosensor based on surface plasmon field-enhanced diffraction phenomena was developed. The resonant coupling of surface plasmons to radiation modes by use of dielectric gratings gives rise to strong diffraction orders, which was utilized for biosensing purposes. By a simple two-step patterning procedure, highly functional and robust sensor surfaces can be fabricated. The association/dissociation of the analyte molecules led to the formation of a dynamic biological grating, a process that could be followed by the change in diffraction intensity. Two model systems were employed in order to demonstrate the potential of this diffraction sensor for routine studies of immuno-interactions and oligonucleotide hybridizations. Its novel characteristics were discovered and concluded to be essential: (1) surface plasmon field enhancement; (2) quadratic signal dependence on the optical contrast; (3) self-referencing mechanism.

8 Supplement

8.1 Abbreviations

2F5	anti-biotin antibody
AF 647	Alexa Fluor dye (maximum absorption peak at 647 nm)
ATR	attenuated total reflection
BIA	biomolecular interaction analysis
bp	base pairs
BSA	bovine serum albumin
CCD	charge coupled device
CMC	critical micelle concentration
CMD	carboxymethyl dextran
Cy5	cyanine dye
D/P	dye-to-protein ratio
Da	Dalton (g/mol)
DNA	deoxyribonucleic acid
EDC	carbodiimide hydrochloride
EDTA	ethylene diamine tetra acetate
EG	ethylene glycol
EIA	enzyme immunoassay
ELISA	enzyme-linked immunoadsorbent assay
Fab	antigen-binding fragment
FIA	fluoroimmunoassay
FOS	fiber-optic spectrometer
FRET	fluorescence resonance energy transfer
GaM	goat anti-mouse antibody
GdnHCl	guanidine hydrochloride
h	Planck's constant
HBS-EP	hepes buffer saline with EDTA
hCG	human chorionic gonadotropin
HE	hybridization efficiency
HeNe	Helium-Neon
IgG	immunoglobulin
IL	interleukin
\vec{k}	wave vector
K_A	affinity constant
K_D	dissociation constant
LA	lipoic acid
LASFN9	high refractive index glass from Schott
LBL	layer-by-layer
LOD	limit of detection
MM	(base pair) Mismatch

Mw	molecular weight
n	refractive index
NHS	N-hydroxy succinimide
NSB	non-specific binding
OD	optical density
PBS	phosphate buffered saline (buffer)
PDMS	polydimethylsiloxane
PMT	photo multiplier tube
PS	polystyrene
PSA	prostate specific antigen
PSP	plasmon surface polariton
RaG	rabbit anti-goat antibody
RaM	rabbit anti-mouse antibody
RC	reference channel
rpm	revolutions per minute
RU	resonance unit
S ₀ , S ₁	singlet electronic state of a molecule
SA	streptavidin
SAM	self-assembled monolayer
SD	standard deviation
SDS	sodium dodecyl sulfate
SERS	surface enhanced Raman spectroscopy
SNR	signal-to-noise ratio
SPDS	surface plasmon diffraction sensor
SPFM	surface plasmon fluorescence microscopy
SPFS	surface plasmon fluorescence spectroscopy
SP, SPP	surface plasmon polariton
SPR	surface plasmon resonance
TE	transversal electric (s-) polarization
TIR	total internal reflection
TIRF	total internal reflection fluorescence
TM	transversal magnetic (p-) polarization
μCP	micro-contact printing
UV	ultraviolet

8.2 List of Figures

<i>Figure 1.1: The advantages and disadvantages of labeling and label-free biosensing techniques.</i>	2
<i>Figure 2.1: The charges and the electromagnetic field of SPs propogating on a surface.....</i>	6
<i>Figure 2.2: The dispersion relation.....</i>	9
<i>Figure 2.3: Prism coupling geometries.....</i>	11
<i>Figure 2.4: Schematic picture of an incident, a reflected and a transmitted transverse magnetic polarized plane wave at an interface.....</i>	12
<i>Figure 2.5: Representation of SPR coupling via a sinusoidal diffraction grating.....</i>	13
<i>Figure 2.6: Simulation curves of the reflectivity and the relative field intensity as a function of the light incident angle on three-phase systems.....</i>	15
<i>Figure 2.7: Sketch of a reflective diffraction of an incident light by a surface grating structure .</i>	17
<i>Figure 2.8: Simplified Jablonski diagram.....</i>	20
<i>Figure 2.9: Schematic example of energy transfer efficiency dependent on the distance of donor-acceptor.....</i>	22
<i>Figure 2.10: Schematic drawing of a fluorophore positioned close to a metal/dielectric interface</i>	23
<i>Figure 2.11: A simple model for a biomolecular interaction at the solid/water interface.</i>	26
<i>Figure 2.12: Schematic examples of: a typical interaction analysis involving an association and a dissociation process, an equilibrium analysis based on a 1:1 Langmuir model.....</i>	28
<i>Figure 3.1: Surface plasmon spectrometer set-up including various extensions.....</i>	32
<i>Figure 3.2: Surface plasmon diffraction set-up.</i>	33
<i>Figure 3.3: A homemade flow cell</i>	34
<i>Figure 3.4: The SPR time responses of the homemade flow cell upon sample exchanges</i>	35
<i>Figure 3.5: Schematic of the labeling of protein with Alexa Fluor 647 dye with a succinimidyl ester moiety.....</i>	36
<i>Figure 3.6: Highly ordered monolayer of alkanethiolate formed on a gold surface.....</i>	38
<i>Figure 3.7: Mixed monolayer of biotin- and EG (spacer)- thiol.....</i>	39
<i>Figure 3.8: μCP procedure.....</i>	40
<i>Figure 3.9: Cross-sectional analysis of PDMS stamps.....</i>	41
<i>Figure 3.10: Optical microscopic images of the copper grids used in this study.....</i>	42
<i>Figure 4.1: Schematic drawing of the interfacial molecular architectures for direct and indirect detection</i>	45

<i>Figure 4.2: Resistance of EG SAMs and mixed SAMs ($\chi = 0.1$) to the nonspecific adsorption....</i>	<i>47</i>
<i>Figure 4.3: Example of repetitive regenerations of bound 2F5 by SDS solution</i>	<i>49</i>
<i>Figure 4.4: The effect of the flow rate on the binding profiles of L2F5.....</i>	<i>50</i>
<i>Figure 4.5: Representation of avidity controlled interaction between an antibody and its surface-coupled antigen</i>	<i>51</i>
<i>Figure 4.6: Comparison of the performance of AF and Cy5 labeled secondary antibodies..</i>	<i>53</i>
<i>Figure 4.7: Overlay of SPR and fluorescence results obtained on different mixed SAM surfaces..</i>	<i>55</i>
<i>Figure 4.8: The end-point results using the direct and the indirect detection schemes.....</i>	<i>58</i>
<i>Figure 4.9: Sensitivity evaluations of SPFS on planar surfaces.....</i>	<i>60</i>
<i>Figure 4.10: A layer-by-layer model built by biotin-streptavidin interaction.</i>	<i>61</i>
<i>Figure 4.11: Schematic drawing of the hIL-8 binding experiments performed on a supra-molecular architecture.</i>	<i>63</i>
<i>Figure 4.12: hIL8-Cy5 binding assay on its Fab surfaces.....</i>	<i>64</i>
<i>Figure 5.1: Schematic of SPFS immunoassays.</i>	<i>69</i>
<i>Figure 5.2: SPFS measurement with the CM5 chip.....</i>	<i>71</i>
<i>Figure 5.3: Fresnel 4-layer (prism, gold, protein, water) simulation curves for the Biacore and the SPFS reflectivity measurements.</i>	<i>72</i>
<i>Figure 5.4: Typical immobilization curve of α-MIG1 to a dextran surface..</i>	<i>74</i>
<i>Figure 5.5: Immobilization of 2F9.1 on the dextran matrix and a planar lipoic acid modified surface.</i>	<i>75</i>
<i>Figure 5.6: Working curves for LOD evaluation.</i>	<i>76</i>
<i>Figure 5.7: Dose-response curves of the different surfaces with different 2F9.1 loading levels... ..</i>	<i>77</i>
<i>Figure 5.8: Double-logarithmic plot of the dose-response curve of the AF-RaM binding to the dextran surface loaded with highest 2F9.1 level (1.51 degree)</i>	<i>78</i>
<i>Figure 5.9: Fluorescence intensity upon the injection of sample solutions with aM concentrations of AF-RaM.....</i>	<i>79</i>
<i>Figure 5.10: Angular scan curves of SPR and fluorescence.....</i>	<i>80</i>
<i>Figure 5.11: A direct comparison with Biacore 3000 instrument.....</i>	<i>81</i>
<i>Figure 5.12: Spectra recorded upon the binding of 33 pM AF-RaM on the 2F9.1 surface.....</i>	<i>82</i>
<i>Figure 5.13: SPFM assay on dextran surface patterned by UV-lithography.</i>	<i>83</i>
<i>Figure 5.14: UV-VIS spectrum of the Alexa Fluor 647 labeled detection antibody - LM86506M and the covalent immobilization of the capture antibody M37230M to the dextran matrix</i>	<i>85</i>
<i>Figure 5.15: Experimental efforts to learn the affinity picture of the sandwich PSA assay.</i>	<i>87</i>

<i>Figure 5.16: Demonstration of an SPFS based sandwich f-PSA immunoassay in both buffer and human plasma.....</i>	<i>88</i>
<i>Figure 5.17: Dose-response curve of the PSA assay in plasma with CMD.....</i>	<i>91</i>
<i>Figure 6.1: Schematic drawing of two types of diffraction sensors based on TIR and ATR modes, respectively.....</i>	<i>94</i>
<i>Figure 6.2: SPM images for PS patterns on Au surfaces and the cross-sectional analysis of PS patterns.....</i>	<i>95</i>
<i>Figure 6.3: Optical photographs of the diffraction patterns generated by various PS patterns on Au surfaces.....</i>	<i>96</i>
<i>Figure 6.4: The diffraction signals obtained from PS patterns on Au and glass surfaces and the angular dependence of the SPR reflectivity and the diffraction intensity of different diffraction orders.....</i>	<i>96</i>
<i>Figure 6.5: Simulations for the diffraction pattern of two kinds of surface periodic structures, both having the same periodicity and contrast while different line widths.....</i>	<i>98</i>
<i>Figure 6.6: SPM angular analysis for pattern A and pattern B treated with the anti-biotin antibody.....</i>	<i>99</i>
<i>Figure 6.7: Diffraction angular scans obtained on the patterned surfaces with and without the binding of the anti-biotin.....</i>	<i>100</i>
<i>Figure 6.8: Revealing of the quadratic signal dependence of the diffraction detection.....</i>	<i>101</i>
<i>Figure 6.9: Normalized desorption curves for the surface biotin density determination.....</i>	<i>103</i>
<i>Figure 6.10: Directly compare the detection limit of the SPR and SP-enhanced diffraction sensor.....</i>	<i>106</i>
<i>Figure 6.11: Temperature variation study for both SPR- and diffraction modes.....</i>	<i>107</i>
<i>Figure 6.12: The diffraction detection of hCG.....</i>	<i>108</i>
<i>Figure 6.13: Diffraction kinetic curves of the SA and DNA probe binding.....</i>	<i>112</i>
<i>Figure 6.14: Kinetic curves of hybridization of different DNA targets.....</i>	<i>113</i>
<i>Figure 6.15: Kinetic curves of the equilibrium titrations of T15-0, T15-1.....</i>	<i>115</i>
<i>Figure 6.16: The equilibrium signals of titrations with T15-0 and T15-1.....</i>	<i>116</i>
<i>Figure 6.17: Influence of the probe density on the hybridization efficiency of 15 mer targets ...</i>	<i>117</i>

8.3 List of Tables

Table 3.1: Commercial instruments equipped with flow cells and liquid handling systems..... 35

Table 4.1: Kinetic and affinity parameters obtained from the Cy5-hIL8/Fab interaction curves. 65

Table 5.1: Comparison of some instrumental parameters of the two SPR set-ups 72

Table 6.1: DNA oligonucleotide sequences used in this study. 111

Table 6.2: In-depth analysis of DNA hybridization by diffraction detection 114

8.4 Bibliography

- [1] (A) Scheller, F. W., Wollenberger, U., Warsinke A., and Lisdat, F. (2001) Research and development in biosensors. *Curr. Opin. Biotechnol.*, 12, 35–40.
(B) Ziegler, C. and Göpel, W. (1998) Biosensor development. *Curr. Opin. Chem. Biol.*, 2, 585-591.
- [2] (A) Zhu, H. et al. (2001) Global analysis of protein activities using proteome chips. *Science*. 293, 2101-2105.
(B) Jocelyn, H. N. and Leodevico, L. I. (2003) Biochips beyond DNA: technologies and applications. *Biotechnology Annual Review*. 9, 1-149.
- [3] (A) (2001) A physical map of the human genome. *Nature*. 409, 934-941.
(B) (2001) The sequence of the human genome. *Science*. 291, 1304-1351.
- [4] Buerk, D. G. *Biosensors* (Technomic Publishing AG, Lancaster, USA, 1992).
- [5] Cooper, M. A. (2003) Label-free screening of bio-molecular interactions. *Anal. Bioanal. Chem.* 377, 834-842.
- [6] McDonnell, J. M. (2001) Surface plasmon resonance: towards an understanding of the mechanisms of biological molecular recognition. *Curr. Opin. Chem. Biol.*, 5, 572–577.
- [7] Doyle, M. L. (1997) Characterization of binding interactions by isothermal titration calorimetry. *Curr. Opin. Biotechnol.* 8, 31-35.
- [8] (A) Weiss, S. (1999) Fluorescence spectroscopy of single biomolecules. *Science*. 283, 1676-1683.
(B) Yeung, E. S. (2001) High-throughput single molecule screening of DNA and proteins. *The Chemical Record*, 1, 123–139.
- [9] Nam, J-M., Thaxton, C. S., Mirkin, C. A. (2003) Nanoparticle-based bio-bar codes for the ultrasensitive detection of proteins. *Science*. 301, 1884-1886.
- [10] Raether, H. (1988) *Surface plasmons on smooth and rough surfaces and on gratings*, Springer-Verlag; Berlin.
- [11] (A) Pockrand, I., Swalen, J.D., Gordon, J.G., Philpott, M.R. (1978) Surface plasmon spectroscopy of organic monolayer assemblies, *Surface Sci.* 74, 237–244.
(B) Gordon, J.G., Ernst, S. (1980) Surface plasmons as a probe of the electrochemical interface, *Surface Sci.* 101, 499–506.
- [12] Jönsson, U., Fägerstam, L., Ivarsson, B. et al. (1991) Real-time biospecific interaction analysis using surface plasmon resonance and a sensor chip technology, *Biotechniques*. 11, 620–627.
- [13] Campion, A., Kambhampati, P. (1998) Surface-enhanced Raman scattering. *Chem. Soc. Rev.*, 27, 241-250.
- [14] Liebermann, T., Knoll, W. (2000) Surface-plasmon field-enhanced fluorescence spectroscopy. *Colloid Surf. A*. 171, 115–130.
- [15] McGilp, J. F. (1999) Second-harmonic generation at semiconductor and metal surfaces. *Surf. Rev. Lett.*, 6, 529-558.
- [16] Osawa, M. (2001) Surface-enhanced infrared absorption. *Top. Appl. Phys.*, 81, 163-187.
- [17] (A) Rothenhäusler, B. ; Knoll, W. (1987) Plasmon surface polariton fields versus TIR evanescent waves for scattering experiments at surfaces. *Opt. Commun.*, 63, 301-304.
(B) Rothenhäusler, B. ; Knoll, W. (1987) Total internal diffraction of plasmon surface-polaritons. *Appl. Phys. Lett.*, 51, 783-785.
- [18] Rothenhäusler, B., Knoll, W. (1988) Surface-Plasmon Microscopy. *Nature*, 332, 615-617.

- [19] (A) Smith, E. A., Corn, R. M. (2003) Surface plasmon resonance imaging as a tool to monitor biomolecular interactions in an array based format. *Appl. Spectrosc.*, 57, 320A-332A.
 (B) Grigorenko, A. N., Beloglazov, A. A., Nikitin, P. I., Kuhne, C., Steiner, G., Salzer, R. (2000) Dark-field surface plasmon resonance microscopy, *Opt. Commun.*, 174, 151-155.
 (C) Guedon, P., Livache, T., Martin, F., Lesbire, F., Roget, A., Bidan, G., Levy, Y. (2000) Characterization and optimization of a real-time, parallel, label-free, polypyrrole-based DNA sensor by surface plasmon resonance imaging. *Anal. Chem.*, 72, 6003-6009.
- [20] <http://www.appliedbiosystems.com/>
- [21] (A) Ishida A, Sakata Y, Majima T. (1998) Surface plasmon excitation of a porphyrin covalently linked to a gold surface, *Chem. Comm.* (1), 57-58.
 (B) Brown, C. W., Li, Y., Seelenbinder, J. A., Pivarnik, P., Rand, A. G., Letcher, S. V., Gregory, O. J., Platek, M. J. (1998) Immunoassays based on surface enhanced infrared absorption spectroscopy. *Anal. Chem.*, 70, 2991-2996.
- [22] (A) Liebermann, T., Knoll, W., Sluka, P., Herrmann, R. (2000) *Colloid Surf. A.*, 169, 337-350.
 (B) Neumann, T., Johansson, M-L., Kambhampati, D., Knoll, W. (2002) Surface-plasmon fluorescence spectroscopy. *Adv. Func. Mate.* 12, 575-586.
 (C) Kambhampati, D., Nielsen, P. E., Knoll, W. (2001) Investigating the kinetics of DNA-DNA and PNA-DNA interactions using surface plasmon resonance-enhanced fluorescence spectroscopy. *Biosens. Bioelectron.*, 16, 1109-1118.
- [23] Wood, R. W. (1902) On a remarkable case of uneven distribution of light in a diffraction grating spectrum. *Philosophical Magazine*, 4, 396.
- [24] Ritchie, R. H. (1957) Plasma losses by fast electrons in thin films. *Phys. Rev.*, 106, 874-881.
- [25] (A) <http://www.mpip-mainz.mpg.de/documents/akkn/soft/winspall2.zip>
 (B) <http://corndog.chem.wisc.edu/fresnel/fcform.html>
- [26] Karthe, W., Müller, R. *Integrierte Optik* (Akademische Verlagsgesellschaft Geest und Portig, Leipzig, 1991).
- [27] Otto, A. (1968) Excitation of nonradiative surface plasma waves in silver by the method of frustrated total reflection. *Z. Phys.*, 216, 398.
- [28] Kretschmann, E. & Raether, H. (1968) Radiative decay of nonradiative surface plasmons excited by light. *Z. Naturforsch. A*, 23, 2135-2136.
- [29] Kazandjian, L. (1996). Rayleigh methods applied to electromagnetic scattering from gratings in general homogenous media. *Phys. Rev. E* 54, 6902-6815.
- [30] Knoll, W. In R.E. Hummel and P. Wißmann, (Eds.), *Handbook of optical properties band II, Optics of small particles, interfaces, and surfaces* 373-399. CRC Press Boca Raton, New York, London, Tokyo, 1997.
- [31] Peterlinz, K. A., Georgiadis, R. (1996) Two-color approach for determination of thickness and dielectric constant of thin films using surface plasmon resonance spectroscopy. *Opt. Commun.*, 130, 260-266.
- [32] (A) Tien, P. K. (1977) Integrated-optics and new wave phenomena in optical-waveguides. *Reviews of Modern Physics* 49, 361-420.
 (B) Knoll, W. (1998) Interfaces and thin films as seen by bound electromagnetic waves. *Annu. Rev. Phys. Chem.* 49, 569-638.
- [33] Stenberg, E, Persson, B., Roos, H, Urbaniczky, C. (1991) Quantitative-determination of surface concentration of protein with surface-plasmon resonance using radiolabeled proteins. *J. Colloid Interface Sci.*, 143, 513-526.
- [34] Ekgasit, S., Thammacharoen, C., Knoll, W. Surface Plasmon Resonance Spectroscopy Based on Evanescent Field Treatment. *Anal. Chem.*, 76, 561-568, 2004.

- [35] Nemetz, A., Knoll, W. (1996) Raman spectroscopy and microscopy with plasmon surface polaritons, *J. Raman Spectrosc.* 27, 587–592.
- [36] Beckmann, P., Spizzichino, A. The scattering of electromagnetic waves from rough surface, Pergamon, New York, (1963).
- [37] Rice, S. O. (1951) *Commun. Pure Appl. Math.*, Vol 4, 351.
- [38] Rayleigh, Lord. *Proc. R. Soc.*, A79-399 (1907).
- [39] Church, E. L., Zavada, J. M. (1975) Residual surface roughness of diamond-turned optics. *Appl. Opt.*, 14, 1788.
- [40] Nelson, K. A.; Casalegno, R.; Miller, R. J. D.; Fayer, M. D. (1982) Laser-induced excited-state and ultrasonic wave gratings - amplitude and phase grating contributions to diffraction. *J. Chem. Phys.*, 77, 1144-1152.
- [41] John M. Cowley. (1975) *Diffraction Physics*. Elsevier Science Publisher B. V. New York.
- [42] (A) Valeur, B. *Molecular Fluorescence Principles and Applications*; Wiley-VCH: Weingheim, 2002.
(B) Lakowicz, J. R. *Principles of Fluorescence Spectroscopy*, 2nd ed.; Kluwer Academic/Plenum Publishers: New York, 1999.
- [43] Macdonald, R. I. (1990) Characteristics of self-quenching of the fluorescence of lipid-conjugated rhodamine in membranes. *J. Biol. Chem.*, 265, 13533-13539.
- [44] Tyagi, S., Kramer, F. R. (1996) Molecular beacons: probes that fluoresce upon hybridization. *Nat. Biotechnol.*, 14, 303-308.
- [45] Axelrod, D., Burghardt, T.P., Thompson, N.L. (1984) Total internal-reflection fluorescence, *Annu. Rev. Biophys. Bio.*, 13, 247-268.
- [46] Plowman, T. E., Reichert, W. M., Peters, C. R., Wang, H. K., Christensen, D. A., Herron, J. N. (1996) Femtomolar sensitivity using a channel-etched thin film waveguide fluoroimmunosensor. *Biosens. Bioelectron.*, 11, 149-160.
- [47] Tamm LK: Total internal reflection fluorescence microscopy - In *Optical Microscopy: Emerging Methods and Applications*. Edited by Herman B, Lemasters JJ. New York: Academic Press, (1993), 295-337.
- [48] Barnes, W. L. (1998) Fluorescence near interfaces: the role of photonic mode density. *J. Mod. Optic.*, 45, 661-699.
- [49] Knobloch, H., Brunner, H., Leitner, A., Aussenegg, F., and Knoll, W. (1993) Probing the evanescent field of propagating plasmon surface-polaritons by fluorescence and Raman spectroscopies. *J. Chem. Phys.*, 98, 10093-10095.
- [50] Schuckannu, P. (1997) Use of surface plasmon resonance to probe the equilibrium and dynamic aspects of interactions between biological macromolecules. *Rev. Biophys. Biomol. Struct.* 26, 541–566.
- [51] P. W. Atkins. *Physical Chemistry*. 6th edition, 1998, 858-859.
- [52] Myszka, D. G., Morton, T. A., Doyle, M. L., Chaiken, I. M. (1997) Kinetic analysis of a protein antigen-antibody interaction limited by mass transport on an optical biosensor. *Biophys. Chem.*, 6, 127-137.
- [53] Morton, T. A., Myszka, D. G., Chaiken, I. M. (1995) Interpreting complex binding kinetics from optical biosensors: a comparison of analysis by linearization, the integrated rate equation, and numerical integration. *Anal. Biochem.*, 227, 176-185.
- [54] (A) MacKenzie, C. R., Hiramata, T., Deng, S. J., Bundle, D. R., Narang, S. A., Young, N. M. (1996) Analysis by surface plasmon resonance of the influence of valence on the ligand binding affinity and kinetics of an anti-carbohydrate antibody. *J. Biol. Chem.*, 271, 1527-1533.

- (B) Kalinin, N. L., Ward, L. D., Winzor, D. J. (1995) Effects of solute multivalence on the evaluation of binding constants by biosensor technology: studies with concanavalin A and interleukin-6 as partitioning proteins. *Anal. Biochem.*, 228, 238-244.
- (C) Glaser, R. W. (1993) Antigen-antibody binding and mass transport by convection and diffusion to a surface: a two-dimensional computer model of binding and dissociation kinetics. *Anal. Biochem.*, 213, 152-161.
- (D) Karlsson, R., Roos, H., Fagerstam, L., Persson, B. (1994) Kinetic and concentration analysis using BIA technology. *Methods*, 6, 99-110.
- (E) O'Shannessy, D., Winzor, D. J. (1996) Interpretation of deviations from pseudo-first-order kinetic behavior in the characterization of ligand binding by biosensor technology. *Anal. Biochem.*, 236, 275-283.
- [55] (A) Knoll, W., Pirwitz, G., Tamada, K., Offenhausser, A., Hara, M. (1997) Supramolecular interfacial architectures for controlled electron transfer. *J. Electroanal. Chem.* 438, 199-205.
 (B) Badia, A., Arnold, S., Scheumann, V., Zizlsperger, M., Mack, J., Jung, G., Knoll, W. (1999) Probing the electrochemical deposition and/or desorption of self-assembled and electropolymerizable organic thin films by surface plasmon spectroscopy and atomic force microscopy. *Sens. Actuator B.*, 54, 145-165.
- [56] Sjolander, S., Urbaniczky, C. (1991) Integrated fluid handling-system for biomolecular interaction analysis. *Anal. Chem.* 63, 2338-2345.
- [57] Myszka, D. G. (1997) Kinetic analysis of macromolecular interactions using surface plasmon resonance biosensors. *Curr. Opin. Biotech.*, 8, 50-57.
- [58] Van der Merwe, P. A. (1994) Human cell-adhesion molecule CD2 binds CD58 (LFA-3) with a very low affinity and an extremely fast dissociation rate but does not bind CD48 or CD59. *Biochemistry*, 33, 10149-10160.
- [59] (A) <http://www.probes.com>
 (B) Berlier, J. E., et al. (2003) Quantitative comparison of long-wavelength Alexa Fluor dyes to Cy dyes: Fluorescence of the dyes and their bioconjugates. *J. Histochem. Cytochem.*, 51, 1699-1712.
- [60] Whitesides, G. M., Laibinis, P. E. (1990) Wet chemical approaches to the characterization of organic surfaces: self-assembled monolayers, wetting, and the physical-organic chemistry of the solid-liquid interface. *Langmuir*, 6, 87-96.
- [61] (A) Lahiri, J., Isaacs, L., Tien, J., Whitesides, G. M. (1999) A strategy for the generation of surfaces presenting ligands for studies of binding based on an active ester as a common reactive intermediate: A surface plasmon resonance study. *Anal. Chem.* 71, 777-790.
 (B) Spinke, J., Liley, M., Schmitt, F. J., Guder, H. J., Angermaier, L., Knoll, W. (1993) Molecular recognition at self-assembled monolayers - optimization of surface functionalization. *J. Chem. Phys.* 99, 7012-7019.
- [62] (A) Bain, C. D., Evall, J., Whitesides, G. M. (1989) Formation of monolayers by the coadsorption of thiols on gold: variation in the head group, tail group, and solvent. *J. Am. Chem. Soc.*, 111, 7155-7164.
 (B) Bain, C.D., Whitesides, G. M. (1989) Formation of monolayers by the coadsorption of thiols on gold: variation in the length of the alkyl chain, *J. Am. Chem. Soc.*, 111, 7164-7175.
- [63] (A) Zhang, Z. J., Imae, T. (2001) Hydrogen-bonding stabilized self-assembled monolayer film of a functionalized diacid, protoporphyrin IX zinc(II), onto a gold surface. *Nano. Lett.*, 1, 241-243.
 (B) Clegg, R. S., Hutchison, J. E. (1996) Hydrogen-bonding, self-assembled monolayers: ordered molecular films for study of through-peptide electron transfer. *Langmuir*, 12, 5239-5243.
- [64] Xia, Y. N., Whitesides, G. M. (1998) Soft lithography. *Angew. Chem.-Int. Edit.* 37, 551-575.
- [65] Dearo, J. A., Gupta, R., Heeger, A. J., Buratto, S. K. (1999) Nanoscale oxidative patterning and manipulation of conjugated polymer thin films. *Synthetic. Met.* 102, 865-868.
- [66] Norrod, K. L., Rowlen, K. L., (1998) Ozone-induced oxidation of self-assembled decanethiol: contributing mechanism for "photooxidation"? *J. Am. Chem. Soc.*, 120, 2656-2657.
- [67] Roy, S., Kim, J-H., Kellis, J. T., Poulouse, J. A. J. Robertson, C. R., Gast. A. P. (2002) Surface plasmon resonance/surface plasmon enhanced fluorescence: an optical technique for the detection of multicomponent macromolecular adsorption at the solid liquid interface. *Langmuir*, 18, 6319-6323.

- [68] Vasilev, K., Knoll, W., Kreitera, M. Fluorescence intensities of chromophores in front of a thin metal film. *J. Chem. Phys.* accepted.
- [69] (A) Merrill, E. W. *Poly(ethylene glycol) Chemistry*; Harris, J. M., Ed.; Plenum Press: New York, 1992; p 199.
(B) Gölander, C.-G., et al. *Poly(ethylene glycol) Chemistry: Biotechnical and Biomedical Applications*; Harris, J. M., Ed.; Plenum Press: New York, 1992; p 221.
- [70] (A) Wang, R. L. C., Kreuzer, H. J., Grunze, M. (2000) The interaction of oligo(ethylene oxide) with water: a quantum mechanical study. *Phys. Chem. Chem. Phys.*, 2, 3613- 3622.
(B) Pertsin, A. J., Grunze, M. (2000) Computer simulation of water near the surface of oligo(ethylene glycol)-terminated alkanethiol self-assembled monolayers. *Langmuir*, 16, 8829- 8841.
- [71] Engvall, E., Perlmann, P. (1972) Enzyme-linked immunosorbent assay, ELISA. III. Quantitation of specific antibodies by enzyme-labeled anti-immunoglobulin in antigen coated tubes. *J. Immunol.* 109, 129–135.
- [72] Wedege, E., Svenneby, G. (1986) Effects of the blocking agents bovine serum albumin and Tween 20 in different buffers on immunoblotting of brain proteins and marker proteins. *J. Immunol. Methods* 88, 233–237.
- [73] Zhang, M. Q., Ferrari, M. (1997) Reduction of albumin adsorption onto silicon surfaces by Tween 20. *Biotechnol. Bioeng.* 56, 618-625.
- [74] P. W. Atkins. *Physical Chemistry*. 6th edition, 1998, 458.
- [75] Reynolds, J.A., Tanford, C. (1970) Gross conformation of protein-sodium dodecyl sulfate complexes. *J. Biol. Chem.* 245, 5161.
- [76] (A) Sigal, G. B., Mrksich, M., Whitesides, G. M. (1998) Effect of surface wettability on the adsorption of proteins and detergents. *J. Am. Chem. Soc.*, 120, 3464-3473.
(B) Sigal, G. B., Mrksich, M., Whitesides, G. M. (1997) Using surface plasmon resonance spectroscopy to measure the association of detergents with self-assembled monolayers of hexadecanethiolate on gold. *Langmuir*, 13, 2749-2755.
- [77] Arakawa, T., Timasheff, S.N. (1984) Protein stabilization and destabilization by guanidinium salts. *Biochemistry*, 23, 5924-5929.
- [78] Duschl, C. Sevin-Landais, A. F., Vogel, H. (1996) Surface engineering: optimization of antigen presentation in self- assembled monolayers. *Biophys. J.*, 70, 1985-1995.
- [79] Müller, K. M., Arndt, K. M., Plückthun, A. (1998) Model and simulation of multivalent binding to fixed ligands. *Anal. Biochem.*, 261, 149-158.
- [80] Bamdad, C. (1998) The use of variable density self-assembled monolayers to probe the structure of a target molecule. *Biophys. J.*, 75, 1989-1996.
- [81] Folkers, J. P., Laibinis, P. E., Whitesides, G. M. (1992) Self-assembled monolayers of alkanethiols on gold - comparisons of monolayers containing mixtures of short-chain and long-chain constituents with CH₃ and CH₂OH terminal groups. *Langmuir*. 8, 1330-1341.
- [82] (A) Schobel, U., Egelhaaf, H., Gauglitz, G. (2000) Mechanisms of fluorescence quenching in donor-acceptor labeled antibody-antigen conjugates. *J. Fluoresc.*, 10, 147-154.
(B) Gruber, H. J., Hahn, C. D., et al. (2000) Anomalous fluorescence enhancement of Cy3 and Cy3.5 versus anomalous fluorescence loss of Cy5 and Cy7 upon covalent linking to IgG and noncovalent binding to avidin. *Bioconjugate. Chem.*, 11, 696-704.
- [83] Roberts, K. E., O'Keeffe, A. K., Lloyd, C. J., Clarke, D. J. (2003) Selective dequenching by photobleaching increases fluorescence probe visibility. *J. Fluoresc.*, 13, 513-517.
- [84] Gajraj, A., Ofoli, R. Y. (2000) Effect of extrinsic fluorescent labels on diffusion and adsorption kinetics of proteins at the liquid-liquid interface. *Langmuir*, 16, 8085-8094.

- [85] (A) Marquart, M., Deisenhofer, J., Huber, R., Palm, W. (1980) Crystallographic refinement and atomic models of the intact immunoglobulin molecule KOL and its antigen-binding fragment at 3.0-Å and 1.9-Å resolution. *J. Mol. Biol.*, 141, 369-391.
(B) Green, N. M. *Advances in Immunology*. Academic Press, New York, 1969, 1-30.
- [86] Nelles, G., Schönherr, H., Jaschke, M., Wolf, H., Schaub, M., Küther, J., Tremel, W., Bamberg, E., Ringsdorf, H., Butt, H. -J. (1998) Two-dimensional structure of disulfides and thiols on gold(111). *Langmuir*, 14, 808-815.
- [87] Bourdillon, C., Demaille, C., Moiroux, J. Saveant, J-M. (1994) Step-by-step immunological construction of a fully active multilayer enzyme electrode. *J. Am. Chem. Soc.*, 116, 10328-10329.
- [88] Hoshi, T., Anzai, J-I, Osa, T. (1995) Controlled deposition of glucose oxidase on platinum electrode based on an avidin/biotin system for the regulation of output current of glucose sensors. *Anal. Chem.* 34, 770-774.
- [89] Anzai, J-I., Kobayashi, Y., Nakamura, N., Hoshi, T. (2000) Use of Con A and mannose-labeled enzymes for the preparation of enzyme films for biosensors, *Sens. Actuators B.*, 65, 94-96.
- [90] Cui, X. Q., Pei, R. J., Wang, X. Z., Yang, F., Ma, Y., Dong, S. J., Yang, X. R. (2003) Layer-by-layer assembly of multilayer films composed of avidin and biotin-labeled antibody for immunosensing. *Biosens. Bioelectron.*, 18, 59-67.
- [91] Knoll, W., Zizlsperger, M., Liebermann, T., Arnold, S., Badia, A., Liley, M., Piscevic, D., Schmitt, F. J., Spinke, J. (2000) Streptavidin arrays as supramolecular architectures in surface-plasmon optical sensor formats. *Colloid Surf. A.*, 161, 115-137.
- [92] Yu, F., Yao, D., Knoll, W. (2003) Surface plasmon field-enhanced fluorescence spectroscopy studies of the interaction between an antibody and its surface-coupled antigen. *Anal. Chem.* 75, 2610-2617.
- [93] Mullett, W. M., Lai, E. P., Yeung, J. M. (2000) Surface plasmon resonance-based immunoassays. *Methods*, 22, 77-91.
- [94] Cush, R., Cronin, J. M., Stewart, W. J., Maule, C. H., Molloy, J., Goddard, N. J. (1993) The resonant mirror - a novel optical biosensor for direct sensing of biomolecular interactions .1. Principle of operation and associated instrumentation. *Biosens. Bioelectron.*, 8, 347-353.
- [95] Ostroff, R. M., Maul, D., Bogart, G. R., Yang, S., Christian, J., Hopkins, D., Clark, D., Trotter, B., Moddel, G. (1998) Fixed polarizer ellipsometry for simple and sensitive detection of thin films generated by specific molecular interactions: applications in immunoassays and DNA sequence detection. *Clin. Chem.* 44, 2031-2035.
- [96] Yun, K., Kobatake, E., Haruyama, T., Laukkanen, M. L., Keinanen, K., Aizawa, M. (1998) Use of a quartz crystal microbalance to monitor immunoliposome-antigen interaction. *Anal. Chem.* 70, 260-264.
- [97] Brecht, A., Piehler, J., Lang, G., Gauglitz, G. (1995) A direct optical immunosensor for atrazine detection. *Analytica Chimica Acta* 311, 289-299.
- [98] Wu, G. H., Datar, R. H., Hansen, K. M., Thundat, T., Cote, R. J., Majumdar, A. (2001) Bioassay of prostate-specific antigen (PSA) using microcantilevers. *Nat. Biotechnol.*, 19, 856-860.
- [99] Adamczyk, M., Moore, J. A., Yu, Z. G. (2000) Application of surface plasmon resonance toward studies of low-molecular-weight antigen-antibody binding interactions. *Method Enzymol.*, 20, 319-328.
- [100] Attridge, J. W., Daniels, P. B., Deacon, J. K., Robinson, G. A., Davidson, G. P. (1991) Sensitivity enhancement of optical immunosensors by the use of a surface-plasmon resonance fluoroimmunoassay. *Biosens. Bioelectron.*, 6, 201-214.
- [101] Malicka, J., Gryczynski, I., Fang, J., Kusba, J., Lakowicz, J. R. (2003) Increased resonance energy transfer between fluorophores bound to DNA in proximity to metallic silver particles. *Anal. Chem.* 315, 160-169.

- [102] Golze, S. Oberflächengebundene Polymermonolagen für die Herstellung von DNA-Chips. Dissertation of Uni. Mainz, 2001.
- [103] Zhang, Z. H., Chen, Q., Knoll, W., Foerch, R., Holcomb, R., Roitman, D. (2004) Plasma polymer film structure and DNA probe immobilization. *Macromolecules*, 36, 7689-7694.
- [104] Löfås, S.; Johnsson, B. (1990) A novel hydrogel matrix on gold surfaces in surface plasmon resonance sensors for fast and efficient covalent immobilisation of ligands. *J. Chem. Soc. Chem. Commun.*, 21, 1526-1528.
- [105] Stenberg, E., Persson, B., Roos, H., Urbaniczky, C. (1991) Quantitative-determination of surface concentration of protein with surface-plasmon resonance using radiolabeled proteins. *J. Colloid. Interf. Sci.* 143, 513-526.
- [106] Berggren, C., Johansson, G. (1997) Capacitance measurements of antibody-antigen interactions in a flow system. *Anal. Chem.* 69, 3651-3657.
- [107] Karlsson, R., Fagerstam, L., Nilshans, H., Persson, B. (1993) Analysis of active antibody concentration - separation of affinity and concentration parameters. *J. Immunol. Methods* 166, 75-84.
- [108] Liebermann, T., Knoll, W. (2003) Parallel multispot detection of target hybridization to surface-bound probe oligonucleotides of different base mismatch by surface-plasmon field-enhanced fluorescence microscopy. *Langmuir*, 19, 1567-1572.
- [109] Lilja, H. (1985) A kallikrein-like serine protease in prostatic fluid cleaves the predominant seminal-vesicle protein. *J. Clin. Invest.* 76, 1899-1903.
- [110] Lilja, H., Christensson, A., Dahlen, U., Matikainen, M.T., Nilsson, O., Pettersson, K., Lovgren, T. (1991) Prostate-specific antigen in serum occurs predominantly in complex with alpha-1-antichymotrypsin. *Clin. Chem.*, 37, 1618-1625.
- [111] Catalona, W. J., Smith, D. S. (1994) Comparison of different serum prostate-specific antigen measures for early prostate-cancer detection. *Cancer*, 74, 1516-1518.
- [112] Hudson, M. A., Bahnson, R. R., Catalona, W. J. (1989) Clinical use of prostate specific antigen in patients with prostate-cancer. *J. Urology.*, 142, 1011-1017.
- [113] P. W. Atkins. *Physical Chemistry*. 6th edition, 1998, 749.
- [114] P. W. Atkins. *Physical Chemistry*. 6th edition, 1998, 736.
- [115] Rosenson, R. S., McCormick, A., Uretz, E. F. (1996) Distribution of blood viscosity values and biochemical correlates in healthy adults. *Clin. Chem.*, 42, 1189-1195.
- [116] Acevedo, B., Perera, Y., Ruiz, M., Rojas, G., Benítez, J., Ayala, M., Gavilondo, J. (2002) Development and validation of a quantitative ELISA for the measurement of PSA concentration, *Clinica. Chimica. Acta.*, 317, 55-63.
- [117] Harma, H., Tarkkinen, P., Soukka, T., Lovgren, T. (2000) Miniature single-particle immunoassay for prostate-specific antigen in serum using recombinant Fab fragments. *Clin. Chem.*, 46, 1755-1761.
- [118] Grubisha, D. S., Lipert, R. J., Park, H.-Y., Driskell, J., Porter, M. D. (2003) Femtomolar detection of prostate-specific antigen: an immunoassay based on surface-enhanced Raman scattering and immunogold labels. *Anal. Chem.*, 75, 5936-5943.
- [119] (A) Soukka, T., Paukkunen, J., Härmä, H., Lönnberg, S., Lindroos, H., Lövgren, T. (2001) Supersensitive time-resolved immunofluorometric assay of free prostate-specific antigen with nanoparticle label technology. *Clin. Chem.*, 47, 1269-1278.
(B) Seto, Y., Iba, T., Abe, K. (2001) Development of ultra-high sensitivity bioluminescent enzyme immunoassay for prostate-specific antigen (PSA) using firefly luciferase. *Luminescence*, 16, 285-290.
- [120] (A) Hasegawa, M., Yamamoto, T., Kanazawa, A., Shiono, T., Ikeda, T. (1999) Photochemically induced dynamic grating by means of side chain polymer liquid crystals. *Chem. Mater.*, 11, 2764-2769.

- (B) Bailey, R. C., Hupp, J. T. (2002) Large-scale resonance amplification of optical sensing of volatile compounds with chemoresponsive visible-region diffraction gratings. *J. Am. Chem. Soc.*, 124, 6767-6774.
- (C) Nakajima, F., Hirakawa, Y., Kaneta, T., Imasaka, T. (1999) Diffractive optical chemical sensor based on light absorption. *Anal. Chem.*, 71, 2262-2265.
- [121] (A) Tsay, Y. G., Lin, C. I., Lee, J., Gustafson, E. K., Appelqvist, R., Maggini, P., Norton, R., Teng, N., Charlton, D. (1991) Optical biosensor assay (OBA). *Clin. Chem.*, 37, 1502-1505.
- (B) Goh, J. B., Loo, R. W., McAloney, R. A., Goh, M. C. (2002) Diffraction-based assay for detecting multiple analytes. *Anal. Bioanal. Chem.*, 374, 54-56.
- (C) Goh, J. B., Tam, P. L., Loo, R. W., Goh, M. C. (2003) A quantitative diffraction-based sandwich immunoassay. *Anal. Biochem.*, 313, 262-266.
- [122] (A) John, P. M., Davis, R., Cady, N., Czajka, J., Batt, C. A., Craighead, H. G. (1998) Diffraction-based cell detection using a microcontact printed antibody grating. *Anal. Chem.*, 70, 1108-1111.
- (B) Morhard, F., Pipper, J., Dahint, R., Grunze, M. (2000) Immobilization of antibodies in micropatterns for cell detection by optical diffraction. *Sens. Actuators B.*, 70, 232-242.
- [123] Bailey, R. C., Nam, J. M., Mirkin, C. A., Hupp, J. T. (2003) Real-time multicolor DNA detection with chemoresponsive diffraction gratings and nanoparticle probes. *J. Am. Chem. Soc.*, 125, 13541-13547.
- [124] Homola, J., Koudela, I., Yee, S. S. (1999) Surface plasmon resonance sensors based on diffraction gratings and prism couplers: sensitivity comparison. *Sens. Actuator B.*, 54, 16-24.
- [125] Fischer, B., Rothenhausler, B., Knoll, W. (1995) Surface-plasmon-enhanced diffraction orders in polymer gratings. *Thin solid films*, 258, 247-251.
- [126] (A) Ober, R. J., Ward, E. S. (1999) The choice of reference cell in the analysis of kinetic data using BIAcore. *Anal. Biochem.*, 271, 70-80.
- (B) Lu, H.B., Homola, J., Campbell, C.T., Nenninger, G.G., Yee, S.S., Ratner, B.D. (2001) Surface functionalization of dual-channel surface plasmon resonance biosensor by protein contact printing. *Sens. Actuators B.*, 74, 91-99.
- (C) Boozer, C., Yu, Q., Chen, S., Lee, C-Y., Homola, J., Yee, S. S., Jiang, S. (2003) Surface functionalization for self-referencing surface plasmon resonance (SPR) biosensors by multi-step self-assembly. *Sens. Actuators B.*, 90, 22-30.
- [127] Wiki, M., Gao, H., Juvet, M., Kunz, R.E. (2001) Compact integrated optical sensor system. *Biosensors Bioelectr.*, 16, 37-45.
- [128] Fritz, J., Baller, M. K., Lang, H. P., Rothuizen, H., Vettiger, P., Meyer, E., Guntherodt, H.-J., Gerber, Ch., Gimzewski, J. K. (2000) Translating biomolecular recognition into nanomechanics. *Science*, 288, 316-318.
- [129] Rothenhausler, B.; Knoll, W. (1987) On the influence of the propagation length of plasmon surface-polaritons in the visible energy-range for the optical characterization of heterogeneous thin-films. *Surf. Sci.*, 191, 585-594.
- [130] Grassi, J. H.; Georgiadis, R. M. (1999) Temperature-Dependent Refractive Index Determination from Critical Angle Measurements: Implications for Quantitative SPR Sensing. *Anal. Chem.*, 71, 4392-4396.
- [131] (A) Persson, B., Stenhag, K., Nilsson, P., Larsson, A., Uhlen, M. Nygren, P. (1997) Analysis of oligonucleotide probe affinities using surface plasmon resonance: a means for mutational scanning. *Anal. Biochem.*, 246, 34-44.
- (B) Sauer, M., Brecht, A., Charisse, K., Maier, M., Gerster, M., Stemmler, I., Gauglitz, G. Bayer, E. (1999) Interaction of chemically modified antisense oligonucleotides with sense DNA: a label-free interaction study with reflectometric interference spectroscopy. *Anal. Chem.*, 71, 2850-2857.
- (C) Peterson, A. W., Wolf, L. K. Georgiadis R. M. (2002) Hybridization of mismatched or partially matched DNA at surfaces. *J. Am. Chem. Soc.*, 124, 14601-14607.
- (D) Nelson, B. P., Grimsrud, T. E., Liles, M. R., Goodman, R. M., Corn, R. M. (2001) Surface plasmon resonance imaging measurements of DNA and RNA hybridization adsorption onto DNA microarrays. *Anal. Chem.*, 73, 1-7.
- (E) Watts, H. J., Yeung, D. Parkes, H. (1995) Real-Time detection and quantification of DNA hybridization by an optical biosensor. *Anal. Chem.*, 67, 4283-4289.
- [132] Wang, J. (2002) Electrochemical nucleic acid biosensors. *Anal. Chim. Acta.*, 469, 63-71.

- [133] Hook, F., Ray, A., Norden, B. Kasemo, B. (2001) Characterization of PNA and DNA immobilization and subsequent hybridization with DNA using acoustic-shear-wave attenuation measurements. *Langmuir*, 17, 8305-8312.
- [134] (A) Jordan, C. E., Frutos, A. G., Thiel, A. J. Corn, R. M. (1997) Surface plasmon resonance imaging measurements of DNA hybridization adsorption and streptavidin/DNA multilayer formation at chemically modified gold surfaces. *Anal. Chem.*, 69, 4939-4947.
(B) He, L., Musick, M. D., Nicewarner, S. R., Salinas, F. G., Benkovic, S. J., Natan, M. J. Keating, C. D. (2000) Colloidal Au-enhanced surface plasmon resonance for ultrasensitive detection of DNA hybridization. *J. Am. Chem. Soc.*, 122, 9071-9077.
- [135] Levicky, R., Herne, T. M., Tarlov, M. J. Satija, S. K. (1998) Using self-assembly to control the structure of DNA monolayers on Gold: a neutron reflectivity study. *J. Am. Chem. Soc.*, 120, 9787-9792.
- [136] (A) Steel, A. B., Herne, T. M. Tarlov, M. J. (1998) Electrochemical quantitation of DNA immobilized on gold. *Anal. Chem.*, 70, 4670-4677.
(B) Peterson, A. W., Heaton, R. J. Georgiadis R. M. (2001) The effect of surface probe density on DNA hybridization. *Nucleic Acids Res.*, 29, 5163-5168.

Acknowledgements

It is difficult to overstate my gratitude to my Ph.D. supervisor, Prof. Wolfgang Knoll, who has supported the work all the way along. He gave me the opportunity to work on such fascinating and pioneering topics. With his enthusiasm, his inspiration and his great efforts, he has managed to guide my work at the right points through many insightful conversations.

I thank Prof. H. Decker who has taken over the job of being my second supervisor of my Ph.D work and never gotten tired of my endless telephones and emails.

I would also like to thank Dr. Björn Persson and Dr. Stefan Löfås from Biacore for their continuous supports during the joint work. Their ideas and sensor chips are always the world class!

Thank you also goes to Prof. Neal Armstrong from University of Arizona, Akira and Shengjun for their enlightening ideas and experiments, which inspired and supported my work on the diffraction sensor. Without learning μ CP from Shengjun and without having the stamps from Shengjun and Aaron (IMRE, Singapore), my first several attempts could not have been done so smoothly.

I would also like to emphasize the importance of the flow cell engineering work supported by Pierre and Darick, and the LBL work carried out by Danica. I also profited a lot from the discussions with all the members of DNA group, Protein group and Electrochemical group (if any).

I have enjoyed the international atmosphere in Knoll's group, especially through countless parties. The lunch chat with the Chinese group members is often the highlight of the day. Among them, especially, great gratitude goes to Yun, who is the best brother-like friend you can ever hope for. Great respect goes to Tao, who is a kind of scientist I want to be. I have also enjoyed a very social office – 1.503, where I met so many friends. Thank you Darick and Jing, it is always a great fun to go traveling and photographing together with you. Thank you Catherine, Andreas and Nikolaus, you are always willing to translate German to English for me. Thank you Danica, for your cakes and cake recipe. Thank you Yanju, Sanong for sharing the paper-writing experiences.

A million thanks go to my wife, Danfeng Yao, who is also my colleague. During the last four years, we have been inspired by each other, of course, not only in science. I am proud of her intelligence and patience and honored to be her husband!

Last but not least, I owe a great debt of gratitude to my parents and my little brother, who have kept supporting me and being greatly considerate and patient to my staying abroad.

Curriculum Vitae

NAME: Fang Yu
GENDER: Male
DATE OF BIRTH: Dec. 09, 1975
NANTIONALITY: Chinese

EDUCATION

2000-2004:

Ph. D in Biophysics, Max-Planck-Institute for Polymer Research, Mainz, Germany

1998~2000

Master's Degree in Biomedical Engineering, Southeast University, Nanjing, China

1997-2000

Bachelor's Degree in Clinical Medicine, Nanjing Medical University, Nanjing, China

1993~1997

Bachelor's Degree in Biomedical Engineering, Southeast University, Nanjing, China

PUBLICATION LIST

1. Yu, F., Persson, B., Loefas, S., Knoll, W. Atto-molar sensitivity in bio-assays based on surface plasmon fluorescence spectroscopy, submitted to JOURNAL OF THE AMERICAN CHEMICAL SOCIETY.
2. Yu, F., Yao, D., Knoll, W. Oligonucleotide hybridization studied by a surface-plasmon diffraction sensor (SPDS), NUCLEIC ACIDS RESEARCH, in press.
3. Yu, F., Tian, S., Yao, D., Knoll, W. Surface plasmon enhanced diffraction for label-free bio-sensing, ANALYTICAL CHEMISTRY, in press.
4. Ekgasit, S., Thammacharoen, C., Yu, F., Knoll, W. Evanescent field in surface plasmon resonance and surface plasmon field-enhanced fluorescence spectroscopies, ANALYTICAL CHEMISTRY, 76, 2210 -2219, 2004.
5. Yu, F., Knoll, W. Immuno-sensor with self-referencing based on surface plasmon diffraction, ANALYTICAL CHEMISTRY, 76, 1971-1975, 2004.
6. Knoll, W., Yu, F., Neumann, T., Schiller, S., Naumann, R. Supramolecular functional interfacial architectures for biosensor applications, PHYSICAL CHEMISTRY CHEMICAL PHYSICS, 5, 5169-5175, 2003.
7. Yu, F., Yao, D., Knoll, W. Surface plasmon field-enhanced fluorescence spectroscopy studies of the interaction between an antibody and its surface-coupled antigen, ANALYTICAL CHEMISTRY, 75, 2610-2617, 2003.
8. Yu, F., Demirgoez, D., Knoll, W. Surface plasmon fluorescence techniques for interfacial protein binding studies, LABORWELT 4, 19-21, 2003.
9. Yu, F., Yao, D., Qian, W. Reflectometry interference spectroscopy in detection of hepatitis B surface antigen, CLINICAL CHEMISTRY, 46, 1489-1490, 2000.
10. Qian, W., Yao, D., Yu, F., Xu, B., Zhou, R., Bao, X., Lu, Z. Immobilization of antibodies on ultraflat polystyrene surfaces, CLINICAL CHEMISTRY, 46, 1456-1463, 2000.
11. Qian, W., Yao, D., Xu, B., Yu, F., Lu, Z., Knoll, W. Atomic force microscopic studies of site-directed immobilization of antibodies using their carbohydrate residues, CHEMISTRY OF MATERIALS, 11, 1399-1401, 1999.
12. Qian, W., Yu, F., Song, Z., Liang, B., Wei, Y. Site-specific immobilization of Fab' fragments of goat anti-human IgG on quartz surfaces, SUPRAMOLECULAR SCIENCE, 5, 701-703, 1998.